The Pennsylvania State University
The Graduate School
College of Engineering

ACOUSTIC PREDICTION OF HEAVY LIFT ROTOR CONFIGURATIONS USING MOMENTUM SOURCE METHOD

A Thesis in
Aerospace Engineering
by
Pavanakumar Mohanamuraly

Submitted in Partial Fulfillment
of the Requirements
for the Degree of

Master of Science

May 2010

The thesis of Pavanakumar Mohanamuraly was reviewed and approved* by the following:

Kenneth S. Brentner
Professor of Aerospace Engineering
Thesis Advisor

Phillip J. Morris
Boeing/A.D. Welliver Professor of Aerospace Engineering
Reader

George A. Lesieutre
Professor and Head, Aerospace Engineering
Department Head

*Signatures are on file in the Graduate School.

Abstract

Calculating acoustics for a full rotorcraft configuration in the design phase is a challenging task, which requires a numerical approach with the right level of fidelity at low computational cost. In the present work, an actuator line model (ALM) for the rotor is proposed where the individual blades of the rotor are modeled as singular line sources in the governing equation by adding momentum and energy equivalent to the rotor. This model was implemented in a parallel unstructured, finite-volume compressible Euler (UFVS) solver, which uses the Roe approximate Riemann solver for interfacial fluxes calculation and an optional $2^{nd}/4^{th}$ order Runge-Kutta method for the time integration. Using overset grid methodology the UFVS-ALM solver was embedded into a bigger suite of tools called Immersed Boundary Solver for Environment Noise (IBSEN) such that the rotor near field is modeled using the UFVS-ALM approach and the flow field over other solid bodies like fuselage, wing and other appendages are captured using IBSEN's Cartesian Grid solver. A model isolated rotor in hover with rectangular, un-tapered blades and NACA 0012 airfoil section was used as a test case to validate the standalone UFVS-ALM solver and the overset UFVS-ALM IBSEN numerical approach. The results are validated against experimental values and the predicted flow field and acoustics are qualitatively assessed.

Table of Contents

List of Figures

List of Tables

List of Symbols

English

p	Fluid pressure
p'	Acoustic pressure
p'_T	Thickness acoustic pressure
p'_L	Loading acoustic pressure
e	Internal energy of fluid
H	Fluid enthalpy
V_c	Climb velocity
$w/\mathbf{w}$	Induced velocity magnitude/Induced velocity vector
u_s	Velocity vector over fluid volume element
v_free	Free stream velocity vector
V_{rel}	Resultant velocity
C_l	Non-dimensional lift coefficient
C_d	Non-dimensional drag coefficient
$\mathbf{f}$	Body force term
Re	Reynolds number
M	Mach number
L	Lift force

D	Drag force
F_{x-z}	Blade forces w.r.t the inertial frame
$\mathbf{x}$	Source position vector
$\mathbf{y}$	Observer position vector
r	Radial coordinate (also) distance between source and observer $\lvert\mathbf{x}-\mathbf{y}\rvert$
c	Speed of sound
t	Time
ξ	Blade cord-wise coordinate
η	Blade thickness coordinate
CV	Fluid control volume
Q	Monopole like term in FW-H equation (also) State vector
F_i	Dipole like term in FW-H equation
l_i	Chordwise compact loading vector
$\mathbf{F}$	Flux vector
G	Rotor forcing term in governing equation
f	Source surface
z_{loc}	Rotor location along the z-direction
r_{tip}	Tip correction length
$\mathcal{R}$	Rotor radius
T_{ij}	Lighthill's stress tensor

Greek

ρ	Fluid density
ϕ	Inflow angle

Ω	Angular velocity of rotor
$\mathbf{\Omega}$	Volume of integration
$\mathbf{\Gamma}$	The blade local $\xi - \eta$ plane
λ	Non-dimensional induced velocity (inflow ratio)
λ_c	Non-dimensional climb velocity
θ_0	Rotor cone angle
θ	Pitch angle
σ	Standard deviation of Gaussian function
δ	Dirac delta function
δ_{ij}	Kroenecker delta function
τ	Retarded time
α_{1-6}	Intermediate variables used in Jacobian matrix
κ_c, κ	Intermediate variables used in BEMT calculation (climb)

Super/Subscript

$(\tilde{\ })$	Roe average value
$(\dot{\ })$	Time derivative
$() \cdot ()$	Dot product
$()_{BET}$	Value obtained from Blade Element Theory
$()_n$	Component of vector along the normal direction
$()_c$	Value at cell center
$()_L$	Left cell value
$()_R$	Right cell value
$()_M$	Component of vector along the Mach number direction

$()_\infty$	Free-stream value
$()_\epsilon$	Regularized value
$(\hat{\ })$	Unit vector
$() \otimes ()$	Tensor outer product
$\Box^2()$	D'Alembertian (wave operator) $\frac{1}{c_\infty^2}\frac{\partial^2}{\partial t^2} - \frac{\partial^2}{\partial x_i \partial x_i}$
$\frac{\bar{\partial}}{\partial \eta}()$	Generalized derivative w.r.t variable η
$\nabla()$	Gradient operator $\frac{\partial}{\partial x}\hat{i} + \frac{\partial}{\partial y}\hat{j} + \frac{\partial}{\partial z}\hat{k}$

Acknowledgments

The author would like to thank Dr. Kenneth S. Brentner for his support and trust throughout this research work. The author would also like to thank Dr. Phillip J. Morris for agreeing to be the thesis reader and reviewing the thesis in a short time. This study was supported by the U.S. Army through the Vertical Lift Research Center of Excellence (VLRCOE) program under sponsored research agreement W911W6-2-0008. The author is grateful to Dr. Ganesh Rajagopalan, Professor Aerospace engineering, Iowa State University, co-investigator in the project.

The author is grateful to the staff and faculty of Aerospace Engineering department, Penn State, for their help and support. The author would like to thank all students of Vertical Lift Research Center Of Excellence (VLRCOE) for their help and support. In particular, the author would like to thank Dr. Len Lopes for his help with the Blade Element code; Dr. Seongkyu Lee for the useful discussions on Aeroacoustics which gave good insight into some of the issues; Mr. Ganesh Vijayakumar and Mr. Pankaj Jha for sharing their experience with the Actuator model; Mr. Christopher C. Hennes, without whose help the IBSEN coupling would not be possible; and finally Mr. James P. Erwin for this moral support during the toughest time of the author's life.

Chapter 1

Introduction

The present work is a part of a new multi-tiered suite of tools capable of predicting rotorcraft noise at various levels of fidelity depending on the required accuracy and computational time constraints. The tools are developed from the outset for acoustic prediction during the early design cycle of the rotorcraft. Acoustics is typically neglected during the early design cycle due to its computational complexity. If modern rotorcraft designs are considered, the impact of acoustics can be quite significant. For example, placing the main rotor close to the fuselage to reduce hub drag could result in significant increase in the fuselage-rotor interactional noise. Similarly, heavy-lift rotor configurations like co-axial rotors, pusher-props and quad-tilt rotors have extremely complex aerodynamic interactions and could increase noise levels. Contemporary Computational Fluid Dynamics (CFD) tools are prohibitively expensive to capture such aerodynamic interactions. Therefore, approximations and modeling are required at various levels for the tool to perform acoustic analysis of complex rotorcraft configurations with practical computational time. This is the primary motivation of the present work. The tool proposed here has to perform tasks that are two fold. Firstly, it must predict the unsteady aerodynamic interactions of the rotorcraft configuration. Secondly, it must provide the unsteady aerodynamic data which is suitable for noise prediction.

Existing methods in the literature used for unsteady interactional aerodynamics can be broadly classified into three categories[1] viz., Singularity, CFD and Hybrid methods. As illustrated in figure 1.1, singularity methods are lowest in computational complexity and time. Panel methods, Lifting-line approximation

and Free Vortex methods fall under this category. These methods can capture lower order interference effects and mean flow quantities. However, unsteady flow field information and other higher order effects cannot be captured. CFD methods have the highest computational cost and at the same time are the most accurate in capturing unsteady interactions. However, they are not suitable for preliminary design, where hundreds of possible configurations are analyzed. Hybrid methods lie in-between these methods in terms of problem complexity and computational time. Although, many hybrid methods are available in the literature for use in early design, none are currently available to capture interactional aerodynamics with sufficient fidelity and speed for acoustic design calculations. A brief review of methods available in the literature for unsteady interactional aerodynamics is provided in the section to follow. Following this, a review of available methods for rotorcraft acoustics are discussed.

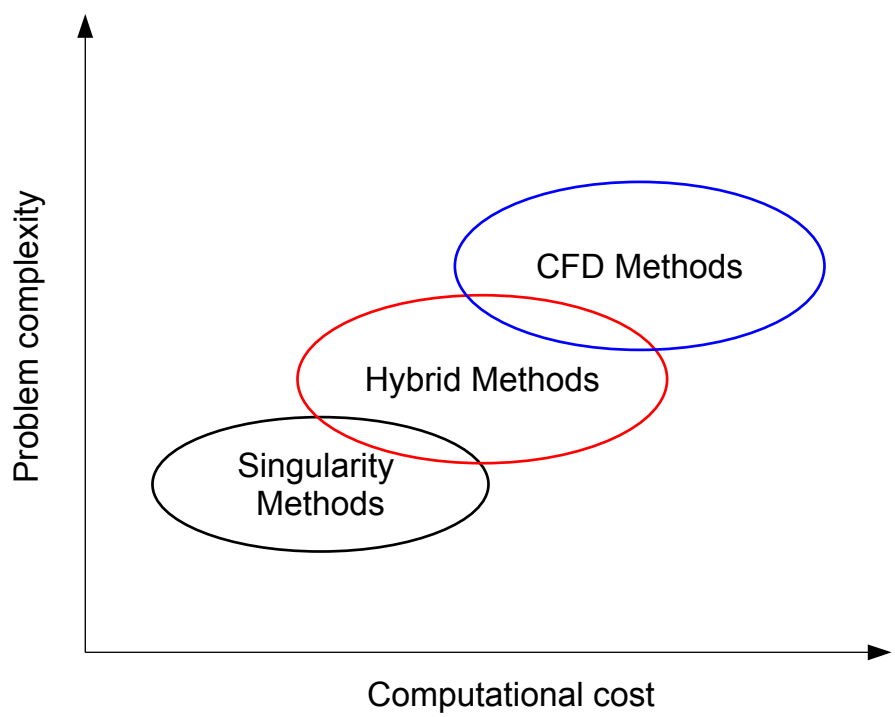

Figure 1.1: Classification of methods with respect to problem complexity and computational time[1].

1.1 Literature Survey

In this section a brief review of the three types of methods namely (i) Singularity methods, (ii) CFD methods and (iii) Hybrid methods is presented.

1.1.1 Singularity methods

In singularity methods, mathematical singularities like sources, sinks, point vortices, etc. are introduced into the governing potential flow equations to model physical bodies like a fuselage, wings, and rotor blades. The Panel method, Vortex/Free Wake method and Lifting Line method are a few singularity methods used regularly in rotorcraft industry. Kartz and Maskew[5] used a modified panel method to predict unsteady loads on helicopter blades and fuselage. Similar studies using the panel method for rotorcraft were conducted by Summa[6] and Ahmed et al.[7]. Here the authors pointed out the requirement of an assumed initial rotor wake to start the calculation. Consequently, the solution was dependent on this assumed initial wake. In addition, wake calculations for subsequent time steps could become computationally expensive. Aerodynamic interference due to the presence of fuselage or auxiliary wing of a compound helicopter are difficult to model in singularity methods. Nevertheless, attempts have been made to model such effects by making certain approximations. In reference [8], an analytical method to calculate interference effects of appendages was developed. Two-dimensional analytical models with suitable correction factors were used to obtain the pressure distribution and force on circular and square-sectioned fuselages and on wings in three dimensions. The changes in lift forces on the blades were presented for hovering flight. Peters et al.[9] proposed an unsteady aerodynamic theory based on induced inflow called the Generalized Dynamic Wake Theory (GDWT) to calculate blade loads for a rotor in hover and forward flight. The theory incorporates the unsteady potential flow theory of Theordosen, Goldstein static inflow distribution and dynamic-inflow theory. Boyd et al.[1] have recently extended the GDWT to include the interference of the fuselage by an inflow correction factor obtained using potential flow theory.

1.1.2 CFD methods

In the CFD method the governing equations of fluid dynamics are approximated by algebraic equations over a finite region. The algebraic equations are solved using the initial and boundary conditions over discrete time intervals. The unstructured finite volume method is sometimes a preferred method in CFD due its robustness in terms of both numerical stability and ease of grid generation for complex configurations. Strawn and Biswas[10] used an adaptive unstructured grid to calculate unsteady aerodynamics of an isolated rotor. The authors concluded that for unsteady flows a structured grid gave a better solution and the same was used for subsequent calculations. The interfacial fluxes were calculated using Roe upwind differencing and a third order MUSCL-type limiting to capture shock waves accurately to predict High-Speed Impulsive noise (HSI) generated by the rotating blades. Chen[11] conducted similar transonic rotor calculations using the same schemes as in reference [10]. However, the analysis was performed in a quasi-steady manner. Both studies reported good agreement with experiments but the computational time is too high to be used for routine design calculations.

In reference [12], overset grids were used to simulate unsteady flow over a full helicopter configuration in both hover and forward flight. The authors used overset grids to simulate flow over the complex configuration. In this method, the grids are generated over individual components and later assembled together to form a composite grid system. The discretized governing equations are solved over the different components by applying suitable boundary conditions at grid interfaces. The overset grid system was a cylindrical background grid over which the individual rotor grids were overlapped. Discretized three-dimensional Euler equations were solved using the finite volume method. The primary use of the solver was geared towards the helicopter industry by minimizing the time and efforts of a designer in setting up cases. The cell count for an isolated rotor case in hover was less than a million cells and for a forward flight case about 1.1 million cells. However, with the presence of a fuselage and tail rotor system the cell count can increase tremendously. Hence, even with an overset system the problem size becomes too large for design calculations.

1.1.3 Hybrid Methods

Many researchers have proposed hybrid methods by combining the above-mentioned methods. These methods are intermediate in problem complexity and computational time. This is achievable by simplifying the problem by modeling the rotor. The resolution requirement is reduced significantly because capturing details of the flow, like the wall boundary layer, are no longer necessary. The hybrid methods are broadly divided into two categories : Modeling the effect of rotor using (i) a pressure jump boundary condition and (ii) a momentum source term in the governing equation. Reference [13] contains a detailed survey of existing hybrid methods. In reference [13], the author used both pressure jump boundary condition and source term to model the rotor. The rotor was idealized as an infinitely thin time averaged disk over which a jump in pressure or momentum addition was prescribed and the flow field was solved in a quasi-steady manner. The properties across the disk were loosely coupled with an unsteady Reynolds-Averaged Navier Stokes flow field calculation and were changed at regular quasi-time intervals based on the converged flow solution. Rajagopalan et al.[14, 15] used a similar time averaged momentum disk to model rotors in an incompressible Navier Stokes finite-volume formulation using the SIMPLE scheme of Patankar[16] for pressure correction to satisfy mass conservation. The author used stretched Cartesian grids over which the rotor sources were placed. This method showed a significant decrease in computational time. In references [4] and [17], a pressure jump boundary condition over the time averaged disk was used to model the rotor. It was suggested that the pressure-jump could be fixed either by using an assumed rotor load distribution or could be corrected at each time step based on the inflow (load) predicted using CFD.

Boyd et al.[1] took a different approach in modeling the rotor blades. Instead of assuming a time-averaged disk, the authors used an unsteady moving pressure jump to model the rotor. The angular position of the pressure-jump boundary was kept in sync with the respective blade azimuth. The pressure-jump value was corrected for the fuselage interference once a periodic solution was obtained (loose coupling). The correction factor was obtained from the difference between the filtered CFD inflow and the GDWT inflow. Unlike the approach adopted by Boyd, Mikkelsen[18] used a more tightly coupled model for wind turbine rotors. Mikkelsen

used a line momentum source (actuator line) placed along the blade span to model the rotor. The stream-function-vorticity formulation of the incompressible Navier-Stokes equations was solved using the finite difference method along with the line source. At each time step, the momentum source strength was determined using Blade Element Theory (BET) and flow field information. Gaussian kernels with prescribed parameters were used to regularize the actuator line source for a robust numerical implementation. The authors mentioned that the method required a suitable tip correction algorithm. In reference [19], a detailed analysis of various tip corrections was presented and the authors suggested a modified Prandtl's tip correction formula applied to wind turbine blades.

Time rate of change of loading is important and has a dominant effect on noise. Therefore, modeling the rotors as a time averaged disk removes unsteady load information present in the blade. The moving pressure jump captures the individual unsteady blade information. However, special assumptions are required to obtain the pressure jump value. For example, in GDWT, a potential flow assumption was made to derive the pressure jump value. Moreover, such a method did not allow tight coupling between the flow solver and the pressure jump value. In the actuator line source method, a tighter coupling between the flow solver and source strength is possible. The main drawback of this method was the requirement of a tip correction for the rotor. Analytical tip loss formulae[19] were derived assuming a helical wake for an isolated rotor in hover, which might not be appropriate for forward flight cases.

1.2 Acoustics Literature Review

Modern rotorcraft acoustic predictions are mostly performed using time domain methods. The acoustic prediction methods used in rotorcraft application can be classified into two categories - (i) Lighthill's Acoustic Analogy Formulation and (ii) Kirchhoff Formulation. In Lighthill's acoustic analogy formulation the governing equations are rearranged into a wave operator on the left hand side and source terms on the right hand side. The wave equation is converted into integral formulation using the free space Green's function and suitable numerical integration scheme is used to obtain the solution. The advent of the Ffowcs Williams

- Hawking (FW-H) equations[20], an extension of Lighthill's analogy to moving bodies in arbitrary motion, in 1969 encouraged research in the direction of noise generation in moving bodies like propellers and helicopter rotors using the acoustic analogy. Using the FW-H equation, various physical phenomena associated with helicopter blades like High-Speed Impulsive (HSI) noise, Blade-Vortex-Interaction (BVI) noise, thickness noise and loading noise of rotors can be explained. Brentner and Farassat[21] gave a historical survey of time domain acoustic methods used in rotorcraft acoustic predictions. Farassat et al.[22–24] have derived various integral formulations to solve the FW-H equations with successful application to real rotor configurations. Brentner and Farassat[25] provided a detailed review of the formulations and the numerical algorithms involved in the solution procedure.

The Kirchhoff formulation is another approach used acoustic prediction method and usually restricted to stationary surface sources. Morgans [26] and Khromov [27] independently attempted to extend the Kirchhoff formula to moving surfaces. A much clearer derivation was laid out by Farassat et al.[28] The authors point out anomalies/errors in the work done by the previous author[26]. The FW-H equations incorporate more physics than the Kirchhoff formula through the inclusion of the quadrupole term. Brentner and Farassat in [29] showed the superiority of the formulation based on the FW-H equation over the Kirchhoff formula. Nevertheless, Kirchhoff formula has enjoyed some success in the aeroacoustic community. Lyrintzis et al.[30–32] have applied the Kirchhoff formula for transonic blade-vortex interaction, tilt-rotor configurations and jet acoustics. In the present work, the acoustic code PSU-WOPWOP[33, 34], based on Formulation 1A of Farassat[24], is used to obtain the acoustics field from rotating blades of the rotorcraft. Brentner et al.[33–35] have extensively validated the code and have shown great success in predicting noise from various rotor configurations.

Chapter 2

Acoustics Theory

The code PSU-WOPWOP[33, 34] is used to predict acoustics using the blade loading information from Computational Fluid Dynamics (CFD) solution. The acoustic code is based on the integral formulation 1A of Farassat[24], which is a solution of the FW-H equation. The FW-H equation is an extension of Lighthill's acoustic analogy to account for noise from bodies in arbitrary motion. The equations are an exact rearrangement of the Navier-Stokes equation into a wave operator acting on acoustic pressure or density on the left hand side and all other terms combine to form the acoustic source terms on the right hand side as shown in equation (2.1). In equation (2.1), $\Box^2$ is the D'Alembertian operator, p' is the acoustic pressure and T_{ij} is the Lighthill's stress tensor defined in equation (2.2). The Lighthill stress tensor is the residual stress arising from the action of the effective fluid stress (fluctuating Reylonds stress, $\rho u_i u_j$ and compressive stress P_{ij}) and the stress due to the acoustic medium at rest $c_\infty^2 \rho$.

$$\bar{\Box}^2 p' = \frac{\partial}{\partial t}\{Q\delta(f)\} - \frac{\partial}{\partial x_i}\{F_i\delta(f)\} + \frac{\bar{\partial}^2}{\partial x_i \partial x_j}\{T_{ij}H(f)\} \tag{2.1}$$

$$T_{ij} = \rho u_i u_i + P_{ij} - c_\infty^2 \rho \delta_{ij} \tag{2.2}$$

The three terms on the right hand side of equation (2.1) have become known as the thickness, loading and quadrupole noise source terms, respectively. The thickness noise source results from the displacement of fluid caused by the moving body and it is predominant in plane of the rotor. The accelerating force distribution on

the body due to it motion in the fluid generates loading noise, which is predominant below the plane of the rotor. Nonlinear effects like variation in local sound speed, fluid particle velocity, transonic flow and other volumetric phenomenon are modeled by the quadrupole source term. Using generalized functions the problem is embedded in the entire free space and hence the free space Green's function maybe employed to solve for the acoustic pressure. The change of variables employed during the integration of the FW-H, differentiates the various solution formulations. Farassat's formulation 1A[24] used in PSU-WOPWOP[33, 34] is one such form, that neglects the quadrupole source term. A detailed derivation of the same can be found in reference [36].

$$4\pi p'(\mathbf{x},t) = p'_T(\mathbf{x},t) + p'_L(\mathbf{x},t) \tag{2.3}$$

where,

$$\begin{aligned} p'_T(\mathbf{x},t) &= \int_{f=0} \left[\frac{\dot{Q}}{r|1-M_r|^2}\right]_{ret} d\mathbf{S} + \\ &\quad \int_{f=0} \left[\frac{Q(r\dot{M}_r + c_\infty M_r - c_\infty M^2)}{r^2|1-M_r|^3}\right]_{ret} d\mathbf{S} \qquad (2.4) \\ p'_L(\mathbf{x},t) &= \frac{1}{c_\infty}\int_{f=0} \left[\frac{\dot{F}_r}{r|1-M_r|^2}\right]_{ret} d\mathbf{S} + \int_{f=0} \left[\frac{F_r - F_M}{r^2|1-M_r|^2}\right]_{ret} d\mathbf{S} + \\ &\quad \frac{1}{c_\infty}\int_{f=0} \left[\frac{F_r(r\dot{M}_r + c_\infty M_r - c_\infty M^2)}{r^2|1-M_r|^3}\right]_{ret} d\mathbf{S} \qquad (2.5) \end{aligned}$$

where for an impermeable surface,

$$Q = \rho_\infty v_n \tag{2.6}$$

$$F_i = P_{ij} n_j \tag{2.7}$$

The suffixes on any vector denotes the component of the vector in the suffix direction. The body velocity is denoted by v_i. The suffix ret denotes that, the quantity is evaluated at the retarded time $\tau = t - \frac{r}{c_\infty}$. Here, r is the radial distance between the source position, $\mathbf{x}$ and the observer position $\mathbf{y}$ at the retarded time. The terms p'_T and p'_L in equation (2.3) are the thickness and loading noise terms respectively. The thickness noise term p'_T for impermeable surfaces does not require the flow

field information. It requires only the motion description and geometry of the surface. Whereas, in the loading noise calculation, the dipole like term F_i requires the fluid stress P_{ij} (or pressure in the case of an inviscid fluid) at the surface. The quadrupole term of the FW-H equation is neglected in the derivation of formulation 1A because it is found to be negligible in low Mach number flows. It should be noted that in the equation (2.5), the first term containing the time derivative of F_i is often predominant because it contributes most to the loading acoustic pressure p'_L when the loading changes rapidly. Hence, care should be taken while obtaining the loads because even a small temporal error in F_i can give a large error in calculating the time derivative $\dot{F}_r$.

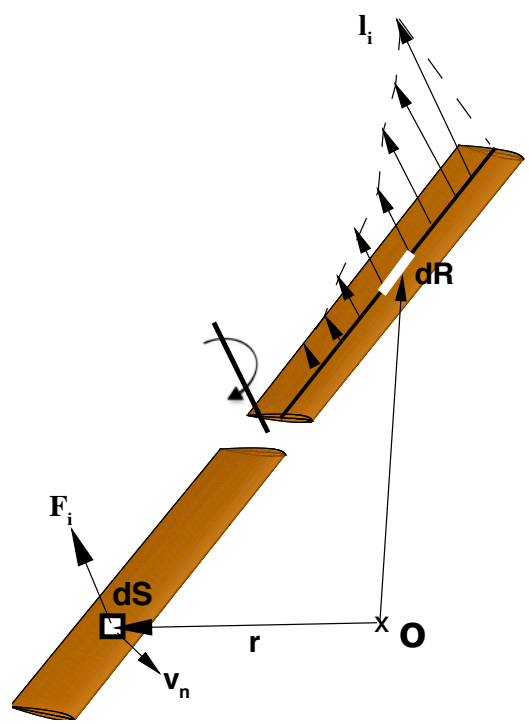

Figure 2.1: Two bladed rotor setup for acoustic prediction at observer position O.

In figure 2.1 a setup to predict the acoustic pressure from a two bladed rotor at a particular observer location is shown. As described in reference [37] the sectional lift distribution can be used instead of the pressure distribution over the blade surface if the chordwise variation of pressure is small compared to the wavelength of the radiated noise. Therefore, one can integrate the chordwise load distribution and represent it as a point load placed along the span of the blade, as shown in the

figure 2.1. This type of approximation is referred to as compact chordwise loading and is suited to low frequency noise prediction. Brentner et al.[38] found that this approximation could predict noise to within a few decibels or less, especially below the rotor, while most of the error in the approximation occurs for inplane observer locations. Good computational speedup can be achieved since the integration along the chordwise direction is no longer necessary. The loading noise integral in formulation 1A with the compact chordwise loading assumption can be written as,

$$\begin{aligned} p'_L(\mathbf{x},t) &= \frac{1}{c_\infty}\int_{f=0}\left[\frac{\dot{l}_r}{r|1-M_r|^2}\right]_{ret} dR + \int_{f=0}\left[\frac{l_r - l_M}{r^2|1-M_r|^2}\right]_{ret} dR + \\ &\quad \frac{1}{c_\infty}\int_{f=0}\left[\frac{l_r(r\dot{M}_r + c_\infty M_r - c_\infty M^2)}{r^2|1-M_r|^3}\right]_{ret} dR \end{aligned} \tag{2.8}$$

where l is the lift force per unit length of the blade and R is the spanwise integration variable (1D).

In the present work, the compact chordwise loading on the rotor blades is predicted using Computational Fluid Dynamics (CFD) where the rotors are modeled as forcing terms in the governing fluid dynamics equations. This is discussed in detail in chapters 3 and 4.

Chapter 3

Actuator Line Model

A survey of hybrid methods in literature was provided in the first chapter. These methods can be broadly categorized into two types, namely, modeling the effect of the rotor as (i) a pressure jump and (ii) a body force term in the governing fluid dynamic equations. The way the individual terms are implemented, the form of governing equations, and the numerical method used to solve the flow field are some of the factors that are unique to a particular type. Shown in equations (3.1-3.3) are the compressible Euler equations in conservative form. The momentum equation (3.2) is arranged such that the flow variables are on the left hand side and the driving potential terms are on the right.

$$\frac{\partial \rho}{\partial t} + \nabla \cdot (\rho \mathbf{u}) = 0 \tag{3.1}$$

$$\frac{\partial (\rho \mathbf{u})}{\partial t} + \nabla \cdot (\rho \mathbf{u} \otimes \mathbf{u}) = -\nabla p + \rho \mathbf{f} \tag{3.2}$$

$$\frac{\partial (\rho e)}{\partial t} + \nabla \cdot (\rho \mathbf{u} e) = -\nabla \cdot (p \mathbf{u}) \tag{3.3}$$

According to the momentum equation (3.2), fluid motion exists in the presence of either a pressure gradient (∇p term) or a body force ($\rho \mathbf{f}$ term). The two types of forces differ from each other by the way they are manifested in the fluid. The ∇p term is a surface force and requires a surface/boundary to impart force on a fluid volume element. In contrast, the $\rho \mathbf{f}$ term is typically a volumetric force like gravity and magnetic field and hence these forces do not require any boundaries to act. It is more appropriate to categorize the methods into modeling the effect of the

rotor (i) as a surface force or (ii) as a volumetric body force. It was pointed out in reference [2] that the two methods are equivalent. This statement is only partially true because the two methods actually represent different physical behavior and are equivalent only under a special condition viz., conservative body force i.e, $\rho\mathbf{f}$ is the gradient of a scalar function as shown in equation (3.4). Batchelor in [39] states, "*... all terms (of momentum equation) can be written as integrals over the bounding surface A, for then the details of the motion within the region enclosed by A are irrelevant ... The contribution from the volume force can be put in the form of a surface integral when* $\rho\mathbf{f}$ *can be written as the gradient of a scalar quantity*".

$$\rho\mathbf{f} = \nabla\left(\rho\phi\right) \tag{3.4}$$

The difference extends beyond this physical interpretation for the two methods

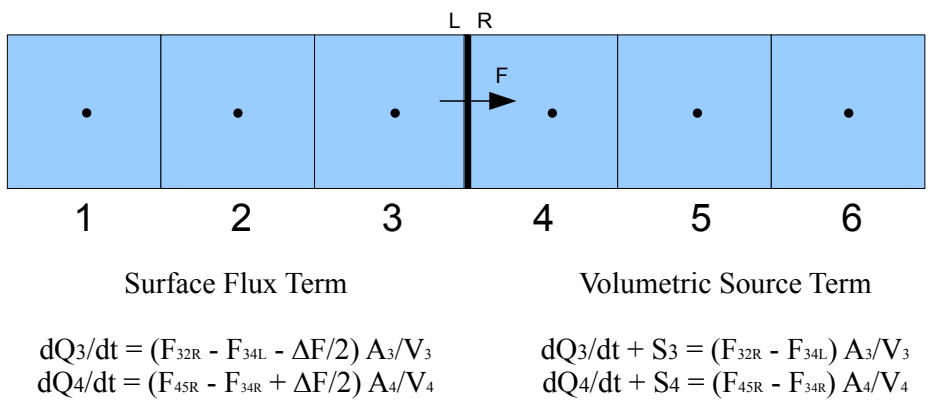

Figure 3.1: Comparison of types of rotor model implementations [2].

and is illustrated in figure 3.1. Here a one dimensional computational domain is shown - the dots represent the cell center and the vertical lines denote the faces separating two cells. The equation on the bottom left equation of figure 3.1 is the surface force addition, where the face averaged surface term (left) ΔF is added to the interfacial flux integration. On the right, the volume force addition is shown, where the cell averaged volume force S adds directly to the time integration of the state vector Q. Thus, the two methods are different even in their numerical implementation. With the clear understanding of the driving potential, one must now understand the physics of the problem to be able to propose a suitable model

for the rotor.

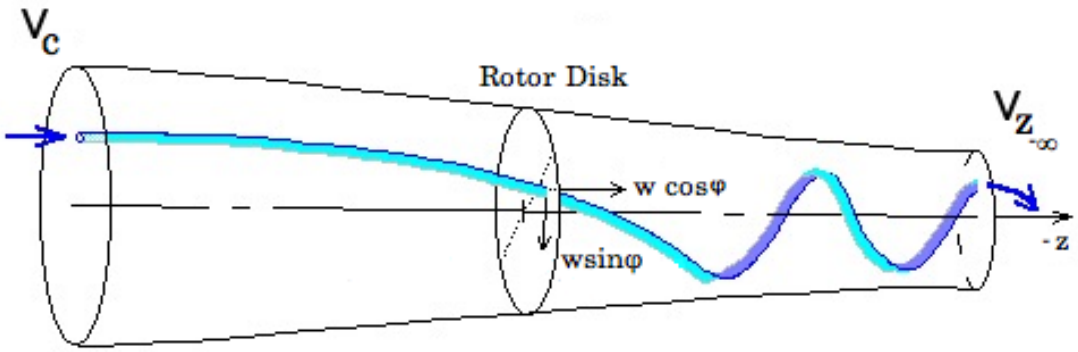

Figure 3.2: Representative Stream-tube across a typical rotor (adapted from [3]).

Figure 3.2 shows a stream tube plot in the flow field of a representative rotor. One can infer from the figure that a rotor affects the flow field in two ways. Firstly, the rotor adds momentum to the fluid inducing axial velocity and swirl. Secondly, the rotor does work on the fluid thereby increasing its internal energy. The physical mechanism generating the induced velocities is the production of stresses in the fluid (normal and shear) due to the rotor. In traditional CFD, a wall boundary condition is implemented at the rotor surface, enforcing a slip boundary condition for inviscid equations and a no-slip condition for viscous flow equations. Enforcing this wall boundary condition generates the required stresses that drive the fluid motion. Steep gradients in flow field values exist near the wall and hence high spatial resolution is required to capture them correctly. This makes the near wall calculations computationally intensive. If one could somehow add directly to the fluid the stresses generated by the rotors, it would be possible to artificially mimic its effects. At the same time one can reduce the spatial resolution requirement if the detailed flow field near the wall is not necessary.

The forces generated by the rotor are not known prior to providing input to the CFD calculations. They should evolve as a part of the flow field solution. These forces should be predicted or assumed initially and corrected iteratively using the obtained flow solution till a correct state is reached. In the present work, Blade Element Theory (BET) is used to calculate the forces generated by the blade. The forces are corrected using the new induced velocity predicted by CFD. The details

of the implementation and coupling the CFD calculations with BET are provided in the chapter 4 and only the derivation of the rotor source terms is shown in this chapter.

3.1 Blade Element Theory (BET)

Although BET was developed and used by many authors, Knight and Hefner[40] were among the first to use this theory to study helicopter rotors. The theory assumes that each blade section is an independent 2D airfoil generating lift and drag forces. Integrating the loads generated by the individual airfoil sections over the blade span and summing over the total number of blades, one obtains the total thrust and torque of the rotor. The BET assumes that the induced velocity over each blade section is a known quantity. Therefore, the induced velocity should be determined by coupling the BET with other methods. In the present work, the induced velocity is determined using CFD and the blade forces determined using BET are added as forcing terms in the CFD governing equations. The local blade section of a coned rotor rotating with angular velocity Ω in vertical flight is shown in figure 3.3. The vertical velocity is V_c, blade chord is c, blade span b and number of blades N_b. The induced velocity is w and it is perpendicular to the resultant velocity V_{rel}. The angles θ, α and ϕ are the pitch angle, angle of attack and inflow angle respectively. Using trigonometry one can determine ϕ using equation (3.6) and the angle of attack can then be calculated using ϕ and the blade pitch θ using equation (3.7). The blade coning angle θ_0 can be either a predefined input or obtained from the trim solution.

$$\sin\phi = \frac{V_c + w\cos\phi}{V_{rel}} \ , \ \cos\phi = \frac{r\Omega - w\sin\phi}{V_{rel}} \ \& \ \tan\phi = \frac{V_c + w\cos\phi}{r\Omega - w\sin\phi} \tag{3.5}$$

$$\phi = \tan^{-1}\left(\frac{V_c + w\cos\phi}{r\Omega - w\sin\phi}\right) = \tan^{-1}\left(\frac{\lambda_c + \lambda\cos\phi}{1 - \lambda\sin\phi}\right) \tag{3.6}$$

$$\alpha = \theta - \phi \tag{3.7}$$

Once the angle of attack α and resultant velocity V_{rel} are known the lift dL/dr and drag dD/dr forces per unit length of the blade (where r is the blade span

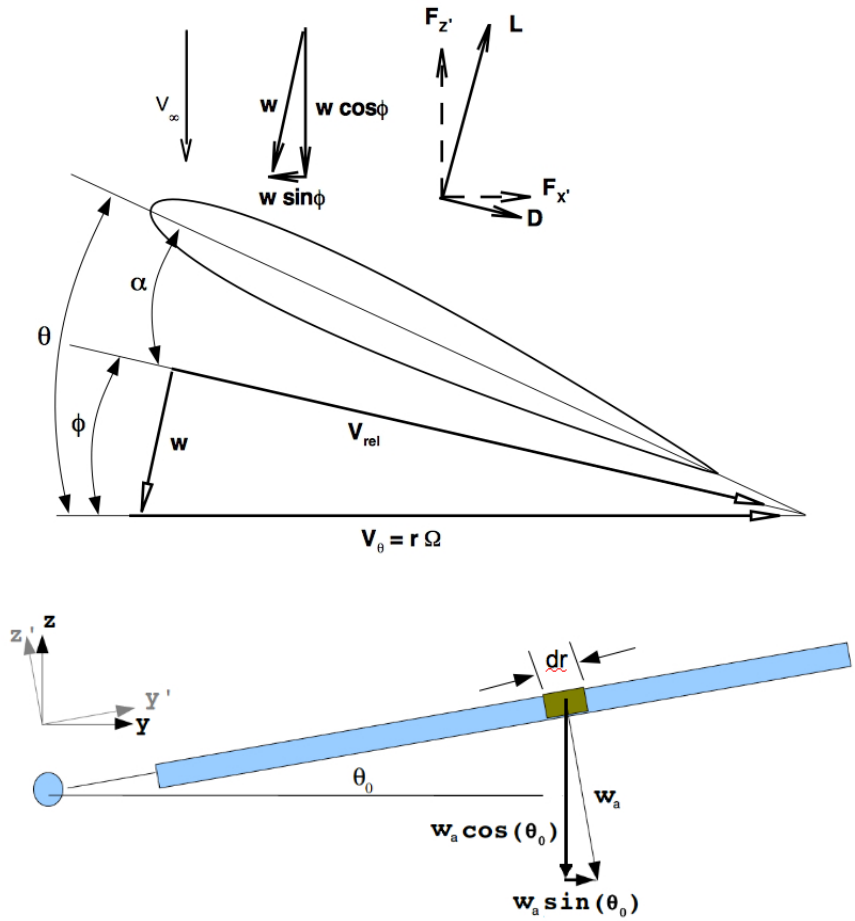

Figure 3.3: Blade Element Analysis in Vertical Flight.

coordinate) can be found as shown in equation (3.8).

$$\frac{dL}{dr} = \frac{1}{2}\rho\, V_{rel}^2\, C_l\, c \quad \& \quad \frac{dD}{dr} = \frac{1}{2}\rho\, V_{rel}^2\, C_d\, c \tag{3.8}$$

where, $C_l = C_l(\alpha, Re, M)$ and $C_d = C_d(\alpha, Re, M)$ are the two-dimensional lift and drag coefficients, which are functions of Reynolds number, Re, and Mach number, M, at the local blade section. Then, using suitable transformations, one can determine the thrust dF_z/dr and torque force dF_θ/dr per unit span acting on the local blade section as shown in equations (3.9) and (3.10).

$$\left(\frac{dF_z}{dr}\right)_{BET} = \frac{dF_{z'}}{dr}\cos\theta_0 = \left(\frac{dL}{dr}\cos\phi - \frac{dD}{dr}\sin\phi\right)\cos\theta_0 \tag{3.9}$$

$$\left(\frac{dF_\theta}{dr}\right)_{BET} = \frac{dL}{dr}\sin\phi + \frac{dD}{dr}\cos\phi \tag{3.10}$$

The values of C_l and C_d can be determine using a table lookup of tabulated empirical values. In the present study, the thin airfoil assumption is made and a value of $2\pi\alpha$ is used for the lift coefficient and the drag component is neglected because typical lift to drag ration (L/D) for airfoils are small. For example, the (L/D) ratio for NACA0012 airfoil is about 78 at sectional C_l of 0.6 and about 17 at sectional C_l of 0.1.

3.1.1 Tip Correction Formula

Even if the CFD calculations are three dimensional, the flow field is determined based on the forcing terms supplied by BET, which are two dimensional. Therefore, important 3D effects such as loss of lift at the blade tips due to pressure compensation (finite number of blades) cannot be predicted by BET. The problem can be overcome by correcting the loads predicted by BET using a suitable tip correction formula. Prandtl derived such a correction analytically for hovering rotors. The formula due to Prandtl, modified by Glauert, is shown in equation (3.11). Here, F is the correction factor and is a function of the span-wise location r, inflow angle ϕ and number of blades N_b.

$$F = \frac{2}{\pi}\cos^{-1}\left[\exp\left(-\frac{N_b(R-r)}{2r\sin\phi}\right)\right] \tag{3.11}$$

A detailed derivation of Prandtl's tip loss function can be found in reference [41]. On close analysis of the derivation, one observes that the model was essentially two dimensional and the function F corrects the load for a given two dimensional rotor flow field. Consequently, one cannot use the inflow angle obtained from 3D CFD calculations to obtain the tip loss function F as it will be inconsistent with the assumptions. In order to maintain consistency the combined Blade Element and Momentum Theory (BEMT) of Glauert[42] is used to calculate the inflow angle required for the tip loss function calculation. In Momentum Theory, a cylindrical

control volume is chosen along the axis of the rotor as shown in figure 3.4. The rotor is idealized as an infinitely thin disk with a jump in pressure Δp that drives the flow. Using the law of conservation of momentum (inviscid, incompressible fluid) the thrust force $(dF_z/dr)_{MT}$ per unit length dr can be obtained as shown in equation (3.12). Applying the tip correction to equation (3.12) and equating it to equation (3.9), the induced velocity required to yield the correct blade load distribution can be obtained. Equation (3.13) is the result of the combined Blade Element and Momentum Theory (BEMT). The terms $(dF_z/dr)_{BET}$ and ϕ are both functions of the induced velocity w therefore an iterative numerical technique like Newton's method should be used to solve for w.

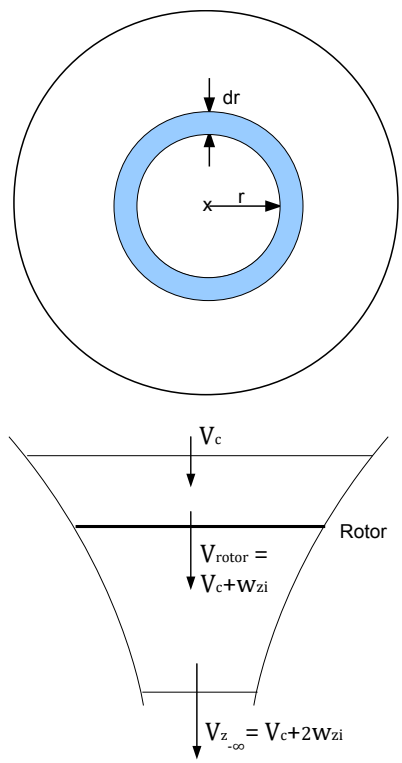

Figure 3.4: Control volume used in momentum analysis.

$$\left(\frac{dF_z}{dr}\right)_{MT} = 4\pi r\rho(V_c + w\cos\phi\cos\theta_0)w\cos\phi\cos\theta_0 \tag{3.12}$$

$$w^2 + \kappa_c w - \kappa = 0 \tag{3.13}$$

where,

$$\kappa_c = \frac{V_c}{\cos\phi\cos\theta_0} \qquad \& \qquad \kappa = \frac{(dF_z/dr)_{BET}}{4\pi\rho\cos^2\phi\cos^2\theta_0}$$

If $w = \tilde{w}$ is the solution obtained for a given blade geometry and rotor condition then the tip loss function $\left(F = \tilde{F}(\tilde{w}, r)\right)$ for that particular configuration can also be determined. The tip loss function is determined using BEMT only once for a rotor configuration and the same is used to correct the loads at all time steps in the combined BET-CFD calculation.

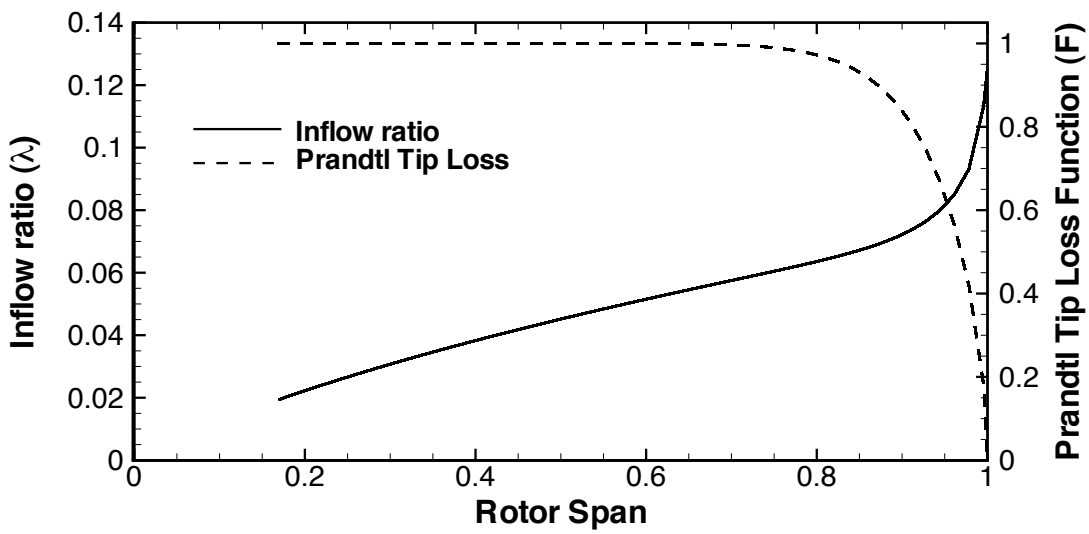

Figure 3.5: Inflow ratio and Prandtl's tip loss function for a two bladed rotor obtained from combined blade element and momentum theory.

Figure 3.5 shows the BEMT results of a representative rectangular two bladed rotor with an NACA 0012 airfoil section. The predicted inflow ratio (non-dimensional ratio of induced velocity to the rotor tip speed) at the tips are unusually high for the rotor. This is due to the fact that 2D theory was used to obtain the induced velocity and the only mechanism to reduce the load at the tip is to decrease the angle of attack of the blade to zero. This is achieved by increasing the induced velocity (inflow ratio) near the tip of the blade. This is the primary reason for the Prandtl's tip loss correction not being used directly in the BET-CFD calculations. In CFD, the reduction in load will result in reduction in induced velocity unlike the BEMT where the velocity would increase to satisfy mass conservation.

A second type of tip correction is employed in the present work for coarse

grids. In coarse grids the number of divisions in the span-wise direction of the blade is small, typically less than 10 cells covering the blade span. Therefore, the sharp drop in the source term to zero near the tip is never captured. When one compares the source term value at the cell center of the cell containing the tip region and the immediate next neighbor, a huge jump in source term value occurs. This results in numerical instability with a disturbance growing near the tip and propagating towards the center. In such cases a half cosine function, which is unity at a particular radial location and zero at the tip, is used to correct the loads. The radial location at which the function is unity is called the tip correction distance and is denoted by r_{tip}. The function is shown in equation (3.14). This function removes the instability for coarse grids and stabilizes the calculations. Typical values used for r_{tip} are $0.8 - 0.85\mathcal{R}$.

$$F = \cos\left[\frac{\pi}{2}\left(\frac{r - r_{tip}}{\mathcal{R} - r_{tip}}\right)\right], \;\; r_{tip} \leq r \leq \mathcal{R} \tag{3.14}$$

3.2 Source Term

The force generated by each elemental section of the blade dr can be determined using BET as explained in the previous section. This force has to be introduced into the governing equations as an equivalent forcing term to determine the induced velocity for the BET calculation. An additional "work done" term W_d has to be introduced into the energy equation to account for the increase in internal energy by work addition. The rotor modeling procedure thus centers around the development of these two terms. In equation (3.2), the body force term $\mathbf{f}$ is a volumetric term having the units of force per unit volume. In BET one idealizes the blade as an infinitely thin line connecting the Aerodynamic Center of each blade section generating lift and drag as show in figure 3.6. This force per unit span $\mathbf{f}(r)$ can be converted into a body force term (force per unit volume) employing impulse functions as shown in equation (3.15).

$$\mathbf{f} = \mathbf{f}(r)\delta(\xi - \xi_0)\delta(\eta - \eta_0) \tag{3.15}$$

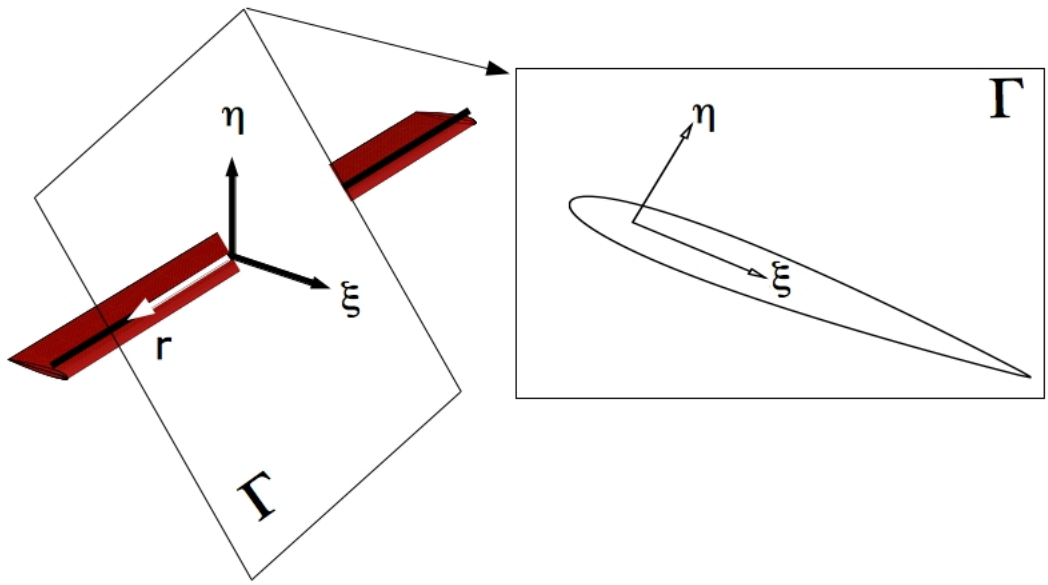

Figure 3.6: Actuator line approximation of a real blade.

The properties of the Dirac delta function, are shown in equations (3.16) and (3.17). The coordinates (r, ξ, η) are illustrated in figure 3.6 and (ξ_0, η_0) is the location of the actuator line in the $\mathbf{\Gamma}(\xi, \eta)$ plane. It is evident from equation (3.16) that $\delta(x)$ has reciprocal unit of x (length), hence $\delta(\xi - \xi_0)\delta(\eta - \eta_0)$ has reciprocal unit of area.

$$\int_{-\infty}^{\infty} \delta(x)dx = 1 \tag{3.16}$$

$$\int_{-\infty}^{\infty} f(x)\delta(x-a)dx = f(a) \tag{3.17}$$

In practical numerical computation it is not possible to represent a delta function exactly. Therefore, the body force $\mathbf{f}$ is regularized by convolution with a unit area Gaussian kernel. Convolution with the kernel spreads the impulse/singularity along the (ξ, η) plane over a finite distance determined by the standard deviation $(\sigma_\xi, \sigma_\eta)$. Mikkelson[18] adopted a similar approach and the regularized body force

term f_ϵ is shown in equation (3.18).

$$f_\epsilon = \frac{1}{2\pi\sigma_\xi\sigma_\eta} f_r \exp\frac{(\xi-\xi_0)^2}{2\sigma_\xi^2} \exp\frac{(\eta-\eta_0)^2}{2\sigma_\eta^2} \tag{3.18}$$

Regularization of an impulse function in single dimension (arrow pointing up) is illustrated in figure 3.7. Here three different values for standard deviation 0.1,0.2 and 0.5 (increasing order of smoothing distance) were used to smooth the unit impulse function. A real rotor blade has finite thickness and area, therefore, in the present work the standard deviation values were specified using the blade length scales. In the chord-wise direction ξ the σ_ξ value was chosen to be between $\frac{1}{3}$ to 1 root chord and in the thickness direction η the standard deviation σ_η was chosen between $\frac{1}{30}$ to $\frac{1}{10}$ root chord.

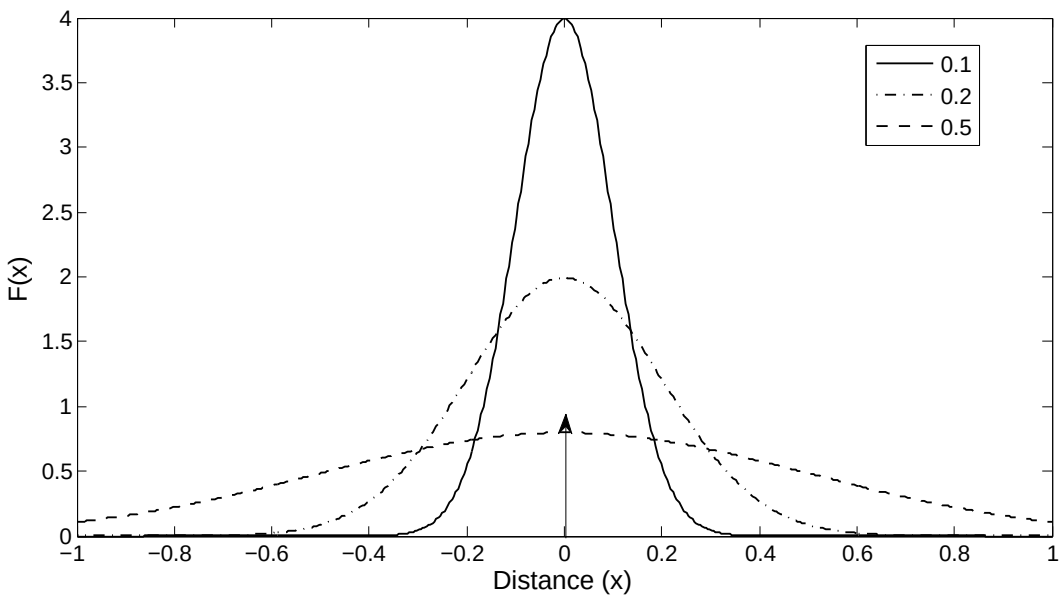

Figure 3.7: Regularization of an unit impulse function using gaussian kernel.

The work addition to the fluid by the rotor body force term W_d can be determined using control volume analysis (figure 3.8). V is the volume in which the rotor body force term exists (defined by the surface Ω) and is completely contained inside the fluid control volume CV. The fluid velocity over the volume element shown in figure (3.8) is defined by $\mathbf{u_s}$. Let $\mathbf{w}$ be the fluid velocity induced as a result of the body force $\mathbf{f}$, which is the difference between the velocity over the

volume element and the free stream velocity $\mathbf{v_{free}}$, $\mathbf{w} = \mathbf{u_s} - \mathbf{v_{free}}$. Then the work done by this body force is the volume integral of the scalar product of $\mathbf{w}$ and $\mathbf{f}$ as shown in equation (3.19).

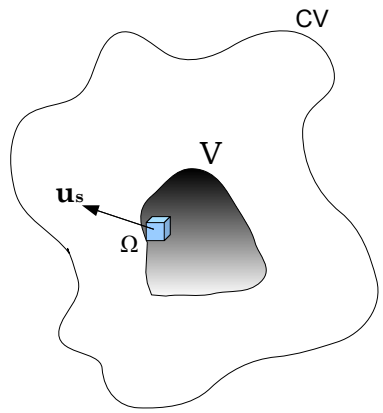

Figure 3.8: Control volume to determine work done by rotor body force term.

$$W_d = \oiiint_{\Omega} \mathbf{w} \cdot \mathbf{f} d\Omega \tag{3.19}$$

This completes the actuator line model for the rotor.

The flow field required to determine the parameters like the angle of attack (α) and induced velocity ($\mathbf{w}$) are obtained from Computational Fluid Dynamics (CFD) solver using the initial guess (blade loads obtained assuming zero induced velocity in BET) for the source terms. The coupling between the actuator line model and the CFD solver are explained in detail in the next chapter.

3.3 Summary

The body force $\mathbf{f}$ and the work term W_d obtained using the above analysis are used to mimic the presence of the rotor in the flow field. The governing equations of fluid dynamics are discretized and solved along with the source term to yield the flow field due to the presence of the rotor. Only gross (lower order) aerodynamic effects of the rotor on the flow can be captured, since the effect of the wall is modeled analytically using forcing terms. In addition, only the spawise variation is specified for the forcing terms while the chordwise variations are neglected. The

line source rotates along with the blade in the computational domain continuously adding momentum and energy (equivalent of the real rotor) to the fluid. The angle of attack, α, resultant velocity, V_{rel}, are obtained from the flow field calculation and the forcing terms are obtained from the forces per unit length - calculated using α and V_{rel}. The source term calculation and the flow field calculation are thus coupled using the BET. The complete numerical implementation of the forcing terms in the discretized governing equation and flow solution procedure are discussed in detail in chapter 4.

Chapter 4

Finite Volume Flow Solver

4.1 Overview

In the previous section, the body force and work terms necessary to model the rotor in the governing fluid dynamics equations were presented. The coupling of the BET with CFD, and the numerical implementation was postponed until the present chapter for better continuity. It was pointed out in [10] that structured body conforming grid are best suited for acoustics. A cylindrical grid system best fits the rotating actuator line if the axis of rotation and the center of the cylindrical grid coincide. Additionally, as explained in chapter 2, numerical error in loads must be minimized in order to have accurate loading noise prediction. In a cylindrical grid system, interpolation of the CFD flow field is not required for the source term calculation. This eliminates numerical error due to interpolation of blade loads, for example, an actuator line embedded in a Cartesian grid would generate large numerical error along the azimuth. This is because the cells do not align to the actuator line as the line cuts through the Cartesian cells non-uniformly. Numerical errors are generated as the line representing the rotor sweeps through the Cartesian grid - due primarily to interpolation inaccuracies. This leads to unsteady loads that are purely numerical in nature and are a problem when given as input for noise prediction. These numerical oscillations cannot be removed from the time history by filtering or smoothing, since they do not occur in a specific frequency range.

The main drawback of the structured cylindrical grid system is the existence of a geometric singularity at the origin. This problem has been investigated by very

few authors in literature due to its complexity. Mosheni and Colonius[43] proposed a staggered grid arrangement to overcome the centerline singularity for finite difference schemes. This method was found to yield spurious oscillations even with High Accuracy Compact schemes with spectral-like resolution[44]. In reference [44], the authors reported the use of an explicit filter to control the oscillations - with some success. A new centerline treatment was proposed by the same authors and was found to yield excellent results without the use of the explicit filter. Hixon et al.[45] carried out error analysis of compact schemes applied to cylindrical coordinates. The authors attributed the origin of the centerline instability to the formulation of the governing equations and illustrated the accuracy and stability of a properly formulated centerline singularity.

The focus of the present work is acoustic design calculations, therefore, one cannot afford to use computationally expensive high accuracy compact schemes for flux calculations. Addition of the rotor source term in the governing equation may tend to make the equations stiff, which can potentially lead to stability problems in high accuracy schemes. Using unstructured finite volume method on a structured cylindrical grid helps avoid the centerline singularity (as the equations are solved in Cartesian coordinates), while maintaining good stability properties. The regularity in the cylindrical grid helps reduce interpolation errors in the blade loads. In such an unstructured cylindrical grid, at the center, the hexahedral cells degenerate into triangular prismatic cells. Although the centerline singularity is avoided, increasing azimuthal resolution can lead to highly skewed cells at the center of the cylindrical grid. Since skewness is a key factor in determining solution quality & stability, it is necessary to avoid such skewed cells at the center. In the present work, the prismatic cells at the center are combined together to form a single polyhedral cell as shown in figure 4.1. Without the centerline treatment, fine grids of azimuthal resolution of about 3° or less were found to yield spurious numerical waves at the centerline. With the centerline treatment, such oscillations were suppressed and a robust computation was possible. Ma et al.[46] have reported good results using a similar method for a 2D incompressible flow problem in polar coordinates. Considering the above advantages, an unstructured finite volume method on structured cylindrical mesh is the adopted solution procedure for the flow field.

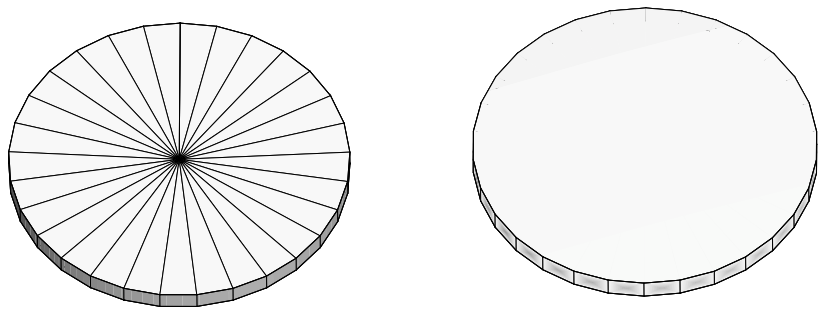

Figure 4.1: Polyhedral cell formed by combining triangular prisms at grid center.

4.2 Governing Equations

The governing equations used for the CFD calculations are the compressible Euler's equations in Cartesian coordinates. The equations were introduced in differential form in equations (3.1-3.3), but for the finite volume discretization, the integral form of the equations is employed. The integral equations in vector form is shown in equation (4.1).

$$\oiiint_V \dot{Q} dV + \oiint_S \mathbf{n} \cdot \mathbf{F} = \oiiint_V G dV \tag{4.1}$$

where,

$$Q = \begin{bmatrix} \rho \\ \rho u \\ \rho v \\ \rho w \\ e \end{bmatrix}, \quad F_n = \mathbf{n} \cdot \mathbf{F} = \begin{bmatrix} \rho \bar{u} \\ \rho u \bar{u} + p n_x \\ \rho v \bar{u} + p n_y \\ \rho w \bar{u} + p n_z \\ e \bar{u} + p u_n \end{bmatrix} \quad and \;\; G = \begin{bmatrix} 0 \\ f_x \\ f_y \\ f_z \\ \mathbf{u} \cdot \mathbf{f} \end{bmatrix}$$

The vector $\mathbf{n}(n_x, n_y, n_z)$ is the unit outward pointing normal of the surface of integration S and the rotor body force term is $\mathbf{f}(f_x, f_y, f_z)$ present inside the volume V. The dot on top of any variable denotes differentiation with respect to time. The fluid velocity vector is $\mathbf{u}(u, v, w)$ and the grid velocity is denoted by $\mathbf{v}$. The quantity $u_n = \mathbf{n} \cdot \mathbf{u}$ and $v_n = \mathbf{n} \cdot \mathbf{v}$ are the velocity components in the normal direction. Similarly, we have $\bar{u} = \mathbf{n} \cdot (\mathbf{u} - \mathbf{v}) = u_n - v_n$. The complete rotor source vector is denoted by G and contains both the body force and work term.

4.3 Finite Volume Discretization

The volume integrals in equation (4.1) are evaluated using the cell center value Q_c (piecewise constant) and the cell volume V_c as shown in equation (4.2).

$$\oiiint_V Q dV \approx Q_c V_c \tag{4.2}$$

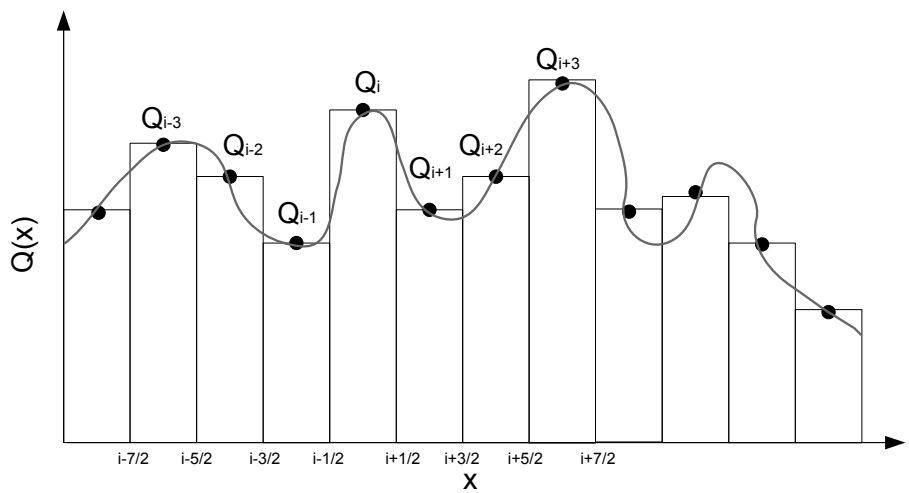

Figure 4.2: Piecewise-constant reconstruction for 1D system.

In this piecewise-constant reconstruction one has to solve a local Riemann problem at every edge indicated by the fractional indices $i+1/2$, $i-1/2$ shown in figure 4.2. The face average flux F_n (piecewise-constant) is approximated as the face center value and it is obtained by solving the Riemann problem at the cell edge (given the left and right states). Introducing the above approximations, the discretized equation can be written as shown in equation (4.3).

$$\dot{Q}_c + \sum_i^n \frac{F_n S_i}{V_i} = G_c \tag{4.3}$$

The flux F_n is evaluated using Roe's Approximate Riemann solver[47] using the left and right states of a face Q_L and Q_R as shown in equation (4.4).

$$\hat{F}_{roe}(Q_L, Q_R, S) = \frac{1}{2}\left[\hat{F}(Q_L, S) + \hat{F}(Q_R, S) - \|\tilde{A}(Q_L, Q_R, S)\|(Q_R - Q_L)\right] \tag{4.4}$$

Where, $\tilde{A}$ is the Roe average Jacobian matrix given in equation (4.5). The form of the Jacobian shown here is from Chen[11] and is rearranged in a different manner as compared to Roe's original formulation.

$$\|\tilde{A}\|(Q_R - Q_L) = \begin{bmatrix} \alpha_4 \\ \tilde{u}\alpha_4 + n_x\alpha_5 + \alpha_6 \\ \tilde{v}\alpha_4 + n_y\alpha_5 + \alpha_7 \\ \tilde{w}\alpha_4 + n_z\alpha_5 + \alpha_8 \\ \tilde{H}\alpha_4 + \tilde{u_n}\alpha_5 + \tilde{u}\alpha_6 + \tilde{v}\alpha_7 + \tilde{w}\alpha_8 - \frac{\tilde{c}^2}{\gamma-1}\alpha_1 \end{bmatrix} \tag{4.5}$$

Where,

$$\begin{aligned} \alpha_1 &= \|S\|\|\tilde{\bar{u}}\|(\Delta\rho - \frac{\Delta p}{\tilde{c}^2}) \\ \alpha_2 &= \|S\|\|\tilde{\bar{u}} + \tilde{c}\|\frac{(\Delta p + \tilde{\rho}\tilde{c}\Delta\tilde{u})}{2\tilde{c}^2} \\ \alpha_3 &= \|S\|\|\tilde{\bar{u}} - \tilde{c}\|\frac{(\Delta p - \tilde{\rho}\tilde{c}\Delta\tilde{u})}{2\tilde{c}^2} \\ \alpha_4 &= \alpha_1 + \alpha_2 + \alpha_3 \\ \alpha_5 &= \tilde{c}(\alpha_2 - \alpha_3) \\ \alpha_6 &= \|S\|\|\tilde{\bar{u}}\|(\tilde{\rho}\Delta u - n_x\tilde{\rho}\Delta\tilde{u}) \\ \alpha_7 &= \|S\|\|\tilde{\bar{u}}\|(\tilde{\rho}\Delta v - n_y\tilde{\rho}\Delta\tilde{u}) \\ \alpha_8 &= \|S\|\|\tilde{\bar{u}}\|(\tilde{\rho}\Delta w - n_z\tilde{\rho}\Delta\tilde{u}) \end{aligned} \tag{4.6}$$

The tilde on top of a variable denotes the Roe average value of the variable and is defined as shown in equation (4.7). Here u should be replaced by the appropriate variable for which Roe average is required.

$$\tilde{u} = \frac{\sqrt{\rho_L}u_L + \sqrt{\rho_R}u_R}{\sqrt{\rho_L} + \sqrt{\rho_R}} \tag{4.7}$$

The operator $\Delta\rho = \rho_R - \rho_L$ denotes the difference between the value of the left and right states.

The discrete equation shown in equation (4.3) can be rearranged and written in a semi-discrete form as an Ordinary Differential Equation (ODE) shown in equation (4.8). The operator L consists of the discrete flux operator and the contribution

due to source term. Two types of explicit time integration method have been implemented to solve this ODE - Runge Kutta integration scheme of order two (RK2) and order four (RK4). The RK4 scheme is the same used by Jameson[48] and is shown in equation (4.9).

$$\dot{Q} = L[Q] \tag{4.8}$$

$$\begin{aligned} Q^{(1)} &= Q^n + \frac{\Delta t}{2} L[Q^n] \\ Q^{(2)} &= Q^n + \frac{\Delta t}{2} L[Q^{(1)}] \\ Q^{(3)} &= Q^n + \Delta t L[Q^{(2)}] \\ Q^{n+1} &= Q^n + \frac{\Delta t}{6} \left(L[Q^n] + 2L[Q^{(1)}] + 2L[Q^{(2)}] + L[Q^{(3)}] \right) \end{aligned} \tag{4.9}$$

For each sub-step in the Runge Kutta time integration shown in equation (4.9) the rotor source term $G^{(i)}$ (contained inside the operator L), where i denotes the current sub-step, has to be calculated. The term $G^{(i)}$ contains the body force and work terms, which require the flow-field values, $Q^{(i)}$, at the current sub-step i. But $Q^{(i)}$ is an unknown quantity and is dependent on both $G^{(i)}$ and the flux F. An implicit numerical procedure is required to solve for the flow-field and source term, which is computationally expensive. The term $G^{(i)}$ merely consists of force and work addition by the blade as it rotates in the fluid medium. Introducing this term into the governing equation does not significantly increase its stiffness because the source and flow-field have time scales (approximately) of the same order. Then a computationally efficient way to solve the equations is to use the flow-field values at the previous sub-step $Q^{(i-1)}$ to calculate the source $G^{(i)}$.

4.4 Source term - finite volume solver coupling

As described above, the rotor flow-field information at the previous time step $Q^{(i)}$ is used to determine the source term $G^{(i)}$. The BET is used to obtain the components of the source term $G^{(i)}$. The necessary input for BET are the local angle of attack of the blade section α and induced velocity vector $\mathbf{w}$. These values are obtained from the CFD solution using suitable interpolation. In the present study, a cylindrical mesh is employed with the grid center coincident with the axis of rotation of the

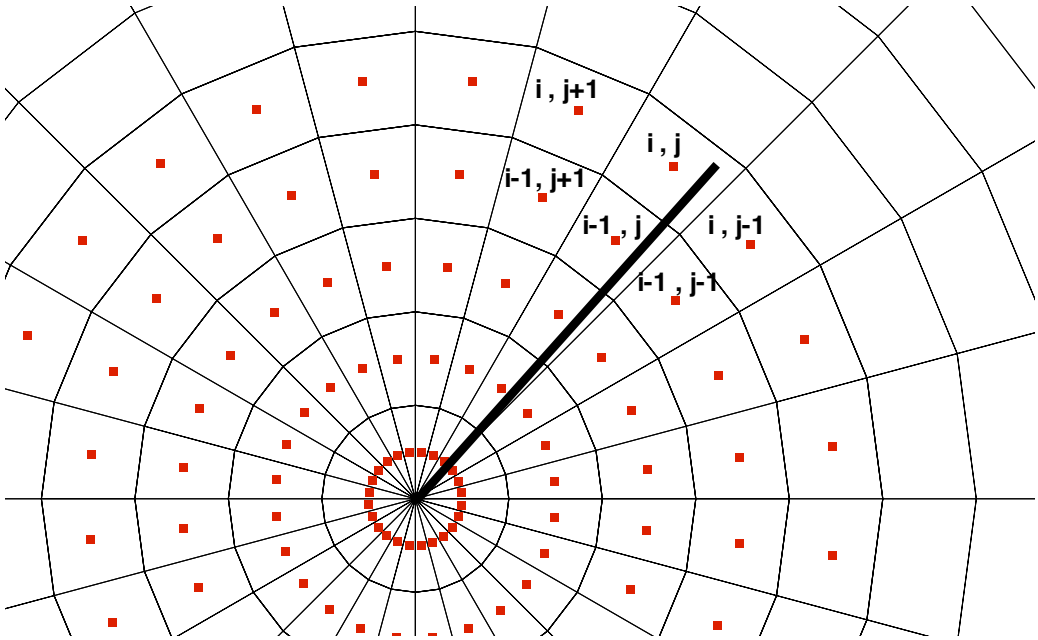

Figure 4.3: Interpolation of field velocity to the actuator line.

actuator line. A typical setup used in the interpolation is shown in figure 4.3. If the actuator line is divided into the same number of radial divisions as the grid (dr) then the value at the grid cell center directly gives the flow-field value at the actuator line. In the numerical implementation, a zeroth order integration is preformed for the volume integral term, shown in equation (4.2). Therefore, it is necessary to apply a suitable limiter before the flow-field values are transferred to the actuator line to reduce numerical error. The following limiter is employed in the present work.

$$\tilde{\mathbf{u}}_{\mathbf{i}} = \max(\mathbf{u}_{\mathbf{i,j+1}}, \mathbf{u}_{\mathbf{i,j}}, \mathbf{u}_{\mathbf{i,j-1}}) \tag{4.10}$$

where, "max" denotes the maximum ($\tilde{\mathbf{u}}_{\mathbf{i}}$) of the specified values $\mathbf{u}_{\mathbf{ij\pm1}}$ and $\mathbf{u}_{\mathbf{ij}}$, which are the cell center values indicated in figure 4.3. The induced velocity vector $\mathbf{w}$ can then be calculated using the equation below,

$$\mathbf{w} = \tilde{\mathbf{u}}_{\mathbf{i}} - \mathbf{v} \tag{4.11}$$

where, $\mathbf{v}$ is the grid velocity. Once $\mathbf{w}$ is obtained the resultant velocity V_{rel} and sectional angle of attack α can be found using the velocity triangle in figure 3.3.

The lift and drag forces per unit length are obtained using equation (3.8). The forces are then regularized by convolution with the Gaussian kernel, with specified standard deviation (spreading distance), as shown in equation (3.18). Thus, the blade load calculation using BET and flow-field calculation by CFD are coupled and are solved iteratively each time step. The loads take a few revolutions to settle to a trim solution or steady value. The time history of the loading data is trimmed upto the specified number of revolutions and the rest is used to make loading noise prediction as explained in chapter 2.

4.5 Parallelization of solver

A simple strategy is adopted to partition the grid using structured cylindrical grid information. The grids are partitioned into blocks of equal size along the Z direction such that number of blocks is equal to the number of processors used for the computation. The individual blocks are padded with a layer of ghost cells (both top and bottom) which accept data from the neighboring block. The data exchange algorithm is illustrated in figure 4.4, the computational cells are colored by their respective block index and the ghost cells are colored by neighboring block index that donates to that particular block. The exchange takes place after every sub-iteration of the Runge Kutta time integration. The regularized rotor source values are assigned to all cell centers of the computational domain. This task is computationally expensive and is avoided in the present work by isolating the rotor sources to one particular block. The block containing the rotor sources is identified and the regularized sources are added only to that particular block's cell centers. In all other grid blocks a zero source value is assigned.

The main aim of the work is to add an extra layer to a low fidelity rotor model into a larger suite of tools, for acoustic design calculation, called Immersed Boundary Solver for Environment Noise (IBSEN), which requires the finite volume solver with the source terms in a limited region near the rotor. This makes the parallelization unnecessary in the actual application of the solver. The parallelization is performed only to obtain faster results from the finite volume solver in order to demonstrate the proof of concept. The implementation of the method in IBSEN is explained in detail in chapter 5.

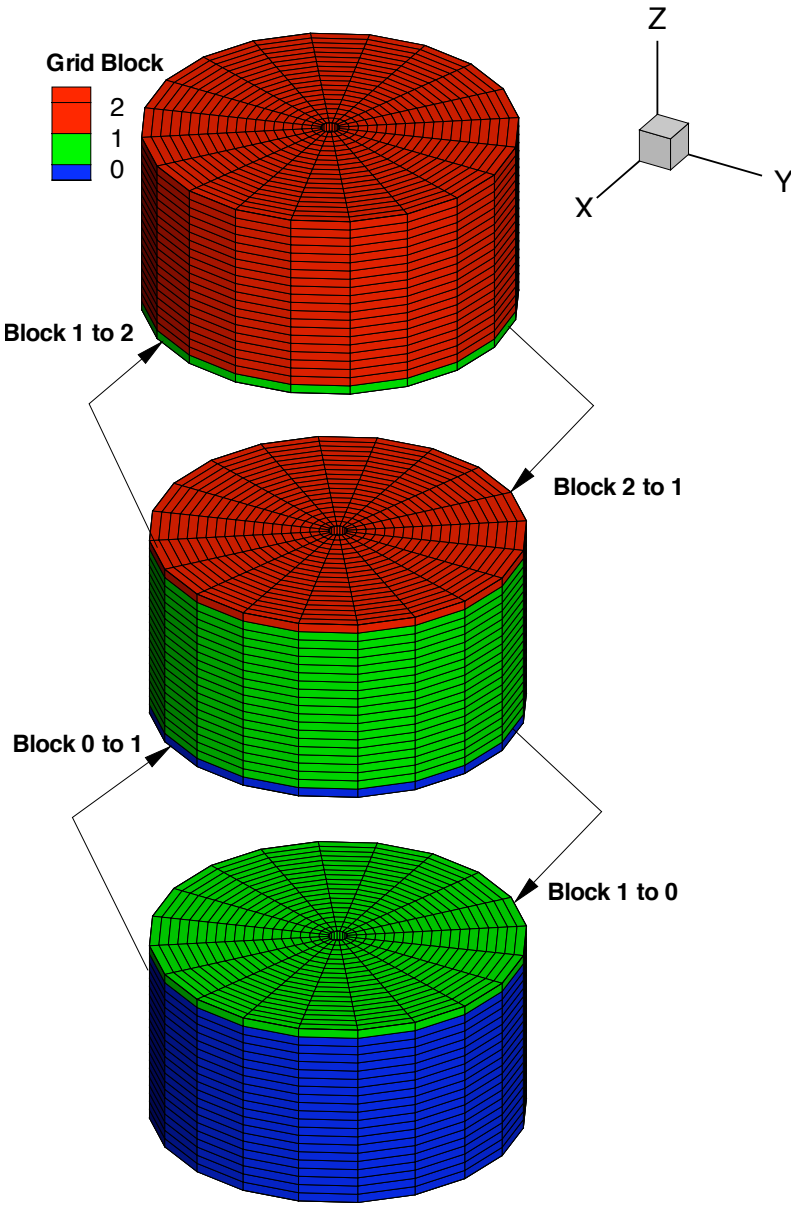

Figure 4.4: Parallel data exchange between individual grid blocks.

4.6 Algorithm

The complete derivation of the actuator model was presented in chapter 3. The coupled BET-CFD numerical procedure use to solve for the blade loads and flow-field of rotors was presented in this chapter. The loads thus obtained are used to predict loading noise generated by the rotor (compact chordwise loading approxi-

mation) using the acoustic code, PSU-WOPWOP as discussed in chapter 2. Before presenting the proof of concept of the numerical procedure using a test case, the complete coupled BET-CFD method is summarized as steps shown below. The procedure is also illustrated as a flow chart in figure 4.5.

Step 1 The rotor parameters are read from an input file and the BEMT is run to obtain the Prandtl's tip loss function F, which will be used for correcting the loads near the blade tips for the entire BET-CFD calculations.

Step 2 The CFD grid blocks are generated and are initialized with free-stream conditions. Using the free-stream values as initial conditions and assuming zero induced velocity the BET is used to calculate the blade loads per unit length $\mathbf{f}(r)$. The loads are corrected by multiplying with the tip loss function F obtained in step 1.

Step 3 Regularization of the load is performed using prescribed standard deviation from input file. If $\mathbf{x}$ is the location of cell center of an arbitrary cell in the domain, $\hat{\mathbf{r}}$ is the unit radius vector of the actuator line, $\hat{\mathbf{r}}_\perp$ is the unit vector normal to $\hat{\mathbf{r}}$ (parallel to Γ), z_{loc} is the location of rotor in the z-plane and z_c, r_c are the z and r (radial coordinate $\sqrt{x^2+y^2+z^2}$) coordinate of the cell center containing the rotor line source then, the regularized body force term $\mathbf{f}_\epsilon$ can be defined as,

$$\mathbf{f}_\epsilon = \frac{1}{2\pi\sigma_\xi\sigma_\eta}\mathbf{f_r}\exp\left(\frac{r^2(\hat{\mathbf{r}}\cdot\hat{\mathbf{r}}_\perp)^2}{2\sigma_\xi^2}\right)\exp\left(\frac{(z_{loc}-z_c)^2}{2\sigma_\eta^2}\right)$$

The coordinates x, y, z are defined in figure 3.3 and r, ξ, η are defined in figure 3.6.

Step 4 The "work done" term is calculated using equation (3.19) based on the regularized body force term $\mathbf{f}_\epsilon$ obtained in step 4 and velocity at the particular cell center. The CFD fluxes are calculated using the numerical scheme explained in § 4.3 along with the calculated body force and work done source terms.

Step 5 The RK4/RK2 time integration is performed to yield the flow-field values for the next sub step. Now the velocity at the actuator line is determined

using the cell centers cut by the actuator line. Since a zeroth-order volume integration for the sources are performed a limiter is applied (equation (4.10)) to the cell center velocity values to reduce numerical oscillations. The actuator line along with the cell centers cut by it are illustrated in figure 4.3.

Step 6 Data is exchanged between the grid blocks and BET is used to recalculate the loads based on the new flow-field values.

Step 7 The steps 4 to 6 are repeated for each sub-step and time step of the time integration till a correct rotor state is reached. The correct state is reached when a constant non-dimensional rotor thrust is obtained or when the trim loop is converged.

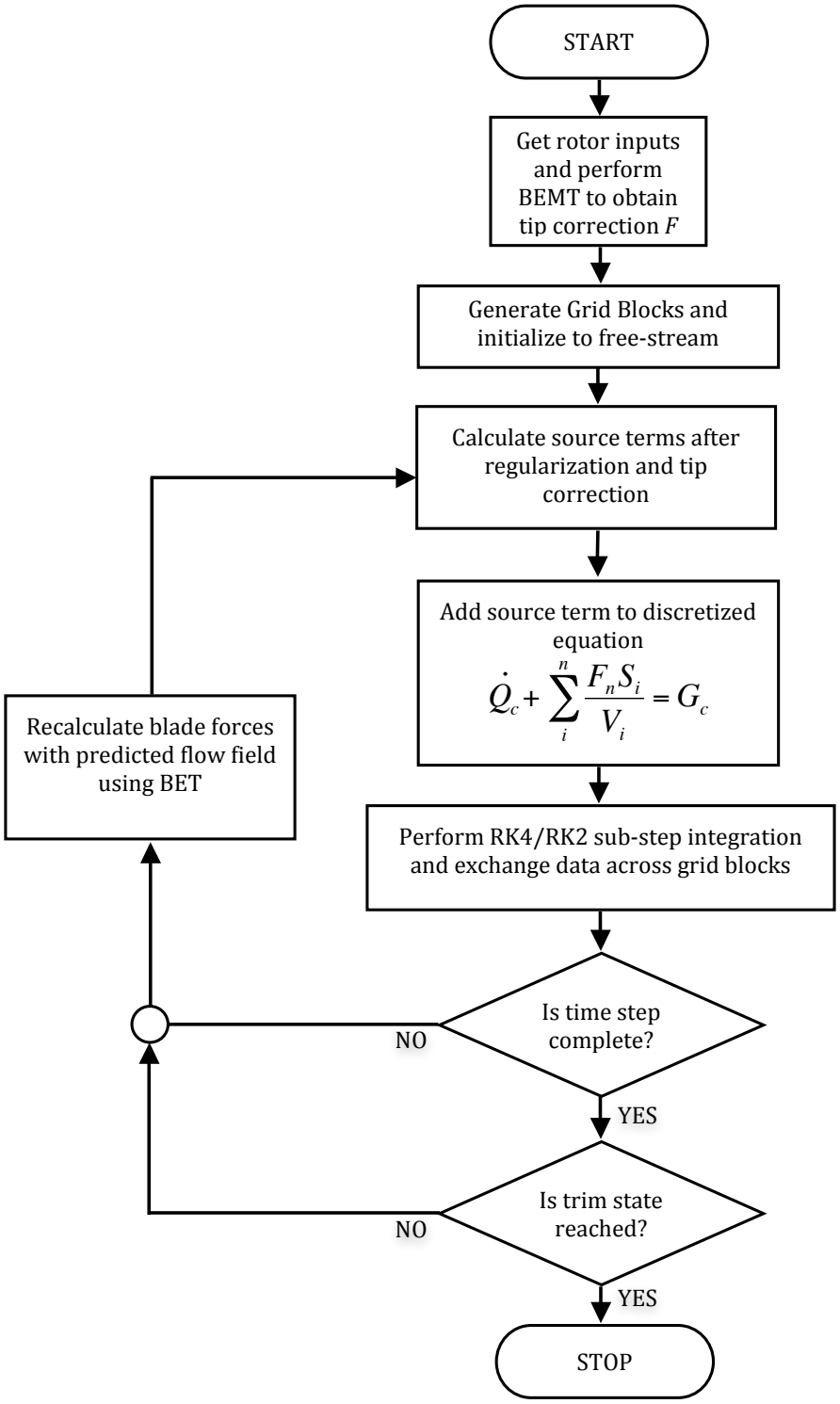

Figure 4.5: Flow chart of the BET-CFD coupled simulation.

4.7 Results

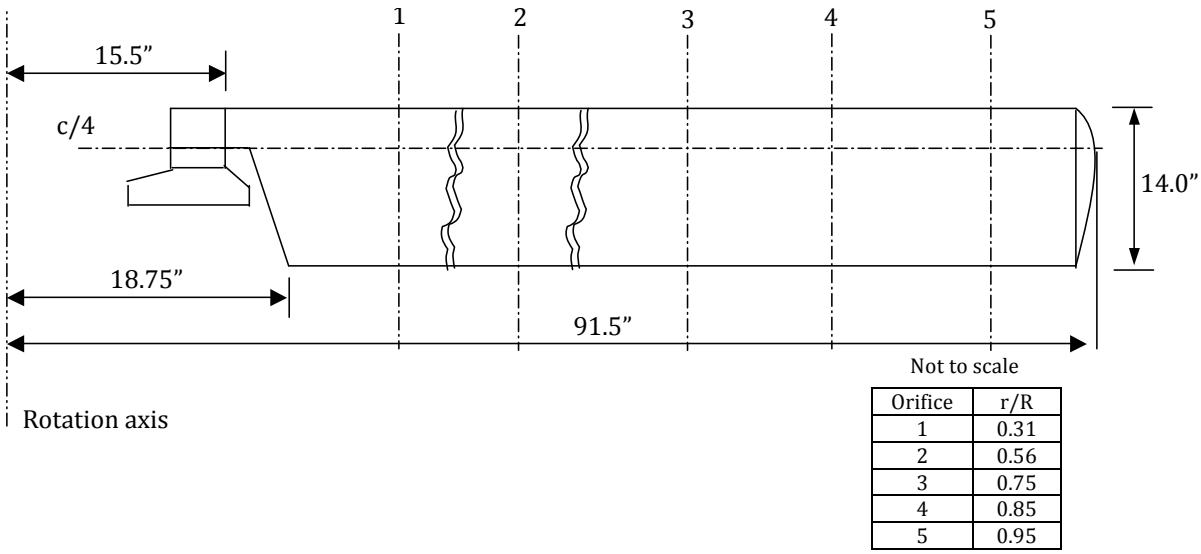

Figure 4.6: Blade layout showing location of pressure orifices numbered from 1-5.

The proposed rotor model in the finite volume solver has been validated using the experimental data by Rabott[49]. In reference [49], the spanwise loading of an isolated rotor in hover was measured for various rotor tip speeds and collective pitch angles. The details of the rotor used in the experiment are provided in table 4.1 and the spanwise location of the pressure taps (on the blades) used to measure the blade forces are indicated in figure 4.6. The unstructured finite volume solver with the actuator line source was used to simulate a case from reference [49], namely, tip speed of 122.5 ms^{-1} and collective pitch of 12° and experimentally measured non-dimensional thrust coefficient C_T of 0.00708.

The source term calculation involves the specification of input parameters from the user, namely, the standard deviation of the Gaussian kernel σ_ξ and σ_η. The grids are equally spaced cylindrical mesh with radial spacing dr, axial spacing dz and azimuthal spacing $d\theta$. The extent of the domain along the radial direction is denoted by r_{max} and that of the positive and negative axial direction are denoted by z^+_{max} and z^-_{max} respectively. Two cases with different grid density were used to simulate the test case and the values used for parameters mentioned above are provided in table 4.2. In both cases of different grid density a zero gradient

boundary condition was employed at the outer boundary. The coarse grid and fine grids were run in parallel in two processors (two grid blocks).

Rotor Properties	
Number of blades	2
Rotor radius (R)	2.3241 m
Root chord (c)	0.3556 m
Solidity (σ)	0.097
Root cut out	0.3937 m
Blade aspect ratio	6
Collective pitch	12°
Airfoil section	NACA0012

Table 4.1: Properties of rotor used in CFD simulation

Parameter	Coarse grid	Fine grid
σ_ξ	$2c$	$2c$
σ_η	c	c
dr	0.1266 m	0.1266 m
$d\theta$	3°	2°
n_f	2	2
r_{max}	$5D$	$5D$
z^+_{max}	$5D$	$5D$
z^-_{max}	$10D$	$10D$
Processors	2	2

Table 4.2: Values of parameters used in the CFD simulations

4.7.1 Blade load convergence

In the proposed actuator line source method, the source strength (or blade load) is recalculated every time step using the flow-field values obtained at a previous time step as explained in chapter 3. Therefore, the primary validation necessary is to ensure the convergence of the source strength or blade load. Neglecting the effect of turbulence, for an isolated hovering rotor (present test case) the loads should necessarily reach a constant value w.r.t time upon convergence. Shown in figure 4.7 is the convergence history of load per unit span of the blade at non-dimensional radial locations (r/R) 0.844, 0.735, 0.626 and 0.354 for the coarse grid. The rotor

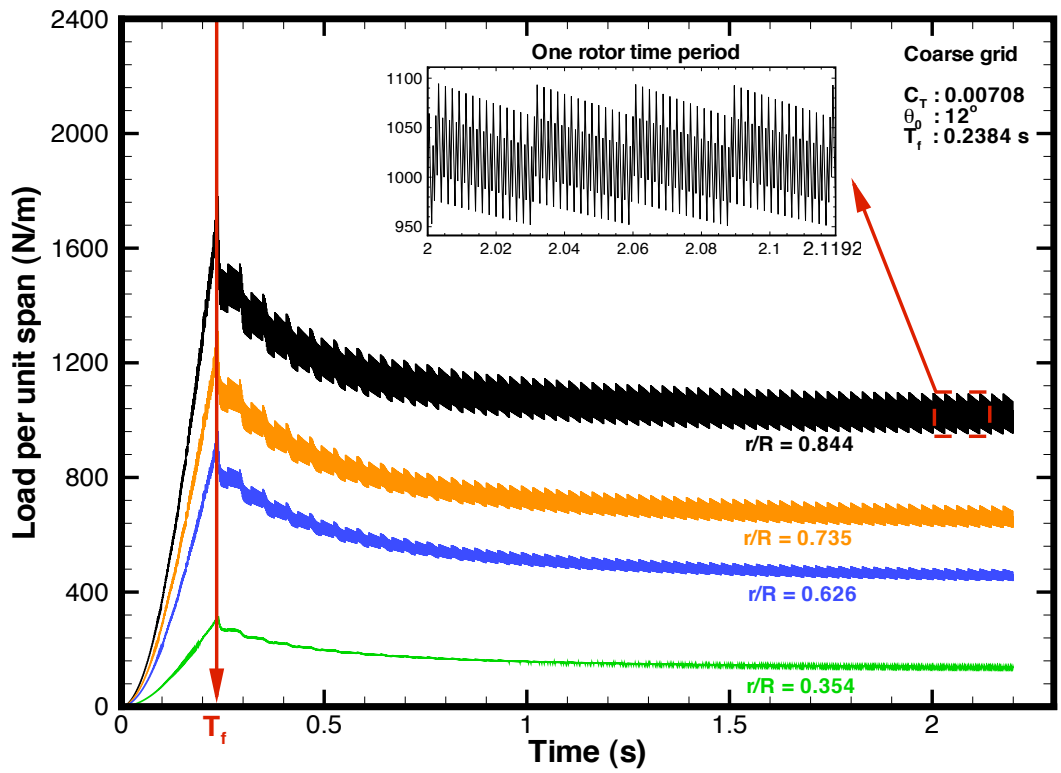

Figure 4.7: Blade load convergence history (coarse grid) at the indicated spanwise locations.

sources were not impulsively introduced with the full source value at time $t = 0$ to avoid numerical instability. The angular velocity of the rotor was gradually increased over a period of time T_f until the full value was realized, as follows. A linear profile for the angular velocity was chosen as shown in equation (4.12).

$$\Omega(t) = \begin{cases} \Omega_0 \left(\frac{t}{T_f}\right) & \text{if } t \leq T_f \\ \Omega_0 & \text{if } t > T_f. \end{cases} \tag{4.12}$$

where, $T_f = n_f(\frac{2\pi}{\Omega_0})$ is a time factor which determines the slope of the linear ramp function. The actual angular velocity of the rotor is Ω_0. The source strength is calculated based on the modified angular velocity $\Omega(t)$. In the present study, a value of 2 was chosen for n_f i.e., the source is ramped slowly to its full value in one rotor revolution. The time factor T_f used for the linear ramping of the rotor angular velocity is indicated in the figure. The load asymptotically converges to

a steady value, but the convergence is not uniform as the loads oscillate about a mean value, defined as the mean converged load. The time history is magnified and shown for one rotor time period in the sub-figure of figure 4.7. There are two distinct numerical wave forms present in the time history - (i) a rapid variation that occurs every azimuthal division (i.e. every 3° for coarse grid and 2° for fine grid) of the cylindrical grid and (ii) a slow variation that occurs every 90° rotor azimuth. In order to explain the error source of the high frequency oscillation occurring every azimuthal division, a simple demonstration case is presented. Consider a domain x with support $x \in (0, 1)$ to represent a single cell over which the Gaussian source is moving w.r.t time t with a unit velocity. The Gaussian function at various times ($t = 0, 0.5, 1.0$) are plotted in figure 4.8(b) and the mathematical form is show in equation (4.13). This function is integrated spatially using the zeroth order integration and is plotted w.r.t time along with the exact integral value $F(t)$ in 4.8(a).

$$f(x,t) = \exp\left[-100(x-t)^2\right] \qquad x \in (0,1) \quad t \in (0,1) \tag{4.13}$$

$$F(t) = \int_0^1 f(x,t)dx \quad t \in (0,1) \tag{4.14}$$

The results clearly demonstrate that the volume integration does not yield a constant source value. In addition, the numerical integration predicts a false peak instead of a constant value. Therefore, when the actuator sources move along the azimuth w.r.t time, the zeroth order integration predicts such false peaks in the integral value as the sources move from one cell to another. As a result, in a given cell, the maximum source value is observed when the peak of the gaussian kernel coincides with the cell center and a minimum when the peak has moved away. This error can be reduced by spreading the gaussian kernel further. But large spreading distance is contradictory to physics as the blade adds momentum to the fluid through the blade surfaces, whose geometry is fixed.

It is actually justified to remove any variation in load greater than or equal to the azimuthal spacing $d\theta$ because the given CFD scheme cannot resolve any scale smaller than $d\theta$ (Nyquist theorem). Therefore, one can use a low pass filter with cutoff frequency slightly less than that of the azimuthal spacing and remove these high frequency oscillations occurring every azimuthal spacing ($d\theta$) from the blade load because they cannot be eliminated with grid refinement (figure 4.10)

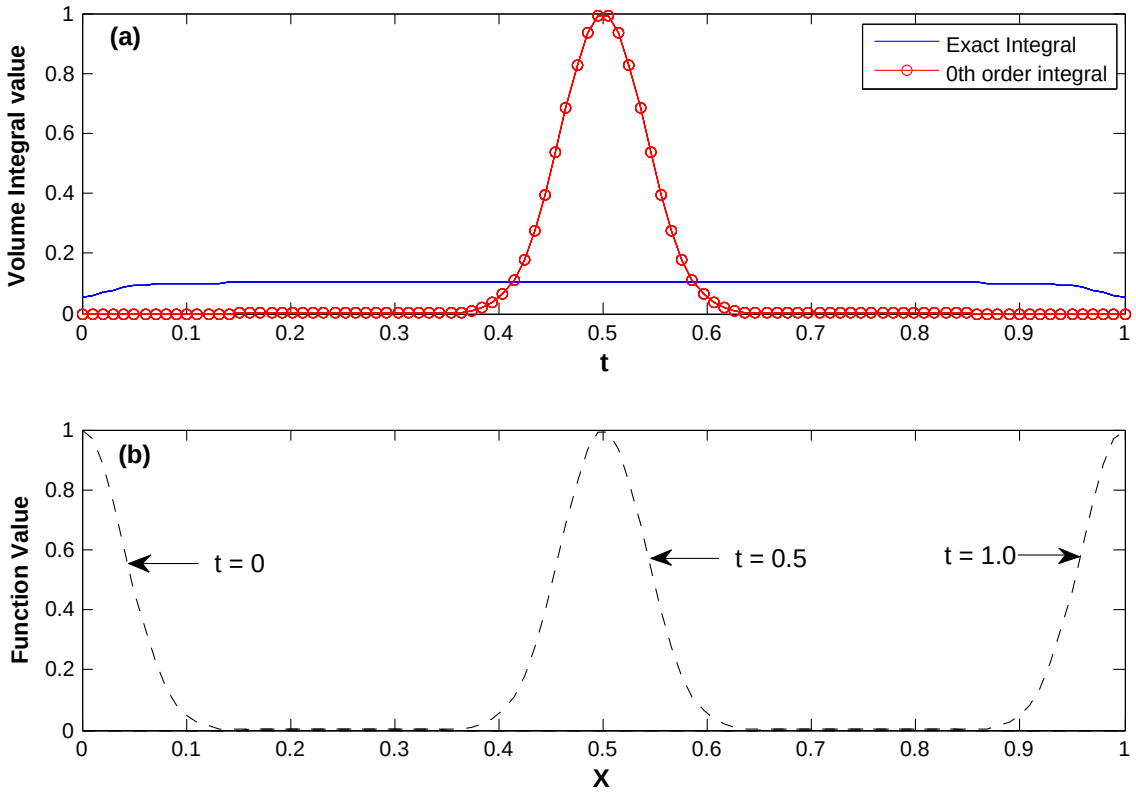

Figure 4.8: Illustration of high frequency error generated by the moving gaussian source due to the zeroth order volume integration.

unless the integral is evaluated exactly. Although there are many ways to perform the filtering, in the present work, the implicit time domain filter of Gaitonde and Visbal[50] was used to filter the loads. A time domain filter is best suited for aperiodic data and the implicit filter[50] has superior filter characteristics in the frequency domain compared to an explicit one of the same order[51]. The filtered load time history for the coarse grid is plotted in figure 4.9. The filter characteristics and properties such as the cut-off frequency can be found in detail in reference [52] and [50]. A brief note on the implementation details of the filter in the present work is provided in Appendix A. Although the high frequency oscillations are removed, the periodic saw-tooth oscillations occurring every 90^0 rotor azimuth exist even after filtering as shown in figure 4.9. They are problematic for acoustic prediction because the frequency of this error and the blade passage frequency are coincident. Hence they cannot be filtered because doing so would

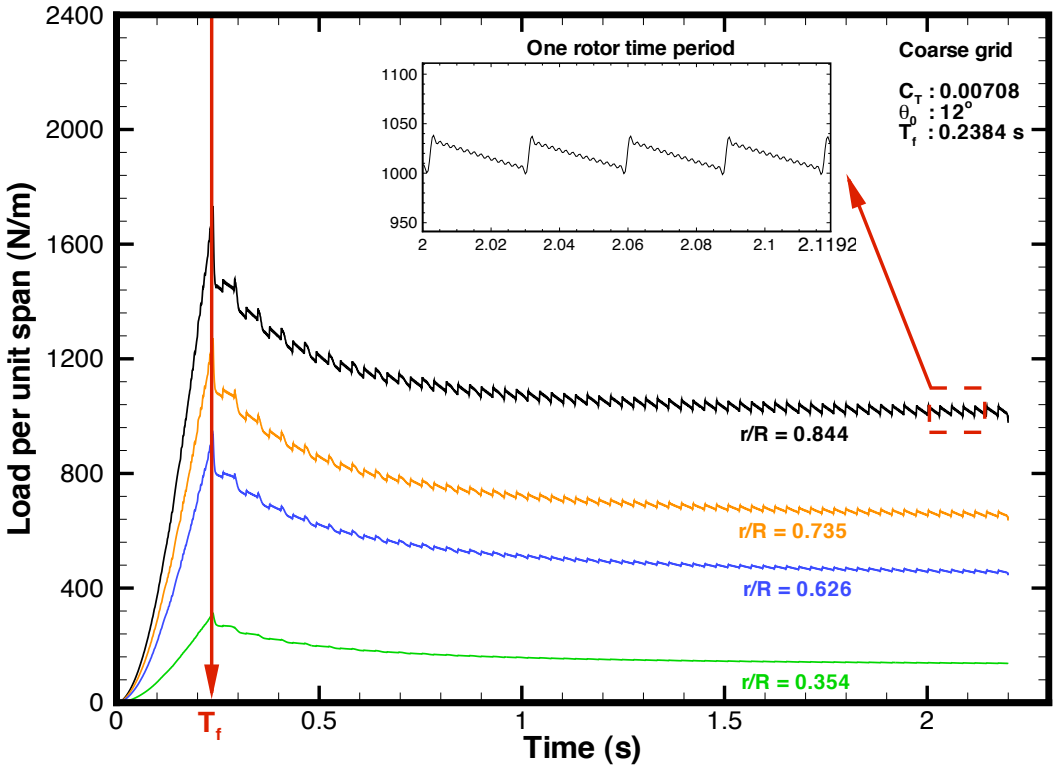

Figure 4.9: Filtered blade load convergence history (coarse grid) at the indicated spanwise locations.

remove almost all unsteady information in the blade loads. The oscillation in the load time history occurring every 90° was suspected to be a problem caused by the coarse nature of the grid. The coarse grid generates large false peaks in the rotor source term volume integration in turn affecting the flow solution. Therefore, the grid spacing in the azimuthal direction was decreased from 3° to 2° to confirm this fact and additionally conduct a grid dependence study. The unfiltered and filtered fine grid load time history are shown in figures 4.10 and 4.11 respectively at the same r/R positions as the coarse grid. The saw-tooth numerical oscillations that occurred every 90° for the coarse grid, occur every 60° for the fine grid indicating that the frequency of the error is grid dependent. Unlike the high frequency error whose source is the volume integration, the source of the low frequency error is suspected to be a combination of both the finite volume scheme and the volume integration of the sources. The error is significantly suppressed in the filtered case

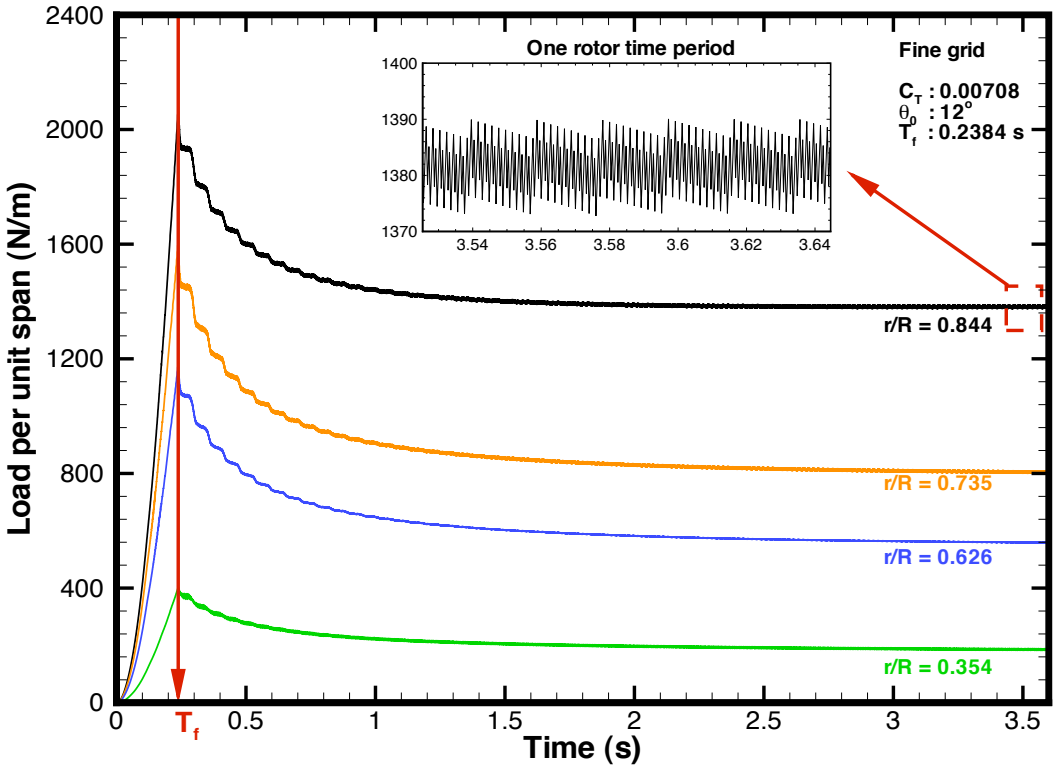

Figure 4.10: Blade load convergence history (fine grid) at the indicated spanwise locations.

as shown in figure 4.11 and the oscillations are less than 0.1% of the converged load, which is acceptable for acoustic design calculation. The investigation on the effect of the error on acoustics shall be conducted in the acoustic section to follow. In order to pin-point the exact source of the low frequency error more analysis and investigation has to be carried out and are proposed as future additions to the present work.

In section 4.3 of chapter 4 the rotor sources were calculated based on an approximate explicit scheme, which used the flow velocity at the previous time step. The sources have to be calculated implicitly because the source value and induced velocity are dependent on each other, but this process was avoided to save computational time. The residual error in the blade loads of this explicit formulation converges to zero non-monotonically with jump in load every 180° rotor revolution evident in the loading history. This is due to the fact that a blade of the rotor

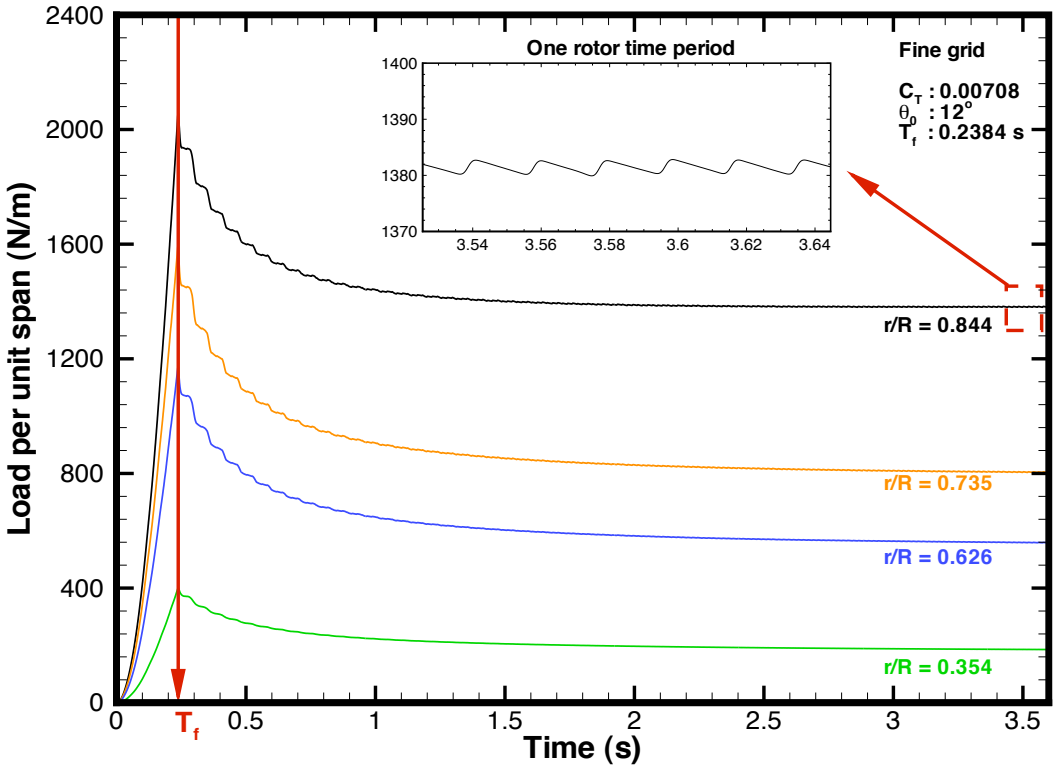

Figure 4.11: Filtered blade load convergence history (fine grid) at the indicated spanwise locations.

encounters the induced wake of another blade once every 180° thus generating this error. This error reduces with the flow-field induced by the source terms being sufficiently developed. Although the results shown above suffer from errors in the form of spurious numerical oscillations, employing a suitable frequency cut-off filter and correctly resolving the flow-field using a fine grid, it is possible to control this error and make the data suitable for acoustic prediction.

4.7.2 Blade load validation

In figure 4.12, the mean converged load per unit span at each span wise location for the coarse and fine grid cases are plotted. The experimental values from reference [49] are shown in red dots in the figure. The loads agree to within 1% for the coarse grid case at all span-wise location except the ones at the blade tip. The fine grid over predicts the span-wise loads compared to the experimental values especially

near the tip. The primary reason is that the convergence of the flow-field and hence the blade loads is quite slow due to the low damping of error by the fine grid compared to the coarse grid. Although the loads were obtained up to $t = 3.5s$, the loads are not fully converged and would take an unrealistically long time to reach the steady state value. Moreover, convergence acceleration using multi-grid methods or local time stepping is not possible since the source terms are evaluated in an unsteady manner. The loss in the non-dimensional thrust coefficient for the coarse and fine grids due to the tip correction are tabulated in table 4.3. The fine

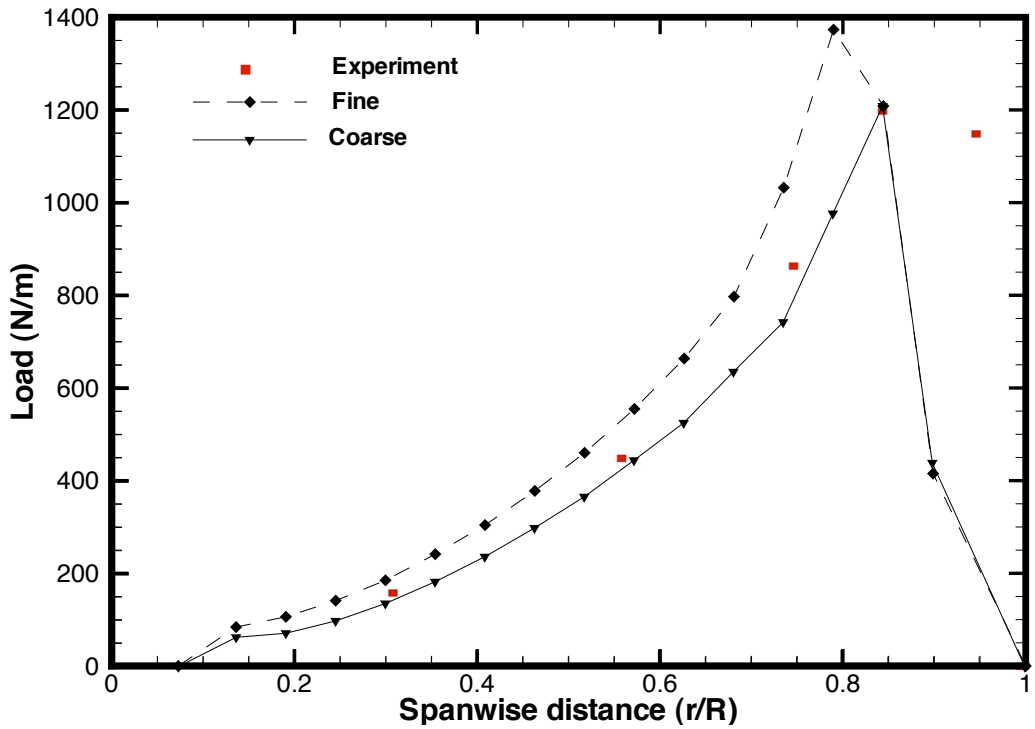

Figure 4.12: Variation of load (mean converged) per unit span along blade radius.

and coarse grid cases showed numerical instability for the tip correction function shown in equation (3.11). Therefore the tip correction function in equation (3.14) was used instead, as it resulted in a stable computation. A value of $0.8\mathcal{R}$, for the coarse as well as fine grid, is the maximum possible tip correction distance to enable stable computation. A snapshot of the induced velocity obtained using the blade loads computed using the Prandtl's tip correction while numerical instability occurred, is shown in figure 4.13(a). The Prandtl's tip loss function was evaluated

using BEMT and the function is plotted in figure 3.5. One can notice that the

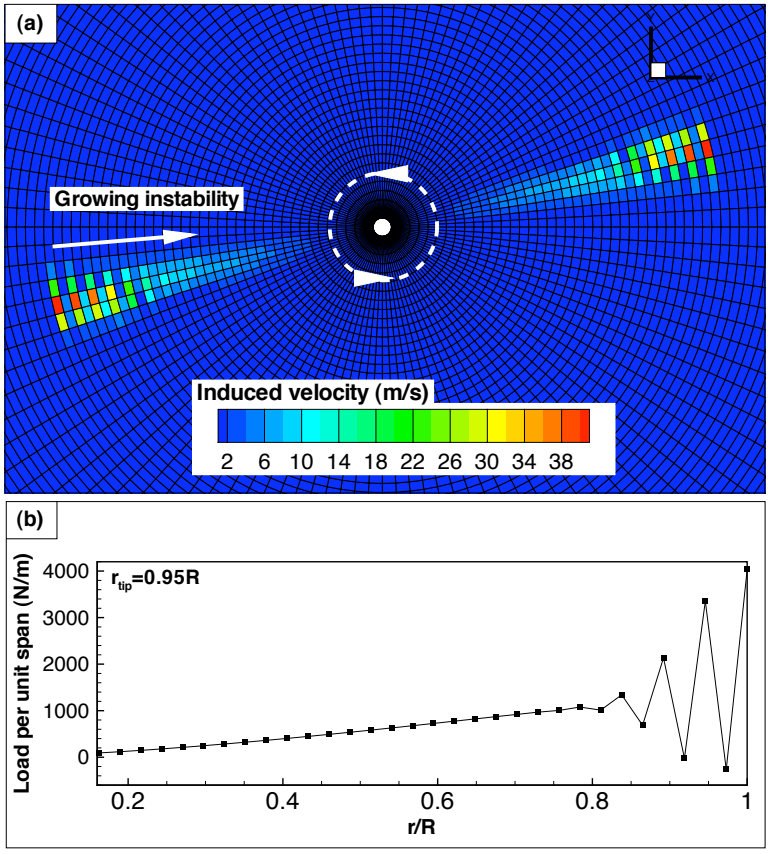

Figure 4.13: Numerical instability due to large tip correction in (a) induced velocity and (b) blade loads.

instability starts near the tip and propagates towards the center of the cylindrical grid. The blade loads obtained at the time of instability are plotted in figure 4.13(b). Usually for a two bladed rotor the load starts to fall off after $0.9 - 0.95\mathcal{R}$ as shown in figure 4.14. Therefore a large discrepancy in loads near the tip is bound to occur because a value larger than $0.8\mathcal{R}$ numerical instability similar to the Prandtl's tip loss function was observed. The reason being that there are no points available near the tip between $0.9-1.0\mathcal{R}$ to resolve the large variation in load and hence this leads to numerical instability. This problem was never anticipated in the present work where only equally spaced cylindrical grid was proposed to be used as the CFD domain. Refining the grid to meet the tip requirement yields an unrealistic runtime for an equally spaced grid. The use of a stretched grid with

more points clustered near the tip could possibly solve this issue. But this was not attempted and is left as a future improvement over the present method.

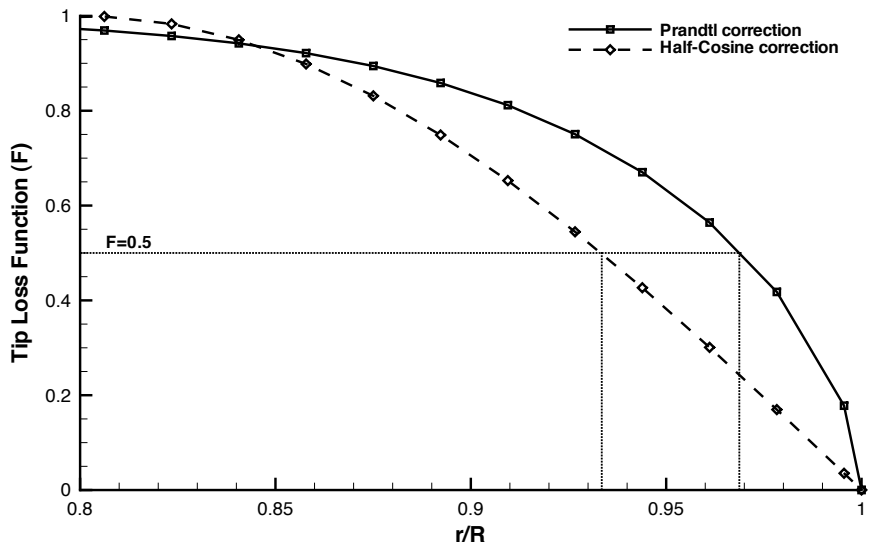

Figure 4.14: Tip correction function comparison for the two bladed isolated rotor test case - Prandtl's correction show in solid line and the Half-cosine correction shown in dotted line.

Experiment	Coarse grid	Fine grid
0.00708	0.00543648	0.00667563
% error	-23.2%	-5.7%

Table 4.3: Comparison of non-dimensional rotor thrust (C_T)

4.7.3 Qualitative flow-field validation

The flow-field results of the coarse grid obtained using the actuator model in the finite volume solver is plotted in figures 4.15 - 4.17. In figure 4.15, the vorticity magnitude in plane of the rotor is plotted along with the iso-surface of pressure. The iso-surface colored red indicates high pressure and the blue represents low pressure respectively. The results of pressure difference between the top and bottom planes of the rotor source and the presence of high vorticity near the actuator line tip are consistent with the observations of Mikkelesen[18]. The pressure difference is indeed implicitly calculated by the momentum source addition as explained

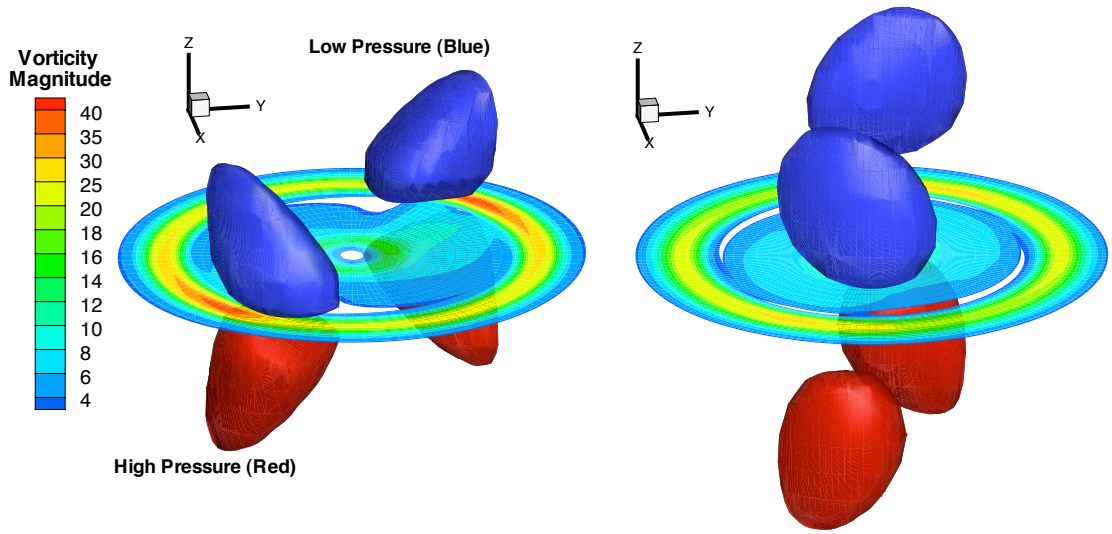

(a) Coarse grid (b) Fine grid

Figure 4.15: Vorticity magnitude at plane of rotor with iso-pressure surface indicating high and low pressure.

by Rajagopalan et al.[15]. The vorticity in-plane of the rotor shows the presence of a strong vortex near the tip of the rotor. A more detailed structure of this vortex is plotted in figure 4.16, where the iso-surface of vorticity near the rotor tip (colored by Mach number) is shown. The tip vortex is a continuous sheet instead of a distinct helical structure. This is due to the fact that the first order scheme on the coarse grids smear the vortex into a continuous sheet. Similar results of smearing of tip vortex into a continuos sheet by coarse grids was reported by Mikkelesen[18]. The wake contraction due to the acceleration of the fluid by momentum addition is rendered visible by the continuous vortex sheet. The contraction ratio (ratio between the wake radius far downstream to the rotor radius) obtained from the coarse and fine grid flow-field are compared to that of the momentum theory in table 4.4. The low order numerical scheme and coarse grid dissipates the wake

Coarse grid	Fine grid	Momentum theory
0.94	0.91	0.707

Table 4.4: Comparison of wake contraction ratio

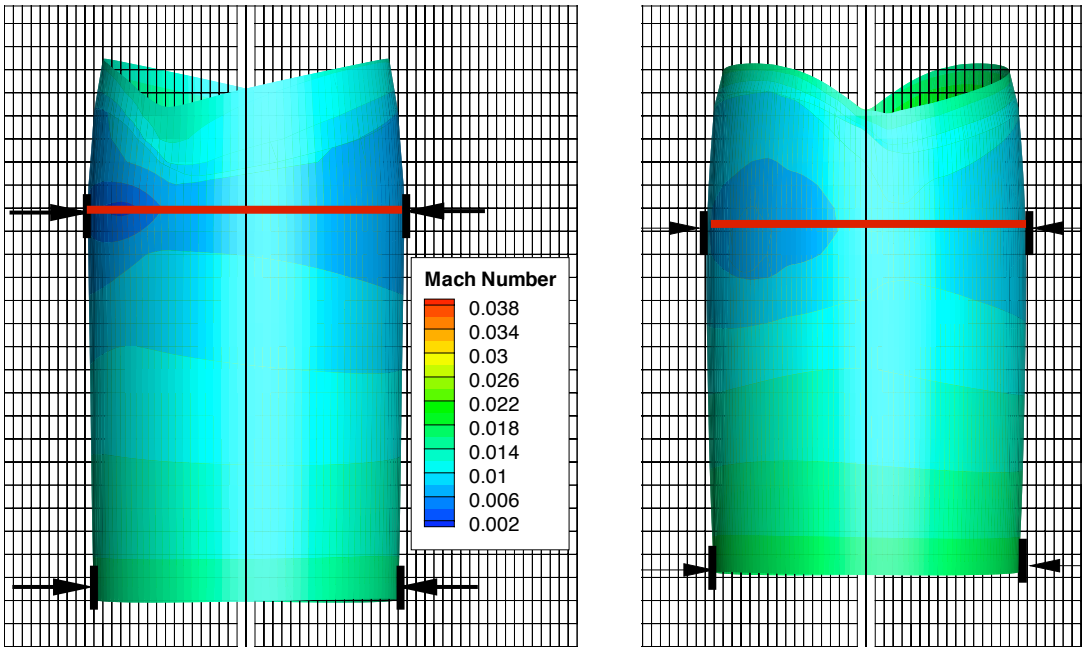

(a) Coarse grid (b) Fine grid

Figure 4.16: Iso-vorticity surface colored by Mach number (coarse grid) showing wake contraction.

considerably within 2 rotor diameters downstream, which can be observed in the velocity vector plot (colored by Mach number) in figure 4.17 on a plane cut perpendicular to the plane containing the rotor. This is main reason for the over prediction of the wake contraction ratio and the contraction not so evident in the velocity vector plots. In reference [53], an actuator disk model was used to solve the flow-field of an isolated rotor in steady climb and the wake contraction in the induced velocity contour is similarly not evident in the plots.

4.7.4 Acoustic prediction

The filtered span-wise blade load was used to perform acoustic prediction of the isolated rotor using PSU-WOPWOP as explained in chapter 2 using the compact chordwise integrated load. The loading acoustic pressure variation for two rotor revolutions as a function of observer time was calculated for a list of observers located at a distance of 10 rotor diameters at elevation angles (θ) 22.5^o, 45°, 67.5^o

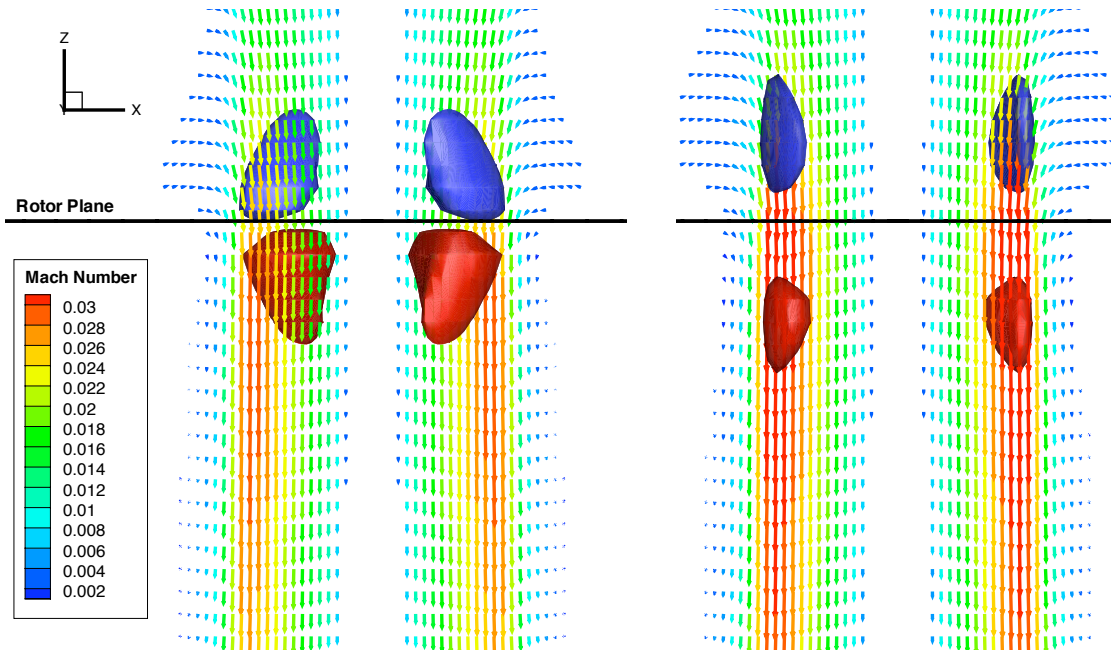

(a) Coarse grid (b) Fine grid

Figure 4.17: Induced velocity vector (colored by Mach number) due to the actuator line source.

and 90° respectively and the locations are indicated in figure 4.18. The loading acoustic pressure is plotted in figure 4.19 for the list of observers shown in figure 4.18 for both coarse and fine grid respectively. The red dotted lines are loading acoustic pressure at the Blade Passage Frequency (BPF) obtained using a narrow band filter on the noise time signal. Since the present case is an isolated rotor in hover (constant blade load w.r.t time) the entire acoustic energy ideally should be contained in the BPF and its higher harmonics. Therefore the loading noise at the BPF (red curve) is useful to qualitatively compare the amount of acoustic energy contained in the numerical oscillations compared to that at the BPF. The loading acoustic pressure of the coarse grid due to the presence of numerical noise (saw-tooth numerical wave form) shows excess acoustic energy due to numerical error over the BPF. Nevertheless, the trend of higher acoustic pressure at an angle of $45-60^o$ from the rotor and a lower acoustic pressure above and below this range is observable in the results. The loading acoustic pressure for the fine grid case is shown in figure 4.20. Here one can observe that the acoustic pressure amplitude

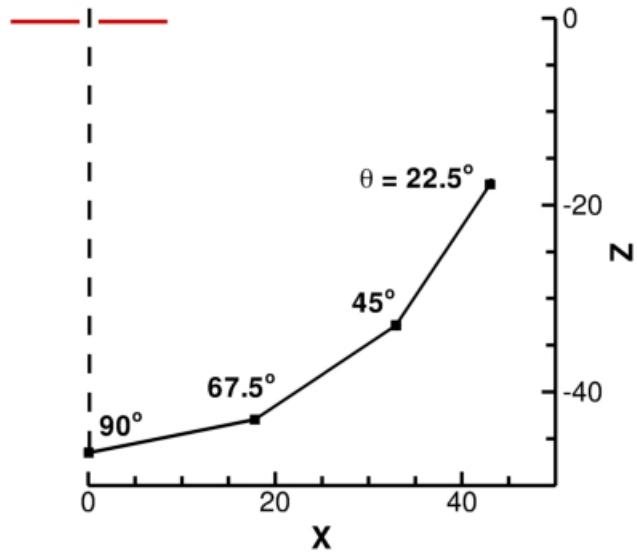

Figure 4.18: Observer location to measure loading acoustic pressure along the elevation angle θ (actuator line location shown in red solid line).

closely follows that of the BPF and only a fractional change is observable due to the error oscillations compared to the coarse grid case. Ideally, exactly underneath the rotor ($\theta = 90^0$ in figures 4.19 and 4.20), the acoustic pressure should be zero. Due to the low frequency periodic error occurring every 60° and 90° along the azimuth one gets 12 and 8 peaks in the signal for the fine grid and coarse grid respectively. The acoustic pressure at the BPF for the fine grid at $\theta = 90^o$ is zero indicating that there are no error sources at the BPF.

The Overall Sound Pressure Level (OASPL) of the fine and coarse grid for a spherical observer grid of 10 rotor diameters (10D) shown in figure 4.21 are plotted in figure 4.22. The grid is generated with a resolution of 9^0 in both the azimuth and elevation direction and the location of the actuator line in the grid is indicated in the figure in red solid line. The trend in the OASPL of the fine grid agree with the general trend in loading noise as the maximum level fall at about $45 - 60^0$ and a minimum level underneath and in-plane the rotor. Due to the presence of large errors in the load time history of the coarse grid the OASPL levels directly below the rotor are very high compared to the fine grid. The general noise levels of the coarse grid are high due to the presence of large numerical error. The OASPL contour in the fine grid show the right trend for an isolated rotor case where the

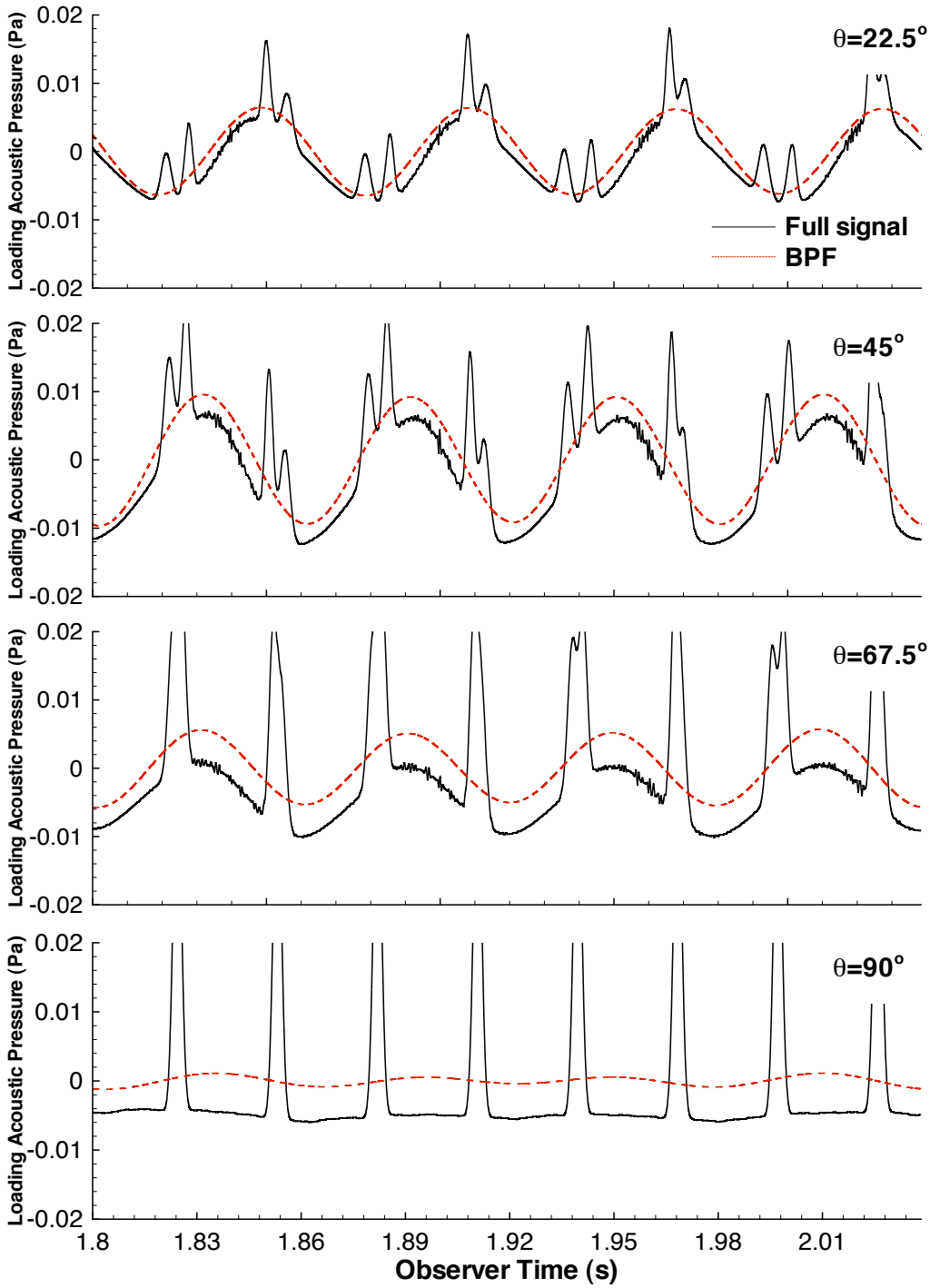

Figure 4.19: Loading acoustic pressure as a function of time at observer located at 10D distance at indicated elevation angle θ from the plane containing the rotor for the coarse grid. The black lines indicate the full loading noise signal and the dotted red line indicate the loading pressure at the BPF.

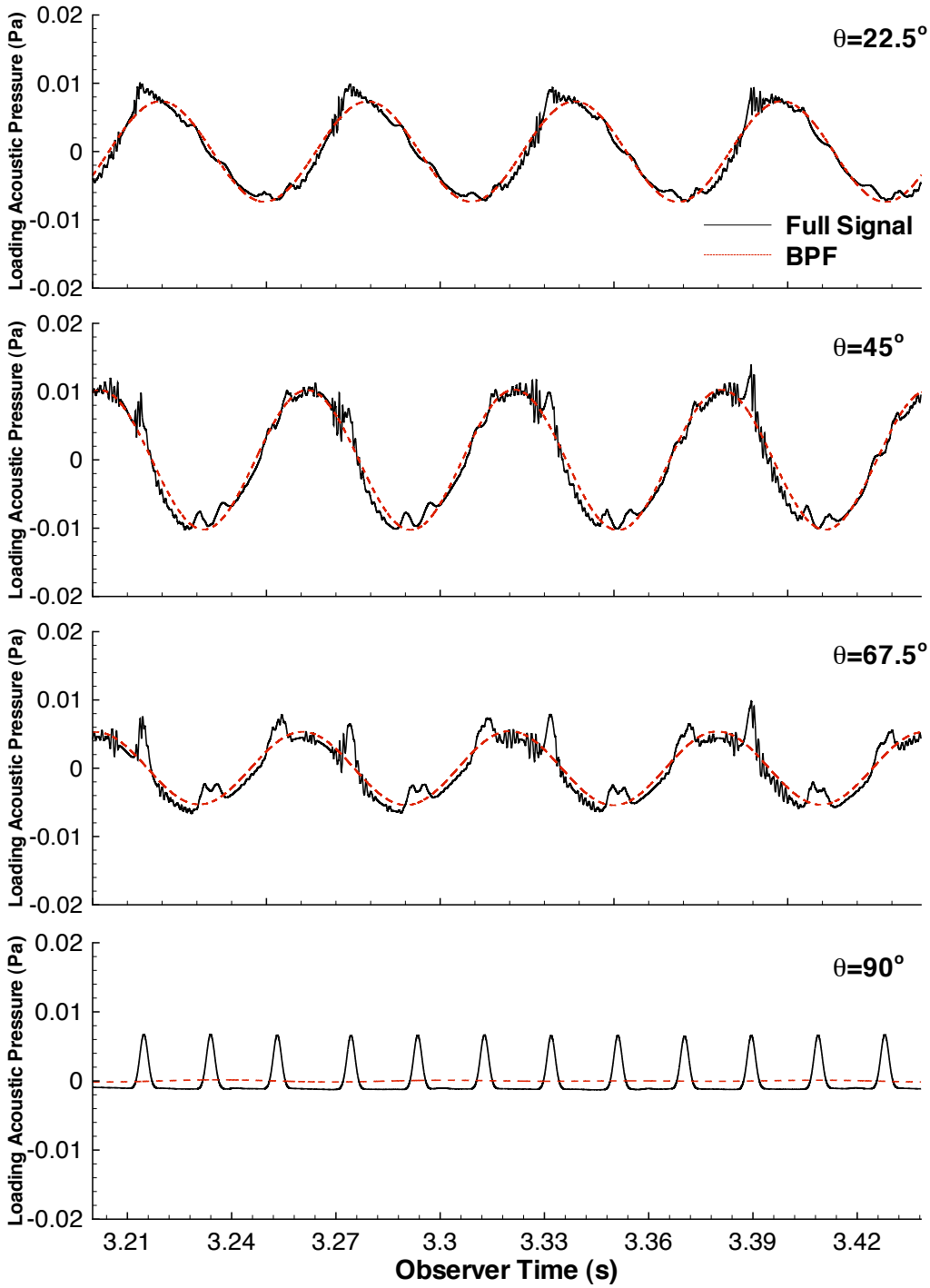

Figure 4.20: Loading acoustic pressure as a function of time at observer located at 10D distance at indicated elevation angle θ from the plane containing the rotor for the fine grid. The black lines indicate the full loading noise signal and the dotted red line indicate the loading pressure at the BPF.

noise is isotropic for a stationary observer.

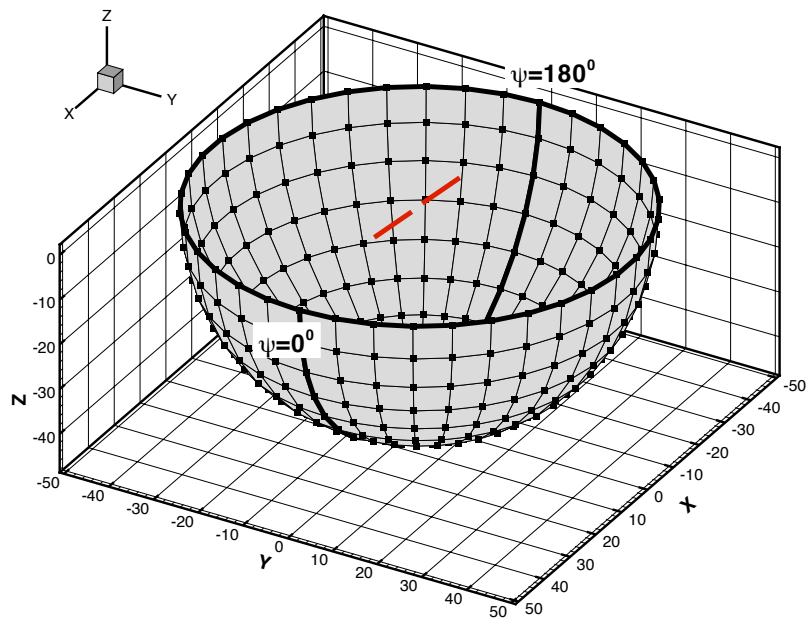

Figure 4.21: Spherical observer grid used for OASPL calculation.

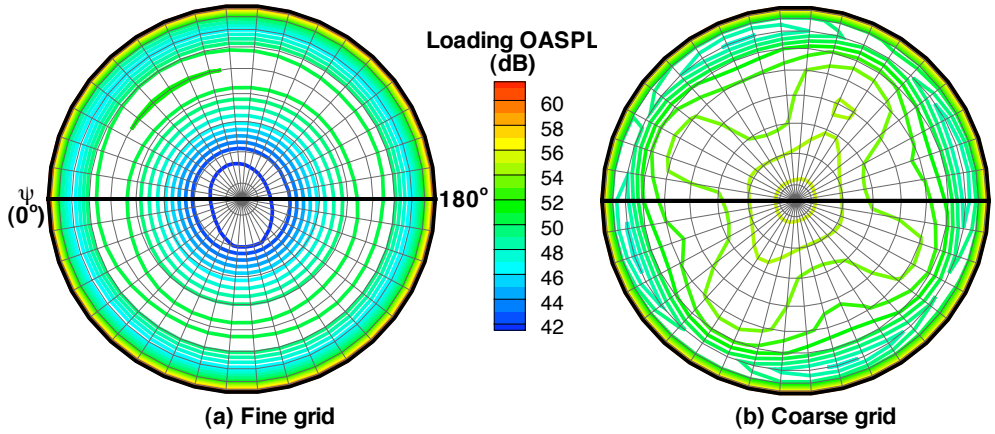

Figure 4.22: Overall Sound Pressure Level (OASPL) contour of loading noise obtained from (a) fine grid and (b) coarse grid for the spherical observer grid of radius 10D.

Chapter 5

Actuator model in IBSEN

As mentioned in the introduction to the thesis, the present work is a part of a new multi-tiered suite of tools capable of predicting rotorcraft noise at various levels of fidelity depending on the required accuracy and computational time constraints. The actuator line source method explained in chapters 3 and 4 will be used as a low accuracy model (low on computational time) in the suite of tools. The tool used for unsteady flow field prediction in the multi-tiered suite is called the Immersed Boundary Solver for Environment Noise (IBSEN) developed by Hennes[54]. It is stated in reference [54] that, *"IBSEN is a flow solver that can be set up quickly to run a variety of geometries, as might be used during the design of a new rotorcraft, so a compressible, inviscid flow solver based on the Immersed Boundary (IB) method was chosen. In this technique the rotor surface geometry is immersed within a structured, Cartesian grid (i.e., the surface of the rotor blade moves within the Cartesian volume grid, but the volume grid does not conform to the surface - it actually passes through the surface). The major aerodynamic effects of the blade are captured while dramatically reducing the time and effort necessary to generate the rotor grid (as compared to a body-fitted OVERFLOW-type grid, for example), and preserving the simple parallelization and load-balancing of a structured, overset grid system. In addition, the flow solver design is heavily influenced by the main project goal of using the solver to quickly predict the noise generated by complex configurations. This influence is reflected in the name of the new solver: Immersed Boundary Solver for Environment Noise (IBSEN)."*

The Unstructured Finite Volume Domain with the Actuator Line Model (UFVD-

ALM) for the rotor is integrated with IBSEN using the overset strategy. Therefore, the complex flow field calculations near the rotor is simplified using the actuator line model. At the same time, the unsteady flow field over fuselage and other appendages can be captured using the immersed boundary condition of the Cartesian grid solver in IBSEN. The interference effect of the fuselage and other appendages on the rotor flow field is passed using the overset boundary. The unsteady rotor loads predicted using UFVD-ALM thus includes the interference effects due to fuselage. The acoustics prediction is performed, as explained in chapter 2, using the chordwise compact loading obtained from the UFVD-ALM. Figure 5.1 shows a setup, which makes use of IBSEN (with UFVD-ALM) to solve the flow field of a generic helicopter configuration. The UFVD-ALM, is confined to a small portion near the rotor while the rest of the domain is the IBSEN Cartesian grid. At the overset interface of the two domains the data from UFVD-ALM is transferred to the Cartesian domain and vice versa using interpolation.

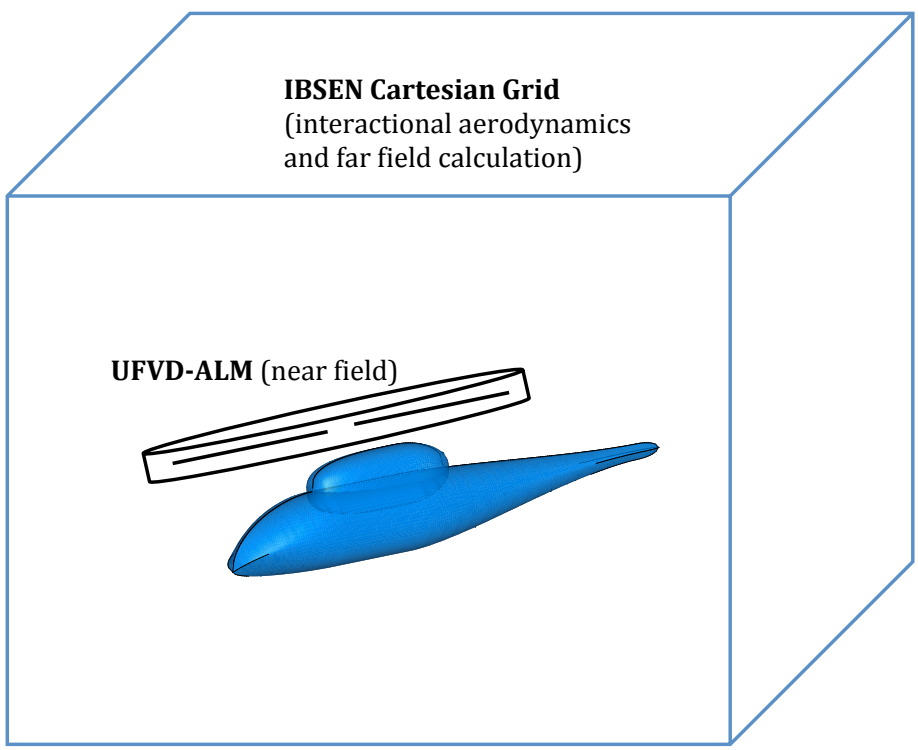

Figure 5.1: Overset grid setup for a helicopter configuration with UFVD-ALM for the rotor near field and IBSEN Cartesian grid for the far field calculation.

The details of the overset strategy and immersed boundary condition implementation in the IBSEN Cartesian grid solver is provided in reference [54]. In this chapter, the strategy adopted to overset the UFVD-ALM with IBSEN and results for a standard test case of isolated rotor in hover, are presented.

5.1 Overset grid method

At the overset boundary of the two domains, namely, the UFVD-AL and IBSEN Cartesian grid, flow field values are interpolated from one grid (donor) to another (acceptor). Interpolation operation yields only an approximate value at the acceptor point and error is controlled by the type of interpolation employed. As a result the interpolation yields numerical sources at the overset boundary and its accumulation can lead to numerical instability. Since the solution methodology in the two overset domains are different, the error propagation becomes highly complex and standard methods fail to predict numerical stability. The UFVD-ALM grids are obtained from a structured cylindrical grid and hence are anisotropic (finer near the center and coarser away) compared to the background grid which is Cartesian. The trilinear interpolation in IBSEN was not tested for coupling arbitrary shaped grids and extending them, hence for the present work, this approach requires testing. In addition, Sengupta et al.[55] have reported success using least squares method for interpolation for an overset domain with polar grids. The authors conducted Direct Numerical Simulation (DNS) of unsteady bluff body flows and reported that the least squares interpolation resulted in a stable computation. The least squares and trilinear interpolation were compare using a standard test case in the present work. The method with the best error characteristics was subsequently implemented as the overset boundary interpolation method to pass values from the cylindrical UFVD-ALM grid to the Cartesian grid. The interpolation is implemented only for the overset boundary points of the IBSEN Cartesian grid requiring flow field values from the neighboring UFVD-ALM and for all other overset boundaries the trilinear interpolation already implemented in IBSEN by Hennes[54] was used. Details of the derivation and numerical implementation of the least squares interpolation used in the present work is available in Appendix B, which is based on the work in reference [55].

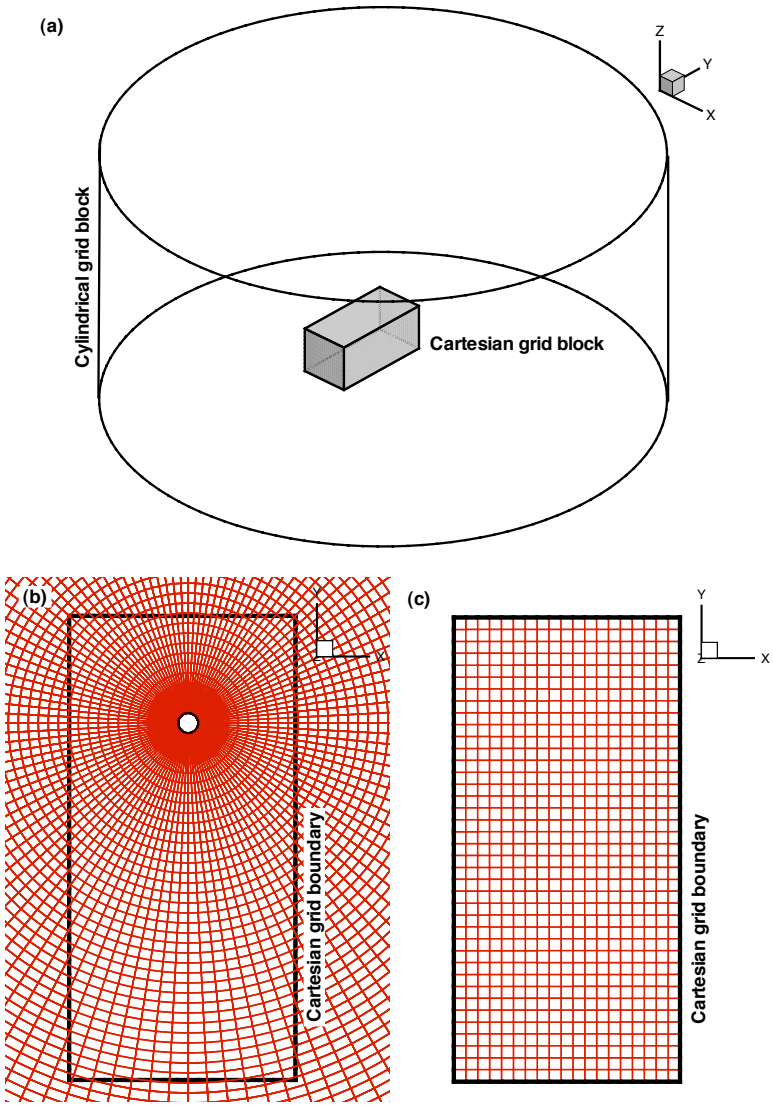

Figure 5.2: (a) Cylindrical and Cartesian grid blocks used for testing least squares interpolation, (b) Top view of cylindrical grid with the Cartesian grid boundary and (c) Cartesian grid top view.

The least squares method was tested using a smooth 3D Gaussian function, shown in equation (5.1), before implementing it in the UFVD-ALM solver.

$$\mathcal{F} = A \exp\left\{ -\frac{[(x-x_0)^2 + (y-y_0)^2 + (z-z_0)^2]}{B} \right\} \tag{5.1}$$

with, $A = 2.0$, $B = 0.05$ and $(x_0, y_0, z_0) = (-0.5, 0, -1.5)$. A cylindrical and a

Cartesian grid were used for testing the interpolation and the grid blocks are shown in figure 5.2(a). The origin $(0, 0, 0)$ corresponds to the center of the cylindrical grid's bottom most plane and the cylindrical grid's radius and height is 5 units. The Cartesian region is a cuboid with dimensions $1 \times 2 \times 1$ units with the centroid of the Cartesian grid offset (x_0, y_0, z_0) from the origin. The top view of the grid generated over the individual blocks is shown in figures 5.2(b) and (c). The test function ($\mathcal{F}$) was specified at the cell centers of the cylindrical grid and the values were interpolated to the Cartesian grid nodes. The relative error, e_r, (equation (5.2)) for the test problem is plotted in figure 5.3(a) and (b) for both least square and trilinear interpolation, at a plane containing the maximum relative error for the least squares interpolation. For the same order of approximation and same set of neighboring interpolants, the least squares interpolation was found to have lower error than trilinear interpolation for a smooth function (cylindrical grid (donor) to Cartesian grid(acceptor)).

$$e_r = \frac{\mathcal{F}_{interpolated} - \mathcal{F}_{exact}}{\mathcal{F}_{exact}} \ \% \tag{5.2}$$

In the original IBSEN code the acoustic prediction is preformed using a permeable surface over which the flow field values are know for all times (from CFD). The far-field acoustic pressure is calculated using the FW-H acoustic analogy with the given input data viz., flow field values at the permeable surface. But in the present case such an acoustic prediction is not meaningful since the blades are modeled and only a gross unsteady flow field near the rotor is available. Therefore, the permeable surface is not employed in IBSEN with the UFVD-ALM, instead, the compact chordwise loads obtained from the UFVD-ALM is used to perform the acoustic prediction. The UFVD-ALM along with the overset boundary interpolation using least squares method and the compact chorwise load input routine for acoustic prediction was added as a new solver module in IBSEN. Figure 5.4 illustrates the overall block diagram of the modified IBSEN code.

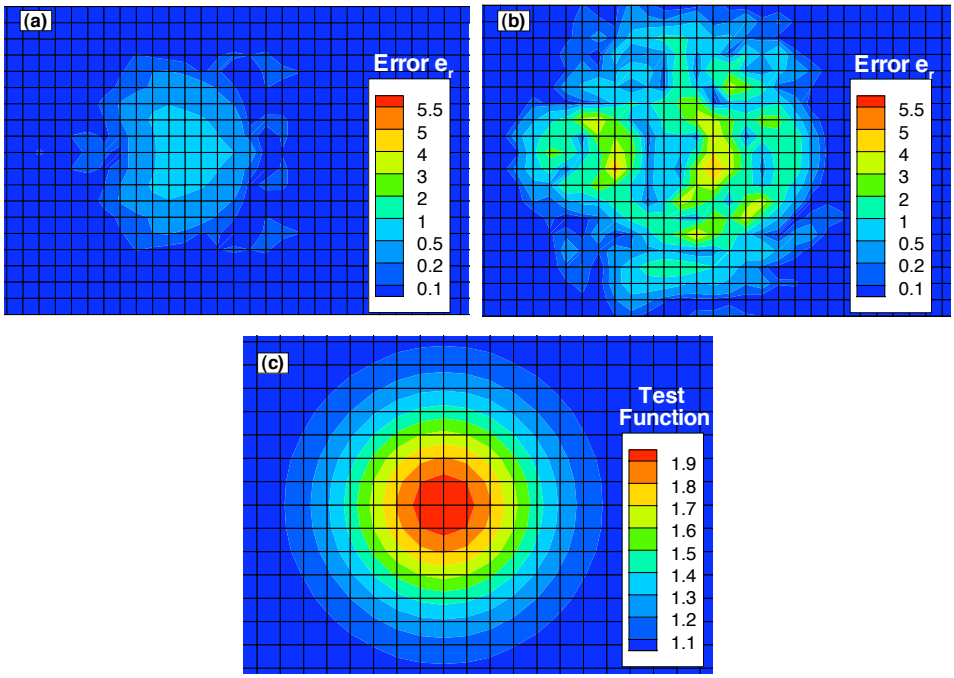

Figure 5.3: Percentage relative error e_r for (a) Least squares interpolation and (b) Trilinear interpolation. (c) The exact test function ($\mathcal{F}$) plotted at the same cut plane as (a) and (b).

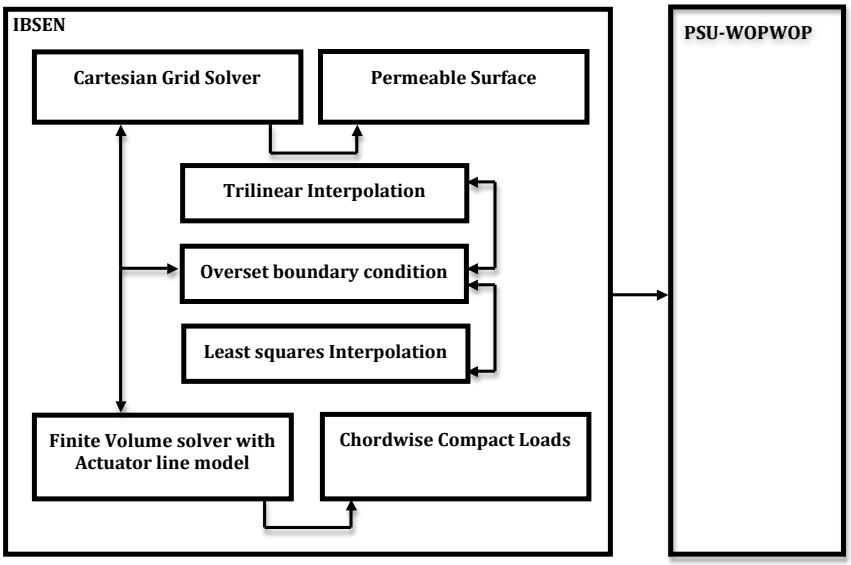

Figure 5.4: IBSEN block diagram - overview of UFVD-ALM solver implementation.

5.2 Results

The UFVS-ALM solver overset with IBSEN was used to solve the test problems from reference [49] described in detail in section 4.7 of chapter 4. The side and top view of the overset grid domain used in the present calculation are shown in figure 5.5(a) and (b), respectively. The inner-most block in the overset setup is the finite volume grid containing the actuator sources (shown in red solid line). The overset Cartesian grid blocks occupies the rest of the domain and were generated using IBSEN's built-in off-body grid generator[54]. The grid density of each inner grid level of the Cartesian overset blocks differers from its outer grid level by a factor of 2. There are 3 such overset levels of Cartesian blocks in the present case. The grid belonging to the first level of the overset Cartesian blocks and that of the finite volume domain are shown in figure 5.6. The thick-green-solid lines demarcate the finite volume grid and the IBSEN Cartesian grid and the region in-between the demarcation is the overlap grid region. The actuator line is placed in the cylindrical grid domain such that it does not fall inside the overlap region. The least squares interpolation described previously is used to interpolate flow values from cylindrical grid to the Cartesian grid in this region. A third order finite difference upwind scheme with Lax-Freidrich flux splitting and first order finite volume scheme with Roe approximate Riemann solver as described in chapter 4 were employed in the Cartesian and finite volume region respectively. The different input and grid parameters used are tabulated in table 5.1. The blade loads and flow field obtained from the simulation are presented in the subsections to follow.

Grid		Input	
dr	$0.0641m$	σ_ξ	$2c$
$d\theta$	1.5^o	σ_η	c
Total Nodes	$1.5e6$	Total processors	8
Actuator domain extent	$1.2D$ by $0.3D$		
IBSEN domain extent	$5D$ by $5D$ by $5D$		

Table 5.1: Values of grid and input parameters used in the CFD simulations

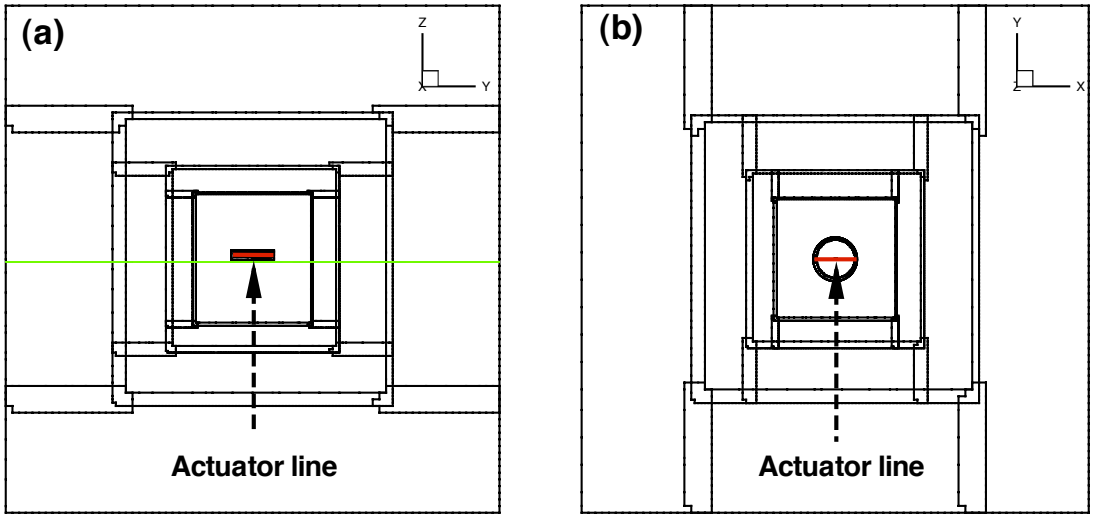

Figure 5.5: Edges of the overlap grid domain shown by solid lines (actuator source shown in red solid line).

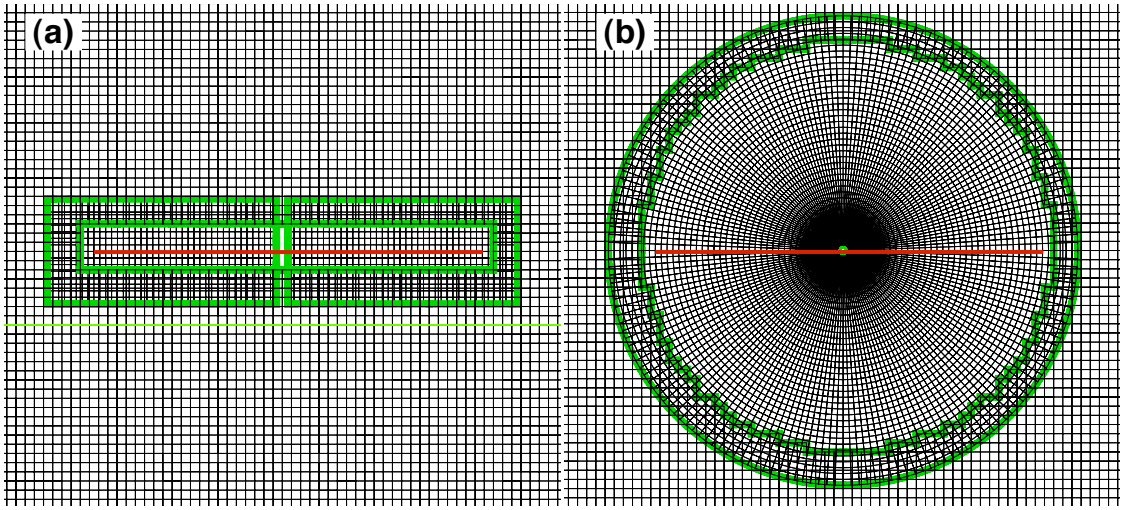

Figure 5.6: Overlap grid, (a) side view and (b) top view, between UFVS-ALM and IBSEN (inner-most grid) - actuator source shown in red solid line.

5.2.1 Blade load convergence

Shown in figure 5.7 is the convergence history of load per unit span at a radial location corresponding to the maximum spanwise value. The results look similar to that of the standalone finite volume solver with (i) the rapidly varying saw-tooth

wave form at every azimuthal division 1.5^o and (ii) the slowly varying component, which is no longer a regular saw-tooh wave form but some arbitrary periodic wave as shown in figure 5.7. In addition the loads converge much faster (at about 0.65s) compared to the coarse grid (1.25s) presented in the previous chapter and the oscillations also occur between a smaller bandwidth compared to the coarse but higher compared to the fine grid standalone case. The effect of overset boundary is quite obvious from these results because the grid used in the overset case are much more refined compared to the fine grid case of the standalone solver. Ideally they should yield much better load prediction but the filtered loading history in figure 5.8 shows the presence of significant numerical oscillations which are neither removed by filtering or by refinement of grid. Therefore, the overset strategy adopted becomes quite critical for obtaining error free solution.

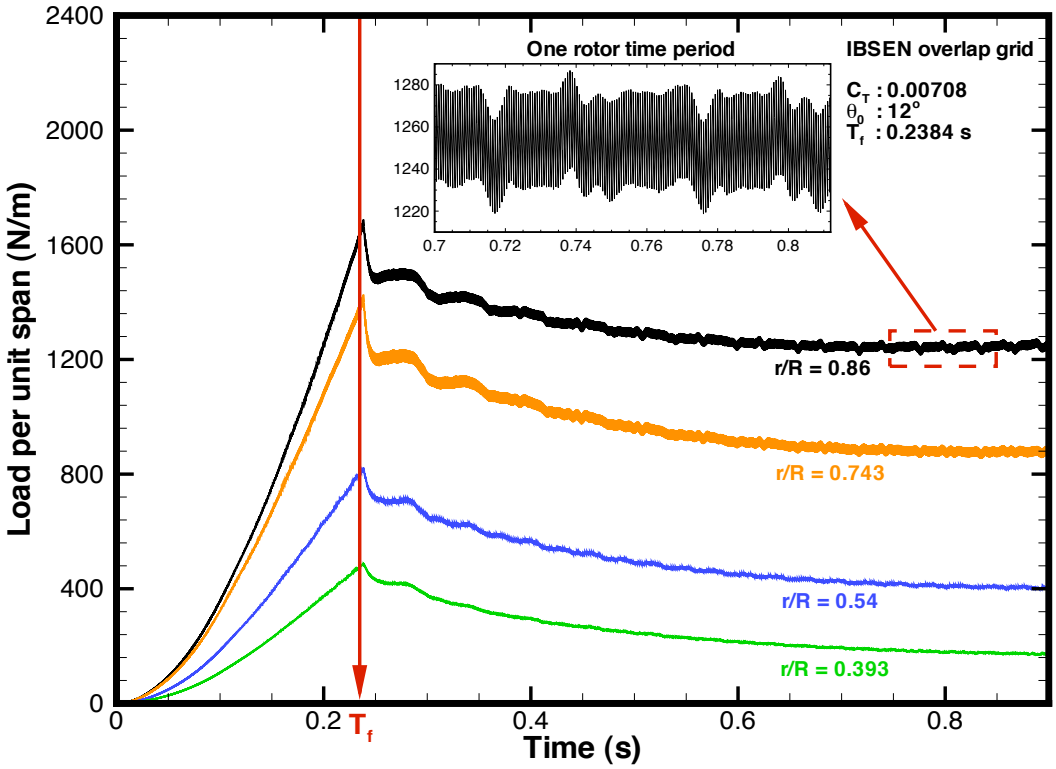

Figure 5.7: Blade load convergence history (IBSEN overlap grid) at the indicated spanwise locations.

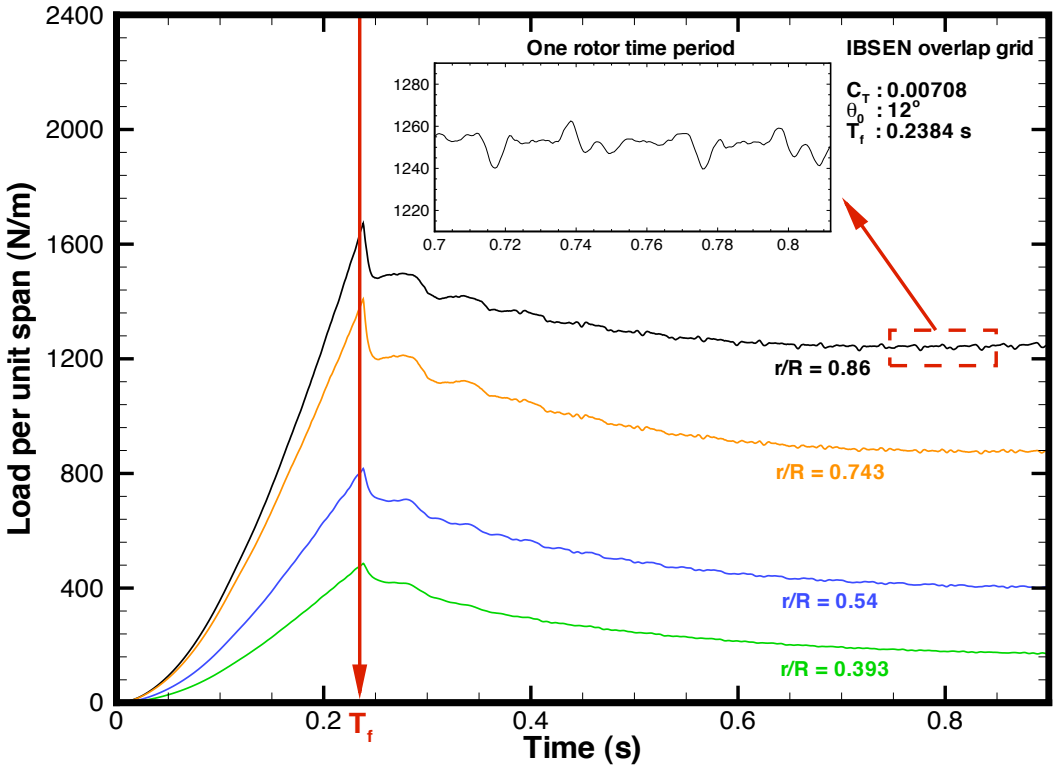

Figure 5.8: Filtered blade load convergence history (IBSEN overlap grid) at the indicated spanwise locations.

5.2.2 Blade load validation

The blade loads obtained using the UFVS-ALM and IBSEN overset solver is validated against the experimentally obtained values in reference [49]. The variation of load per unit span for the mean converged load is plotted along the blade radius in figure 5.9 along with the experimental values. The loads converge much faster in the overset grid case compared to the standalone finite volume grid cases. The primary reason is that unlike the grids used in the standalone solver case, the overset grid are fine only near the rotor and become coarser as one moves away. Therefore, the convergence is more rapid in this case as the errors are effectively damped by the coarse background grids at the same time the flow is correctly resolved by the near field cylindrical grid. The spanwise loads are slightly over-predicted and the overset boundary is suspected to be the primary cause because conservation of flow variables is not fully ensured at the interpolation boundary. A higher order

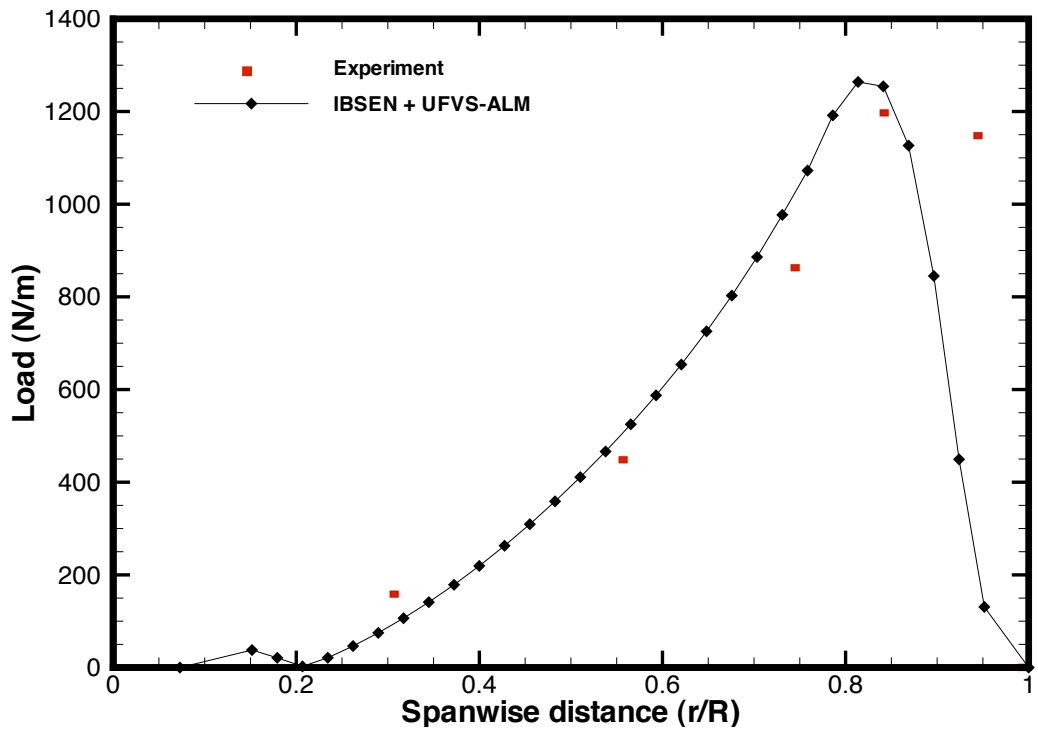

Figure 5.9: Variation of load (mean converged) per unit span along blade radius.

interpolation may yield better conservation properties but in reference [55] it was pointed out that a higher order does not necessarily ensure better accuracy. Thus, the problem dictates further investigation which is beyond the scope of the present work. The numerical issue with the tip correction, similar to the standalone finite volume solver, existed in the present case. Nevertheless, due to the increased number of points along the blade span, it was possible to push the tip correction length value to $0.83\mathcal{R}$ and any value beyond showed numerical instability. This is a good indication that the radial spacing is a key factor in determining the tip numerical instability. The loss of thrust due to the tip correction is tabulated in table 5.2.

Experiment	IBSEN result
0.00708	0.00604178
% error	-14.6%

Table 5.2: Comparison of non-dimensional rotor thrust (C_T) - IBSEN result

5.2.3 Qualitative flow field validation

The flow field obtained using the overset UFVS-ALM IBSEN solver is plotted in figures 5.10 - 5.12. The vorticity magnitude in plane of the rotor, plotted in figure 5.10, is higher compared to the finite volume cases because the finer grid density used to solve the flow field resolves the vorticity more accurately. The third order finite difference scheme used in the Cartesian grids results in lower numerical dissipation. The pressure difference between the top and bottom surface

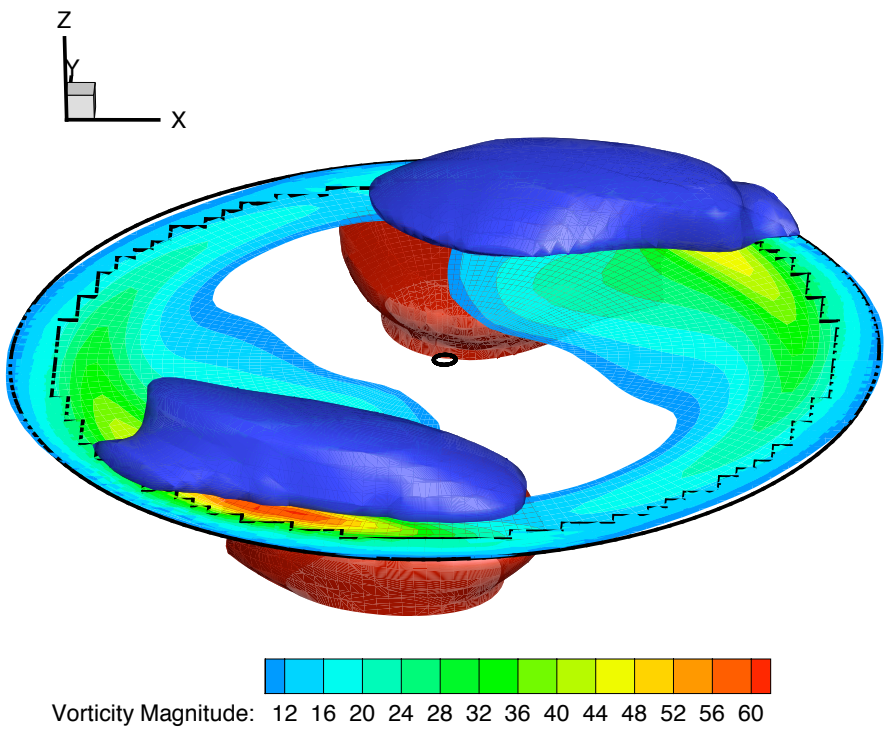

Figure 5.10: Vorticity magnitude at plane of rotor with iso-pressure surface indicating high (red) and low pressure (blue) obtained using IBSEN UFVS-ALM.

of the actuator source resulting from added momentum is indicated by the high (red) and low (blue) pressure iso-surface of pressure in figures 5.10 and 5.11. In figure 5.11, the velocity vectors colored by Mach number are drawn to the same scale as that of the stand alone finite volume solver results plotted figure 4.17. The induced velocity field of the overset and stand alone cases agree well up to a few rotor radius downstream, but the wake undergoes lesser dissipation in the overset grid case. Since the simulation was performed only for 10 revolutions of

the rotor the wake had developed only for few rotor diameters downstream. The

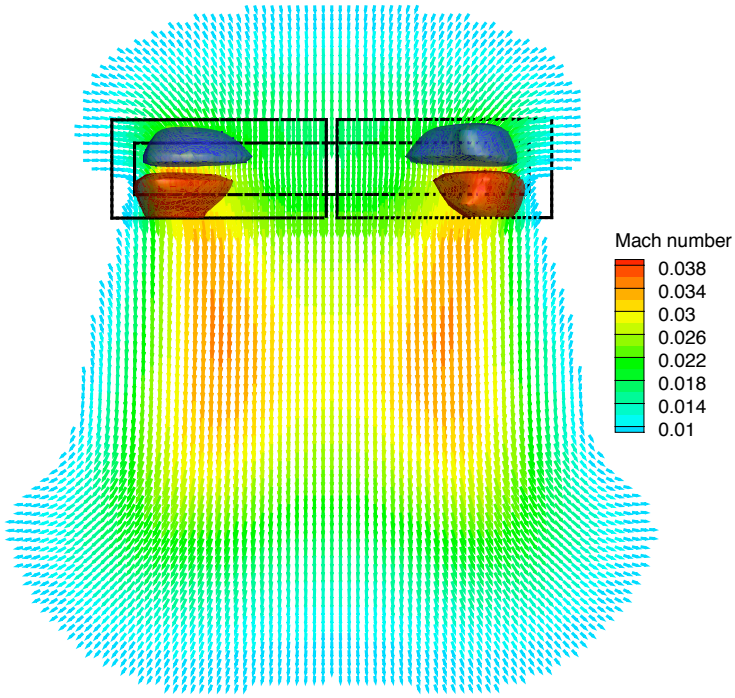

Figure 5.11: Velocity vector colored by Mach number at a plane normal to the rotor plane with iso-pressure surface indicating high (red) and low pressure (blue) - obtained using IBSEN UFVS-ALM (levels below 0.01 is cut-off).

wake contraction is clearly evident in both the velocity vector plot and iso-vorticity plot in figures 5.11 and 5.12 respectively. The wake contration ratio of the IBSEN case is tabulated along with the ideal contraction ratio predicted by momentum theory in table 5.3. The overset interpolation smears the tip vortex generated by the momentum source addition resulting in vorticity to be smeared at grid points on the top surface of the rotor plane. The strong ring vortex is a reminiscent of the startup transients (ramp start). This starting vortex forms initially when the sources are introduced and dissipates as it convects downstream w.r.t time. The overall flow field results of the overset UFVS-ALM in IBSEN solver appears much more physical than the standalone finite volume solver due to the following reasons. The wake developed downstream of the rotor shows better contraction compared to the finite volume case. In addition, the wake is preserved longer downstream of the rotor. The primary reason is the third order finite difference scheme used

to solve the flow field in the outer Cartesian grid. This resolves the flow features much better than the first order finite volume scheme. Since IBSEN was geared towards aeroacoustic predictions, equally spaced grids were employed because they possess good propagation characteristics, i.e., have minimal numerical dissipation and dispersion. Thus the solution is improved further by the equally spaced grids.

Momentum theory	IBSEN result
0.707	0.785

Table 5.3: Wake contraction ratio predicted by momentum theory and IBSEN

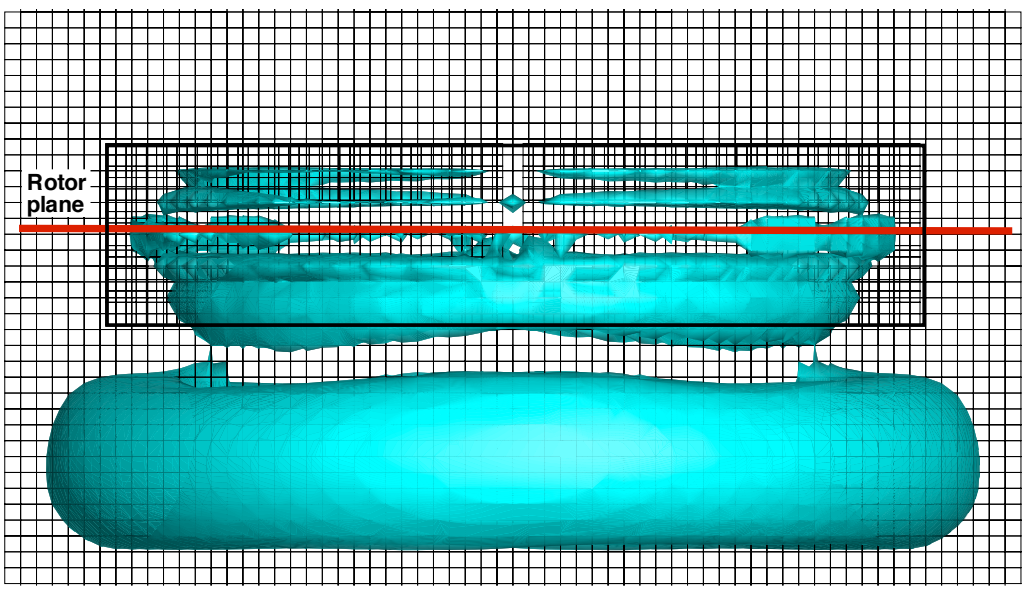

Figure 5.12: Iso-vorticity surface of the rotor wake obtained using IBSEN UFVS-ALM (overlap grid plotted).

5.2.4 Acoustic prediction

The loading acoustic pressure obtained using the filtered load and narrow-band BPF (red dotted lines) are shown in figure 5.13 at the observer locations indicated in figure 4.18. The numerical noise due to oscillations in the blade loads dominates the complete acoustic spectrum. The loading acoustic pressure at the BPF is quite

small compared to the loading pressure due to the numerical noise. Although the numerical error oscillates only within 3.5% of the mean converged load, the time rate of change of the loads are quite high because the oscillatory error in loading occurs at a higher frequency compared to the standalone cases where the oscillations predominantly occurred at low frequencies. This can be explained using equation (5.3) where the time derivative of a function $f(t)$ is performed in the Fourier space ($F(\omega)$ denotes the Fourier transform of $f(t)$).

$$f'(t) = \int \omega F(\omega) d\omega \tag{5.3}$$

Therefore, for the same amplitude of $|F(\omega)|$ a large ω would yield a higher value for the time derivative compared to a smaller value of ω.

The Overall Sound Pressure Level (OASPL) of the UFVS-ALM results for a spherical observer grid of 10 rotor diameters (figure 4.21) are plotted in figure 5.14. Similar to the coarse grid results of the standalone solver the UFVS-ALM results suffer from large errors in the load time history. The OASPL is fairly constant for $\theta = 90 - 30^o$ with variation of only few dB because the numerical noise dominates the OASPL more than the loading acoustic pressure at the BPF. The results clearly indicate that the presence of even a small error in loading can have a significant impact on the loading noise. The results obtained are a preliminary study to demonstrate the successful coupling of the actuator line model in the IBSEN flow solver and its suitability for design acoustic calculations. There are a few important issues which require further investigation to enable reliable estimation of loading acoustic pressure using the present method and are discussed in the next chapter.

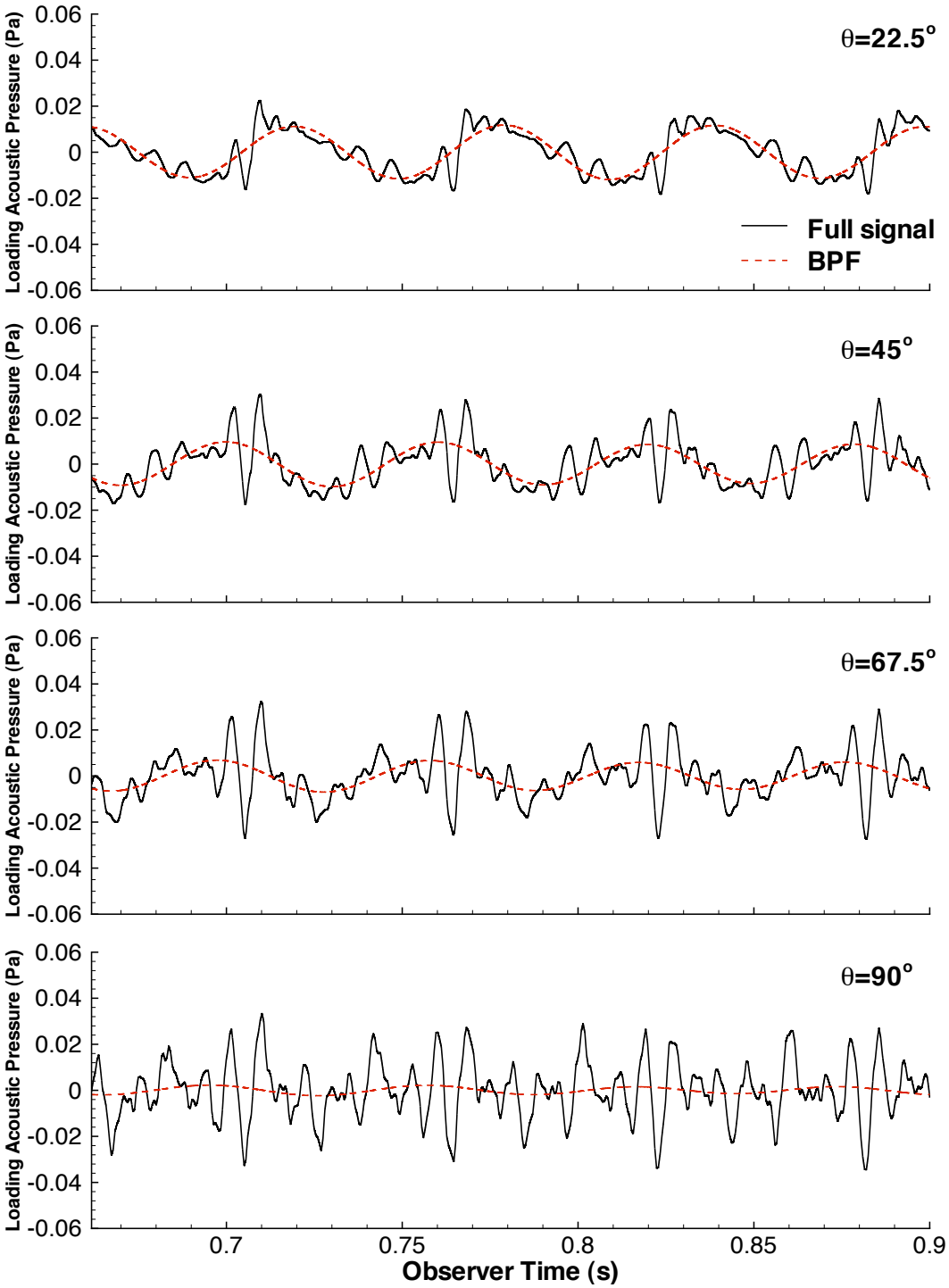

Figure 5.13: Loading acoustic pressure as a function of time at observer located at 10D distance at indicated elevation angle θ from the plane containing the rotor for the IBSEN overset grid.

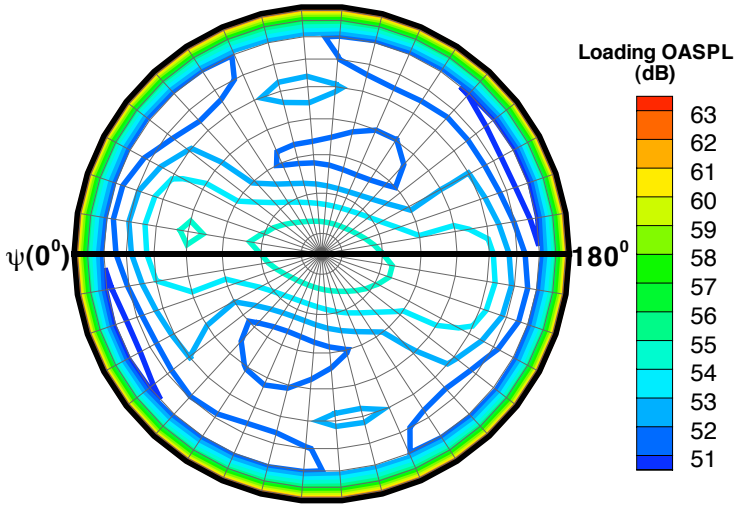

Figure 5.14: Overall Sound Pressure Level (OASPL) contour of loading noise obtained from UFVS-ALM at a distance of 10D.

Chapter 6

Summary and Future Work

A summary of the complete actuator line method to predict loading noise from rotorcraft is first presented. Following this, the limitations of the method and future direction for continued research towards improving the method are suggested.

6.1 Summary

The present work aims at adding a new layer of fidelity into a multi-tiered suite of tools for rotorcraft design and acoustic predictions. The tool is constrained with the following requirement viz., (a) unsteady information about the flow field be preserved for acoustics, (b) computational speed should enable design calculations, (c) numerical errors in data be minimized and made fit for acoustic prediction and (d) the unsteady interactional flow field should be captured to facilitate interactional noise predictions.

Towards achieving the above mentioned goals an unsteady actuator line model (ALM) to model the blades of a rotor as equivalent sources in the governing fluid dynamic equations was derived. The model uses the unsteady flow field obtained for an initial guess value for the blade loads/sources using CFD and iteratively corrects the loads/sources using BET to converge to a given trim state. The ALM was numerically implemented in a first order finite volume scheme with Roe's approximate Riemann solver in an unstructured grid formulation. The grids were generated from structured equally spaced cylindrical grid with the centerline cells merged into a single polyhedral cell to minimize numerical errors. The numeri-

cal implementation of the ALM and finite volume solver is discussed in detail in chapters 3 and 4 respectively. The key features in the numerical implementation of ALM are, (a) regularization of singular source terms using Gaussian kernel with prescribed standard deviation, (b) volume integration of the blade source terms to obtain the cell average source value, (c) azimuthal interpolation of induced velocity from the CFD domain on to the actuator line and (c) recalculation of blade loads using BET and interpolated induced velocity predicted by CFD in a previous time step in an explicit fashion. The coupled unsteady ALM-finite volume CFD solver has been validated and the blade loads are found to converge to the correct state with the predicted blade loads in good agreement with the experimental results. Due to the coarse nature of the grids employed for the calculations the unsteady flow field is not adequately captured to long distance downstream of the rotor. Nevertheless important features like wake contraction, fluid acceleration downstream of the rotor and pressure difference across the rotor plane are observed while the exact values are not close to typically obtained ones. The flow field results of the standalone finite volume solver is understandable since emphasis was laid on robustness and stability rather than high accuracy and resolution.

Interactional noise prediction requires an accurate method to obtain the unsteady flow field, which is difficult to obtain using the present finite volume method as a high grid density is required. In addition the equally spaced cylindrical mesh further increases the cell count requirement. The strategy adopted to overcome this constraint was by adding the present UFVS-ALM into the overset CFD solver IBSEN. IBSEN was designed to perform aeroacoustic computation for full rotorcraft configurations, therefore, it has good dispersion and dissipation characteristics and higher accuracy compared to the first order finite volume scheme of UFVS-ALM. The overset strategy can be utilized to increase grid density only at key locations in the domain thus saving on computational time. Therefore, the UFVS-ALM is used to only model the rotor and the immediate vicinity and IBSEN's Cartesian grid solver is used in all other portion of the domain to solve the flow field. The immersed-boundary condition in IBSEN can be used to simulate the unsteady flow over a fuselage and other appendages and the interaction due to the presence of the solid boundary is passed to the UFVS-ALM using the overset boundary. The flow field results of the isolated rotor obtained using the overset combined UFVS-ALM

in IBSEN shown in chapter 5 are more realistic compared to the results of the standalone finite volume solver. The wake contraction ratio predicted is close to the theoretical estimate and the unsteady wake is preserved faithfully downstream of the rotor. The span-wise blade loads predicted are also close to the experimental values except near the tip of the blade. Thus in the presence of fuselage or other appendages, the UFVS-ALM containing the blade sources would have the interaction information of the solid boundaries, placed in the IBSEN Cartesian grid, in the unsteady blade loads obtained.

6.2 Limitations of UFVS-ALM and Scope for Improvement

The limitations and issues from a theoretical and numerical standpoint concerning UFVS-ALM are briefly presented below. The suggestions to improve the method eliminating some of the limitations mentioned in this section are postponed to the next section.

6.2.1 Chordwise loading variation

The basic underlying assumption in the ALM is that a rotor blade is modeled as an infinitely thin line adding momentum to the fluid equivalent to that of the rotor blade located along the aerodynamic center of the blade. This implies that chordwise variations in the blade loads are not modeled and not captured in the calculated flow field. This assumption is acceptable from an acoustics standpoint since the acoustic predictions are performed using chordwise compact loading but is definitely a limitation from the flow field point of view.

The model can be improved by using a better approximation for the chordwise variation instead of the Gaussian kernel. In reference [4] the authors used a distribution, show as red solid line in figure 6.1, to spread the source term (pressure) along the chordwise direction instead of a Gaussian function, shown as blue solid line in figure 6.1. This type of function approximates the rotor blade momentum distribution better as it is more realistic. An additional layer of sophistication can be added to the chordwise distribution by assuming a locally 2D airfoil section

of the blade and calculate the C_p distribution using a panel method. The input parameters for the panel method namely, velocity and angle of attack can be obtained from the predicted CFD flow field. Standard panel codes like XFOIL[56] can be readily coupled with the source calculation routine to obtain the chordwise C_p variation and the same can be used as the source distribution function.

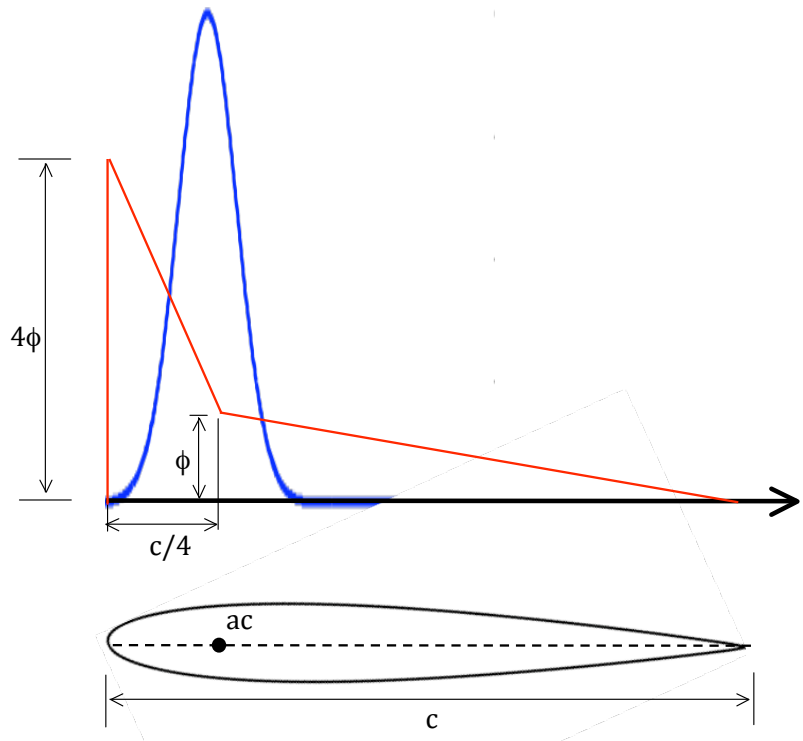

Figure 6.1: Area normalized chordwise source term distribution (a) red line is the source distribution in reference [4] and (b) blue line is the Gaussian source distribution.

6.2.2 Volume integration of rotor sources

The blade loads obtained using the UFVS-ALM suffer from high and low frequency errors generated from the volume integration of the source terms. Grid resolution less than 2 deg along the azimuth were required in the stand alone case to significantly reduce the error in the loads, thus making the calculations expensive. Using a low pass filter one can remove the high frequency noise but the low frequency noise cannot be eliminated and is a limitation for acoustic prediction using coarse

grids. A higher order quadrature for the integration of the volumetric sources is a possible solution to alleviate this problem. The computational cost incurred in the higher order integration can be considerably reduced in the present case by employing the integration only in cells where the actuator sources are spread and in the rest of the domain the source value is zero.

6.2.3 Tip correction

The key issue with the present method is the development of a tip correction function to correct the loading at the blade tip. The tip correction proposed in the present work based on the analytical tip correction of Prandtl resulted in numerical instability whereas an ad-hoc correction based on a tip correction length parameter was found to work satisfactorily. The primary reason is that the tip correction of Prandtl for a two bladed rotor predicts the fall in load to occur at about $0.95\mathcal{R}$ but there are hardly any cells in the spanwise direction to actually capture this sudden fall in source term. This fall can be controlled in the ad hoc correction using the tip correction length set to any arbitrary value ($0.8\mathcal{R}$ in the isolated rotor case) thus alleviating this problem. This is a serious limitation since the loads are largely under-predicted due to the loss in lift in the spanwise location from $0.8 - 0.95\mathcal{R}$.

A possible solution to this limitation is by using a stretching function to cluster points near the blade tip to capture the large variation in loading and prevent numerical instability. The use of higher order quadrature can be of additional help because the gradual change in source value over the volume can be captured, thus improving numerical stability.

6.2.4 Overset grid method

Although the oversetting of the UFVS-ALM with IBSEN has been successful there are issues with numerical oscillations in the load. The problem has to be understood first by identifying the source of the error before coming up with a strategy to eliminate or reduce these errors. At this point the error is suspected to be generated by reflections at the overset boundary because the interpolation used at these boundaries generates error that could affect the solution but the problem requires further investigation.

6.3 Future Extensions

The following are some of the recommendation proposed as future extension to the UFVS-ALM.

6.3.1 Low Mach number preconditioning

The ALM cannot predict shocks because there are no real blades in the domain and only source terms that mimic the blade. In addition, the acoustic prediction is indirectly coupled to the flow field as the compact chordwise loading approximation is actually coupled directly to the BET model. Therefore it is justified to use a low Mach number pre-conditioner[57] to scale the eigenvalue of the equation and speed up the calculations. There are two significant advantages, (i) the time step size can be almost doubled with only (ii) minimal change to to the code and without significant increase of operation count per time step. The eigenvalues for a preconditioned (λ_{pre}) and non-preconditioned (λ) Euler's equation are shown in equation (6.1) and (6.2) respectively.

$$\lambda_{pre} = (U, U, g - b, g + b) \tag{6.1}$$

$$\lambda = (U, U, U - c, U + c) \tag{6.2}$$

where, $g = \frac{1}{2\gamma}U(\gamma + \epsilon)$, $b = \frac{\hat{c}}{2}$ and the pseudo-acoustic speed $\hat{c}$ is give by the expression $\frac{\sqrt{(\epsilon-\gamma)^2+4\epsilon RT\gamma^2}}{\gamma}$. The parameter ϵ is given a value of γM_∞^2 in low Mach number flows to scale the sound speed to the same order as the fluid velocity. Shown in table 6.1 is an estimate of time step Δt with and without preconditioning for an isolated rotor in hover with tip speed (V_{tip}) of 150 ms^{-1}, smallest characteristic length (Δx) (ratio of cell volume to cell area) of 0.01 m, speed of sound (c) is 330 ms^{-1}, velocity scale $U = V_{tip}$, Mach number M_∞ is assumed to be the tip Mach number, the temperature is assumed to be 300 K and a CFL number of 0.8. One can take almost twice the time step size for a preconditioned system compared to a non-preconditioned case, which can be a huge saving in computational time as the operation count per time step is not significantly increased.

Parameter	Preconditioned	Non-preconditioned
Maximum Eigenvalue λ_{max}	$g + b = 240\ ms^{-1}$	$U + c = 480\ ms^{-1}$
$\Delta t = CFL\frac{\Delta x}{\lambda_{max}}$	$3.22\ 10^{-5}\ s$	$1.67\ 10^{-5}\ s$

Table 6.1: Estimated time step with and without preconditioning

6.3.2 Arbitrary blade motion

Arbitrary blade motion in the ALM can be achieved by simply shifting and rotating the Gaussian kernel used in the regularization of the singular sources. A trim procedure should be added to the blade element code in the ALM if one needs to simulate forward flight cases with arbitrary blade motion.

Appendix A

Low Pass Filtering

The loads obtained using the actuator line method described in chapter 3 suffer from high frequency numerical error due to the error in volume integration of the source terms. So a low pass filter (LPF) is used to remove the high frequency numerical error in the unsteady loading data. A LPF technique is adopted from Visbal and Gaitonde [50] that filters the load in the time domain. If ϕ is one of the component of the loading vector at a particular spanwise blade location varying w.r.t time with total time samples N, then the filtered values $\hat{\phi}$ are obtained by solving the tridiagonal system

$$\alpha\hat{\phi}_{i-1} + \hat{\phi}_i + \alpha\hat{\phi}_{i+1} = \sum_{n=0}^{3} \frac{a_n}{2} \left(\phi_{i+n} + \phi_{i-n}\right) \tag{A.1}$$

which provides a sixth order filter on a seven point stencil. The coefficients are derived in terms of α with Taylor and Fourier series analysis (given below), and acceptable values for the adjustable parameter α satisfy the inequality $-0.5 < \alpha \leq 0.5$. For most cases, values of α between 0.3 and 0.5 are appropriate. Coefficients for points $n = 4, N-3$ are given in Table A.1. The values at the endpoints 1

a_0	a_1	a_2	a_3
$\frac{11}{16} + \frac{5\alpha}{8}$	$\frac{15}{32} + \frac{17\alpha}{16}$	$-\frac{3}{16} + \frac{3\alpha}{8}$	$\frac{1}{32} - \frac{\alpha}{16}$

Table A.1: Low pass filter coefficients for points 4 through N-3.

and N are not filtered. The boundary points 2, 3, N-1, and N-2 are given special treatment with one-sided formulas.

$$\begin{aligned} \alpha\hat{\phi}_{i-1} + \hat{\phi}_i + \alpha\hat{\phi}_{i+1} &= \sum_{n=1}^{7} a_{n,i}\phi_n, i \in 2, 3 \\ \alpha\hat{\phi}_{i-1} + \hat{\phi}_i + \alpha\hat{\phi}_{i+1} &= \sum_{n=0}^{6} a_{N-n,i}\phi_{N-n}, i \in N-2, N-1 \end{aligned} \tag{A.2}$$

The right boundary values for a are found by noting that $a_{N-n,i} = a_{n+1,N-i+1}$. The values of a for points 2, $N-1$, 3, and $N-2$ are given in Tables A.2 and A.3.

Passing the data multiple times through the filter routine results in a sharper

$a_{1,2}$	$a_{2,2}$	$a_{3,2}$	$a_{4,2}$	$a_{5,2}$	$a_{6,2}$	$a_{7,2}$
$\frac{1}{64} + \frac{31\alpha}{32}$	$\frac{29}{32} + \frac{3\alpha}{16}$	$\frac{15}{64} + \frac{17\alpha}{32}$	$-\frac{5}{16} + \frac{5\alpha}{8}$	$\frac{15}{64} - \frac{15\alpha}{32}$	$-\frac{3}{32} + \frac{3\alpha}{16}$	$\frac{1}{64} - \frac{\alpha}{32}$

Table A.2: Low pass filter coefficients for points 2 and N-1.

$a_{1,3}$	$a_{2,3}$	$a_{3,3}$	$a_{4,3}$	$a_{5,3}$	$a_{6,3}$	$a_{7,3}$
$-\frac{1}{64} + \frac{\alpha}{32}$	$\frac{3}{32} + \frac{13\alpha}{16}$	$\frac{49}{64} + \frac{15\alpha}{32}$	$\frac{5}{16} + \frac{3\alpha}{8}$	$-\frac{15}{64} + \frac{15\alpha}{32}$	$\frac{3}{32} - \frac{3\alpha}{16}$	$-\frac{1}{64} + \frac{\alpha}{32}$

Table A.3: Low pass filter coefficients for points 3 and N-2.

frequency cut-off and is recommended for data with high sampling rates. The filter is optimized to have a cut-off frequency of twice the sampling frequency and hence the sampling rate for the loads should be approximately less than twice the Nyquist frequency (f_{nyq}), which is calculated using the relation in equation (A.3).

$$f_{nyq} = \frac{\Omega}{2d\theta} \tag{A.3}$$

where, Ω is the rotor angular speed and $d\theta$ is the azimuthal spacing of the cylindrical grid.

Appendix B

Least Squares Interpolation

The overset boundary condition in the IBSEN with UFVS-ALM requires a suitable interpolation routine to transfer values form the cylindrical grid to the neighboring Cartesian grid. The least squares interpolation was adopted as the interpolation procedure because Sengupta et al.[55] have shown success in using the same for polar grids. Shown in figure B.1 are the two domains the cylindrical grid (cyl) and Cartesian grid (cart). The point p is the acceptor point requiring information for the background Cartesian grid nodes shown in circles. The first step to obtain the interpolation function is to form the residual or error function R_i using Taylor series (up to first order) as shown in equation (B.1).

$$R_i = -f_i + f_p + f_x|_p \Delta x_i + f_y|_p \Delta y_i + f_z|_p \Delta z_i + O(\Delta^2) \tag{B.1}$$

The functional F is constructing by summing the square of the error function over all neighboring points i, $F = \sum_i R_i^2$. The functional F is minimized w.r.t the function values at the point p, f_p, and its derivatives, $f_{x-z}|_p$ to obtain four linear equations in terms of the function f_p and the first derivatives $f_{x-z}|_p$. The interpolation operator $\mathbf{C}$ can then be written in matrix form as shown in equation(B.2).

$$\mathbf{f} = \mathbf{C}^{-1}\mathbf{b} \tag{B.2}$$

where, $\mathbf{f} = [f_p \quad f_x|_p \quad f_y|_p \quad f_z|_p]^T$ and $\mathbf{b} = \left[\sum_{i=1}^{N} \frac{f_i}{N} \quad \sum_{i=1}^{N} \frac{\Delta x_i f_i}{N} \quad \sum_{i=1}^{N} \frac{\Delta y_i f_i}{N} \quad \sum_{i=1}^{N} \frac{\Delta z_i f_i}{N}\right]^T$.

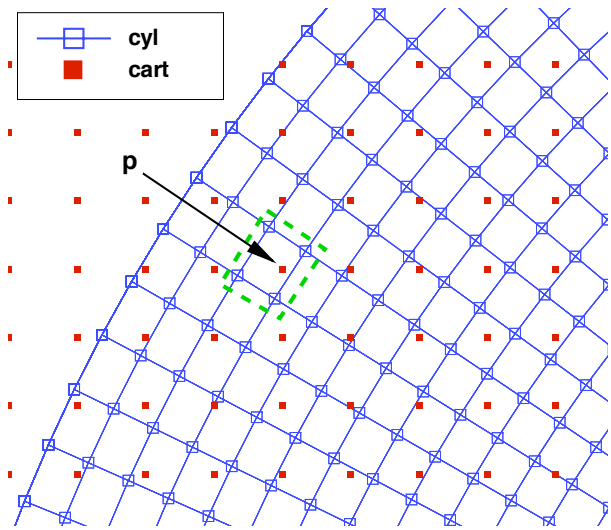

Figure B.1: The overlapping cylindrical (cyl) and Cartesian grid (cart) showing the acceptor point p and the neighboring cloud of points in green dotted line.

$$\mathbf{C} = \begin{pmatrix} 1 & \sum \frac{\Delta x_i}{N} & \sum \frac{\Delta y_i}{N} & \sum \frac{\Delta z_i}{N} \\ \sum \frac{\Delta x_i}{N} & \sum \frac{\Delta x_i^2}{N} & \sum \frac{\Delta x_i \Delta y_i}{N} & \sum \frac{\Delta x_i \Delta z_i}{N} \\ \sum \frac{\Delta y_i}{N} & \sum \frac{\Delta y_i \Delta x_i}{N} & \sum \frac{\Delta y_i^2}{N} & \sum \frac{\Delta y_i \Delta z_i}{N} \\ \sum \frac{\Delta z_i}{N} & \sum \frac{\Delta z_i \Delta x_i}{N} & \sum \frac{\Delta z_i \Delta y_i}{N} & \sum \frac{\Delta z_i^2}{N} \end{pmatrix} \tag{B.3}$$

The operator $\sum$ is the sum over all points $i = 1, N$. The least squares matrix $\mathbf{C}$ is real symmetric and only depends on the grid geometry. Therefore one gains significant computational time if the Cholesky decomposition of the least squares matrix is pre-computed and stored for each Cartesian overlap point. In Cholesky decomposition the least squares matrix is decomposed into a lower and upper triangular matrix $\mathbf{L}$ and $\mathbf{L}^T$ as shown in equation (B.4), where $\mathbf{L}^T$ is the transpose of $\mathbf{L}$. The Cholesky decomposition is computationally cheaper than LU decomposition as the former requires only half the number of operations as the latter to solve the linear system in equation (B.2).

$$\mathbf{C} = \mathbf{L}\mathbf{L}^T \tag{B.4}$$

The vector $\mathbf{f}$ can be computed by back-substution using the vector $\mathbf{b}$ (computed each time during interpolation) and the Cholesky matrix (pre-computed once) as shown in equation (B.5). The GNU Scientific Library[58] (GSL) Cholesky decomposition routines were used for decomposing the least squares matrix and performing back substitution.

$$\begin{aligned} \mathbf{L}\mathbf{f}^{(\mathbf{1})} &= \mathbf{b} \\ \mathbf{L}^T\mathbf{f} &= \mathbf{f}^{(\mathbf{1})} \end{aligned} \tag{B.5}$$

Bibliography

[1] D. D. Boyd. *Rotor/Fuselage Unsteady Interactional Aerodynamics: A New Computational Models*. PhD thesis, Virginia Polytechnic Institute and State University, 1999.

[2] OB́rien D. M Jr and Smith M. J. Analysis of Rotor-Fuselage Interactions Using Various Rotor Models. In *AIAA 43nd Aerospace Sciences Meeting*, number AIAA 2005-0468, 2005.

[3] Auld D. J. and Srinivas K. Aerodynamics for Students Webpage.

[4] Dobrev I., Massouh F., and Rapin M. Actuator Surface Hybrid Model. *Journal of Physics: Conference Series*, 75:1–7, 2007.

[5] Katz J. and Maskew B. Unsteady Low-Speed Aerodynamic Model for Complete Aircraft Configurations. *Journal of Aircraft*, 25, 1988.

[6] Summa J. M., Strash D. J., and Yoo S. A Novel Potential/Viscous Flow Coupling Technique for Computing Helicopter Flow Fields. (NASA-CR-193272), 1993.

[7] Ahmed S. R. Fuselage Aerodynamic Design Issues and Rotor/Fuselage Interactional Aerodynamics - part 2: Theoretical Methods. Technical Report AGARD-R-781, AGARD, 1993.

[8] Bramwell A. S. A Theory of the Aerodynamic Interference between a Helicopter Rotor Blade and a Fuselage and Wing in Hovering and Forward Flight. *Journal of Sound and Vibration*, 3, 1966.

[9] Peters D. A., Boyd D. D., and He C. J. Finite-State Induced-Flow Model for Rotors in Hover and Forward Flight. In *AHS conference*, 1987.

[10] Strawn R C and Biswas R. Numerical simulations of helicopter aerodynamics and acoustics. *Journal of computational and applied mathematics*, pages 471–483, 1996.

[11] Chen C. L., Mccroskey W. J., and Obayashi S. Numerical Solutions of Forward-Flight Rotor Flow using an Upwind Method. *Journal of Aircraft*, 28:374–380, 1991.

[12] Steijl R., Barakos G., and Badcock K. A Framework for CFD Analysis of Helicopter Rotors in Hover and Forward Flight. *International Journal for Numerical Methods in Fluids*, 51(8):819–847, 2006.

[13] Le Chuiton F. Actuator Disc Modeling for Helicopter Rotors. *Aerospace Science and Technology*, 8:285–297, 2004.

[14] Rajagopalan R. G. A Procedure for Rotor Performance Flow Field and Interference a Perspective. 2000. AIAA-2000-0116.

[15] Rajagopalan R. G. and Mathur S. R. Three Dimensional Analysis of a Rotor in Forward Flight. Number AIAA-1989-2045, 1989.

[16] Patankar S. V. and Spalding D. B. A Calculation Procedure for Heat, Mass and Momentum Transfer in Three-dimensional Parabolic Flows. *International Journal for Heat and Mass Transfer*, 15, 1972.

[17] Chaffin M.S. and Berry J.D. Navier-Stokes Simulation of a Rotor using a Distributed Pressure Disk Methods. In *Proceedings of the American Helicopter Society, 51st Annual Forum, Fort Worth, TX*, 1995.

[18] Mikkelsen R. *Actuator Disc Methods Applied to Wind Turbines*. PhD thesis, Technical University of Denmark, 2003.

[19] Shen W. Z., Mikkelsen R., Sorensen J. N., and Bak C. Tip Loss Corrections for Wind Turbine Computations. *Wind Energy*, 8(4):457–475, 2005.

[20] Ffowcs Williams J. E. and Hawkings D. L. Sound Generation by Turbulence and Surfaces in Arbitrary Motion. *Philosophical Transactions of the Royal Society of London. Series A, Mathematical and Physical Sciences*, 264(1151):321–342, 1969.

[21] Brentner K. S. and Farassat F. Helicopter Noise Prediction: The Current Status and Future Direction. *Journal of Sound and Vibration*, 170(1):79–96, 1994.

[22] Farassat F. Linear Acoustic Formulas for Calculation of Rotating Blade Noise. *AIAA Journal*, 19(9), 1981.

[23] Farassat F. Introduction to Generalized Functions with Applications in Aerodynamics and Aeroacoustic. (NASA-TP-3428), 1994.

[24] Farassat F. Derivation of Formulation 1 and 1A of Farassat. Technical Report NASA-TM-2007-214853, NASA, 2007.

[25] Brentner K. S. and Farassat F. Modeling Aerodynamically Generated Sound of Helicopter Rotors. *Progress in Aerospace Sciences*, 39, 2003.

[26] Morgans W. R. The Kirchhoff Formula Extended to a Moving Surface. *Philosophical Magazine*, 9:141–161, 1930.

[27] Kromov V. A. Generalisation of Kirchoff's Theorem for the Case of a Surface Moving in an Arbitrary way. *Soviet Physics - Acoustics*, 9:68–71, 1963.

[28] Farassat F. and Myers M. K. Extension of Kirchoff's Radiation Formula to Radiation from Moving Surfaces. *Journal of sound and vibration*, 123(3):451–460, 1988.

[29] Brentner K S and Farassat F. An Analytical Comparison of the Acoustic Analogy and Kirchhoff Formulation for moving surfaces. *AIAA Journal*, 36(8), 1997.

[30] George A. R. and A. S. Lyrintzis. Mid-Field and Far-Field Calculations of Transonic Blade-Vortex Interactions. In *AIAA10th Aeroacoustics Conference, Seattle, WA*, number AIAApaper 86-1854, July 9-11 1986.

[31] Berezin C., Visintainer J. Pollack M., Lyrintzis A., and Koutsavdis E. Development and practical application of the rotating kirchhoff method for the prediction of HSI and BVI noise. In *Proceedings of the AHS Technical Specialists Meeting for Rotorcraft Acoustics and Aerodynamics, Williamsburg, VA*, Oct. 1997.

[32] A. Uzun, Blaisdell G. A., and Lyrintzis A. S. 3-d Large Eddy Simulation for Jet Aeroacoustics. In *9th AIAA/CEAS Aeroacoustics Conference, Hilton Head, SC*, number AIAApaper 2003-3322, May 2003.

[33] Bres G. A., Brentner K.S., Perez G., and Jones H. E. Maneuvering Rotorcraft Noise Prediction. *Journal of Sound and Vibration*, 275(3):719–738, 2004.

[34] K. S. Brentner, L. V. Lopes, H. N. Chen, and J. F. Horn. Near realÐtime simulation of rotorcraft acoustics and flight dynamics,. In *Proceedings of the American Helicopter Society 59th Annual Forum*, Phoenix, AZ, May 2003.

[35] Brentner K. S. An Efficient and Robust Method for Predicting Helicopter High-Speed Impulsive Noise. *Journal of Sound and Vibration*, 203(1):87–100, 1997.

[36] L. V. Lopes. A New Model and Prediction Tool for Landing Gear Acoustics. Master's thesis, The Pennsylvania State University, University Park, Pennsylvania, December 2005.

[37] K. S. Brentner and H. E. Jones. Noise prediction for maneuvering rotorcraft. In *6th AIAA/CEAS Aeroacoustics Conference*, number AIAA 2000-2031, Lahaina, Hawaii, June 2000.

[38] Brentner K. S., Burley C. L., and Marcolini M. A. Sensitivity of Acoustic Predictions to Variation of Input Parameters. *Journal of the American Helicopter Society*, 39(3):43–52, 1994.

[39] Batchelor G. K. *An Introduction to Fluid Dynamics*. Cambridge university press, 2000.

[40] Knight M. and Hefner R. A. Static Thrust of Lifting Airscrew. Technical Report NACA TN 626.

[41] Wald Q. R. The Aerodynamics of Propellers. *Progress in Aerospace Sciences*, 42:85–128, 2006.

[42] Glauert H. *The Elements of Aerofoil and Airscrew Theory*. Cambridge Science Classics. Cambridge University Press, 1983.

[43] Mohseni K. and Colonius T. Numerical Treatment of Polar Coordinate Singularities. *Journal of Computational Physics*, 157(2):787–795, 2000.

[44] Constantinescu G. S. and Lele S. K. A Highly Accurate Technique for the Treatment of Flow Equations at the Polar Axis in Cylindrical Coordinates using Series Expansions. *Journal of Computational Physics*, 183(1):165–186, 2002.

[45] Hixon R., Shih S. H, and Mankbadi R. R. Numerical Treatment of Cylindrical Coordinate Centerline Singularities. In *35th AIAA/ASME/SAE/ASEE Joint Propulsion Conference and Exhibit*, 1999.

[46] Ma L., Ingham D.B., and Wen X. A Finite Volume Method for Fluid Flow in Polar Cylindrical Grids. *Int. J. Numer. Meth. Fluids*, 28:663–677, 1998.

[47] P. L. Roe. Approximate Riemann Solvers, Parameter Vectors, and Difference Schemes. *J. Comput. Phys.*, 135:250–258, 1997.

[48] Jameson A., Turkel E., and Schmit W. Numerical Solution of the Euler Equation by Finite Volume Methods using Runge-Kutta Time-Stepping Schemes. In *14th AIAA Fluid and Plasma Dynamics Conference*, 1981.

[49] Rabott J. P. Static Thrust Measurements of the Aerodynamic Loading on a Helicopter rotor blade. 1956. NACA-TN3688.

[50] Visbal M. R. and Gaitonde D. V. On the Use of Higher-Order Finite-Difference Schemes on Curvilinear and Deforming Meshes. *Journal of Computational Physics*, 181:155Ð185, 2002.

[51] Alpert P. Implicit Filtering in Conjunction with Explicit Filtering. *Journal of Computational Physics*, 44(1):212–219, 1981.

[52] Y. Bhumkara T.K. Sengupta and V. Lakshmanana. Design and Analysis of a New Filter for LES and DES. *Computers & Structures*, 87(11-12):735–750, 2009.

[53] Aouida S. Validation Report for elsA v3.3. Technical Report ELSA/PTST-98088, ONERA, November 2009.

[54] Hennes C. C. Interactional aerodynamics for noise prediction of heavy lift rotorcraft configurations. 2009. Penn State, PhD Thesis.

[55] T. K. Sengupta and Dipankar A. Suppression of Vortex Shedding Behind a Circular Cylinder by Another Control Cylinder at Low Reynolds Numbers. *Journal of Fluid Mechanics*, 573:171–190, 2007.

[56] M. Drela. XFOIL: An Analysis and Design System for Low Reynolds Number Airfoils. In *Conference on Low Reynolds Number Airfoil Aerodynamics*. University of Notre Dame, June 1989.

[57] Choi Y. H. and Merkle C. L. The Application of Preconditioning in Viscous Flows. *Journal of Computational Physics*, 105:207–223, 1993.

[58] M. Galassi et al. *GNU Scientific Library Reference Manual (3rd Ed.)*. 2009.